

University of Alberta

**The Studies of Thiosulfate and Lead-induced Stress Corrosion
Cracking of Alloy 800**

by

Liang Yu

A thesis submitted to the Faculty of Graduate Studies and Research
in partial fulfillment of the requirements for the degree of

**Master of Science
in
Materials Engineering**

Department of Chemical and Materials Engineering

©Liang Yu
Spring 2011
Edmonton, Alberta

Permission is hereby granted to the University of Alberta Libraries to reproduce single copies of this thesis and to lend or sell such copies for private, scholarly or scientific research purposes only. Where the thesis is converted to, or otherwise made available in digital form, the University of Alberta will advise potential users of the thesis of these terms.

The author reserves all other publication and other rights in association with the copyright in the thesis and, except as herein before provided, neither the thesis nor any substantial portion thereof may be printed or otherwise reproduced in any material form whatsoever without the author's prior written permission.

Examining Committee

Dr. Jingli Luo, Chemical and Materials Engineering, University of Alberta

Dr. Thomas H. Etsell, Chemical and Materials Engineering, University of Alberta

Dr. Xiaodong Wang, Mechanical Engineering, University of Alberta

Abstract

Scratch test and scanning electrochemical microscopy (SECM) were applied to study the effects of thiosulfate on stress corrosion cracking (SCC) of Alloy 800 in simulated crevice solutions. The results showed that thiosulfate cathodically shifted the pitting potential of Alloy 800 significantly and the pitting morphology on the electrode surface was also different from that formed in the absence of thiosulfate. The synergistic effect between thiosulfate and stress was also observed, which was mainly promoting enhanced anodic dissolution at active sites.

In the lead-induced stress corrosion crackings (PbSCC) work, the crack propagation rate (CPR) of Alloy 800 double cantilever specimen were estimated in neutral crevice chemistries solutions at 300 degree Celsius. The PbSCC of alloy 800 at high temperature were investigated by comparing the CPR rate of Pb-contaminated and Pb-free conditions. A repetitive behavior of crack advance was observed from the measurement. This observation is consistent with the film rupture model.

Acknowledgements

First of all, I would like to sincerely thank my supervisor Prof. Jingli Luo for her patient input, tremendous assistance, and encouragement throughout my studies in University of Alberta. She is not only a mentor in my research, but also in my life.

I am grateful to my colleagues Dr. Renkang Zhu, Dr. Lianpeng Tian, Luning Wang, and everyone in our group for helpful discussions, valuable input, and such a good working atmosphere that we are embracing. I would also like to thank the professors, students, and staff in the Department of Chemical and Materials Engineering for their constant assistance in the past several years. This work would not have been possible without the financial support of the Natural Sciences and Engineering Research Council and Atomic Energy of Canada Limited.

I also wish to express my deepest appreciation to my mother, Heping Xiao, my father, Zengxiang Yu, my sister, Li Yu, and most importantly my fiancée, Xin Zhang, for their constant encouragement, support and love.

Table of Contents

Title	
Examining Committee	
Abstract	
Acknowledgement	
Table of Contents	
List of Figures	
List of Tables	
List of Abbreviations and Symbols	
CHAPTER 1 INTRODUCTION.....	1
REFERENCES.....	3
CHAPTER 2 LITERATURE REVIEW.....	5
2.1 INTRODUCTION.....	5
2.2 INTRODUCTION OF ALLOY 800.....	5
2.3 INTRODUCTION OF SCC.....	6
2.3.1 Basic Concepts of SCC.....	6
2.3.2 Mechanisms of SCC.....	9
2.4 INTRODUCTION OF REDUCED SULFATE STRESS CORROSION CRACKING (S ^{y-} SCC).....	10
2.4.1 The Origin of Low Valence Sulfate Species.....	11
2.4.2 The Effect of Dissolved Reduced Sulfate Species on SCC.....	13

2.5 LEAD-INDUCED STRESS CORROSION CRACKING (PbSCC).....	16
2.6 FILM RUPTURE THEORY.....	19
2.7 ELECTROCHEMISTRY OF LOCALIZED CORROSION.....	21
2.8 POTENTIAL DROP TECHNIQUE.....	23
2.8.1 Introduction.....	23
2.8.2 Theoretical Aspects of Direct Current Potential Drop.....	26
2.8.3 DCPD Calibration.....	27
2.8.4 Effect of Temperature on DCPD.....	31
2.8.5 Application of DCPD in detecting SCC propagation of nuclear materials.....	32
2.9 SCANNING ELECTROCHEMICAL MICROSCOPE (SECM).....	33
2.9.1 Introduction.....	33
2.9.2 Principles of SECM.....	36
2.9.2.1 <i>Ultramicroelectrodes</i>	36
2.9.2.2 <i>Feedback Mode</i>	38
2.9.2.3 <i>SECM Surface Imaging</i>	40
2.9.3 Applications of SECM.....	42
2.10 SUMMARY.....	43
REFERENCES.....	45
CHAPTER 3 EXPERIMENTAL APPARATUS AND PROCEDURES...	56
3.1 MATERIALS AND SOLUTIONS.....	56
3.1.1 Test Materials - Alloy 800 (UNS N08800).....	56

3.1.2 Solutions for S^{y-} SCC Studies.....	58
3.1.3 Solutions for PbSCC Studies.....	59
3.2 TEST SPECIMEN PREPARATION.....	60
3.2.1 C-ring Specimen for S^{y-} SCC Studies	60
3.2.2 Double Cantilever Beam (DCB) Specimen with Constant Opening Displacement.....	63
3.3 EXPERIMENTAL APPARATUS, SETUPS AND PROCEDURES.....	65
3.3.1 Scratch Test.....	65
3.3.2 Scanning Electrochemical Microscopy Test.....	67
3.3.3 Potential Drop Technique.....	69
3.3.4 The Calculation of the Stress Intensity Factor K for DCB Specimen...70	
REFERENCES.....	73

**CHAPTER 4 THE STUDY OF THIOSULFATE STRESS CORROSION
CRACKING OF ALLOY 800 USING SCRATCH TESTING AND
SCANNING ELECTROCHEMICAL MICROSCOPY.....75**

4.1 RESULTS AND DISCUSSION.....	75
4.1.1 Investigation of Microstructures of Alloy 800 Specimens.....	75
4.1.2 Effects of Stress and Thiosulfate on the Pitting Potential of Alloy 800 Specimen.....	78
4.1.3 Localized Corrosion Effects of Thiosulfate and Stress.....	93
4.1.4 Semi-Quantitative Results of Localized Reactivity.....	99
4.2 CONCLUSIONS.....	103

REFERENCES.....104

**CHAPTER 5 THE STUDIES OF ALLOY 800 AT 300°C BY USING
DIRECT CURRENT POTENTIAL DROP TECHNIQUE.....113**

5.1 RESULTS AND DISCUSSIONS.....113

5.1.1 Calibration of Potential Drop System.....113

*5.1.1.1 Calibration Curve of Alloy 800 DCB Specimen at Room
Temperature.....113*

*5.1.1.2 Temperature Dependence of the Resistivity of Alloy 800 DCB
Specimen.....116*

5.1.1.3 Calibration Curve of Alloy 800 DCB Specimen at 300°C.....119

5.1.2 The effect of Pb on the SCC of Alloy 800 DCB Specimen By Real
Time Crack Propagation Monitoring.....121

*5.1.2.1 The Comparison of Voltage Changes in Pb-contaminated and
Pb-free Conditions.....121*

*5.1.2.2 The Calculation of the Predicated Crack Length Increase by
Calibration Curves.....129*

*5.1.2.3 The Examination of the Real Crack Length Increases by SEM
methods.....133*

5.1.3 Periodic Crack Propagation Behaviours.....141

5.1.4 The Calculation of the Stress Intensity Factor K for Alloy 800 DCB
Specimen in Both Pb-contaminated and Pb-free Conditions at 300
°C.....144

5.2 CONCLUSIONS.....149

REFERENCES.....150

CHAPTER 6 GENERAL CONCLUSIONS AND FUTURE WORK.....154

6.1 GENERAL CONCLUSIONS.....154

6.2 FUTURE WORK.....155

List of Figures

Figure 1.1 The electricity sources distribution in Ontario province.....	1
Figure 2.1 Three conditions necessary for SCC.....	9
Figure 2.2 Potential vs. pH diagram for the stability of sulphur species in aqueous environment at 300 °C	12
Figure 2.3 Potential vs. pH diagram for the stability of sulphur species in aqueous environment at 25 °C.....	13
Figure 2.4 Schematic of Q_f vs. time relationship for a strained crack tip and unstrained crack sides.....	20
Figure 2.5 Schematic polarization curve (plot of applied potential vs. log current density) showing the active region, passive region, open circuit potential (E_{oc}), the primary passivation potential (E_{pp}), the pitting potential (E_p), the transpassive potential (E_t), and the critical current density (I_{crit}).....	23
Figure 2.6 Schematic Illustration of a SECM setup in our work.....	36
Figure 2.7 Schematic diagram of a cell for ultramicroelectrode voltammetry.....	37
Figure 2.8 Typical voltammogram for an ultramicroelectrode.....	38
Figure 2.9 Typical probe approach curves, diffusion-controlled steady-state tip current as a function of tip-substrate separation distance. (a) Substrate is a conductor; (b) Substrate is an insulator.....	41

Figure 3.1 Schematic representation of C-ring specimen (a) side view (b) outlook	62
Figure 3.2 The Schematic Representation of the Potential Drop Measurement on an Alloy 800 Double Cantilever Specimen with a wedge.....	63
Figure 3.3 The design and dimension of DCB specimen.....	64
Figure 3.4 The schematic representation of the double-tapered wedge	65
Figure 3.5 The schematic representation of the scratch test system.....	67
Figure 3.6 The illustration of voltage measurement and dc current going through the alloy 800 specimen.....	69
Figure 3.7 The schematic representation of the DCB specimen with a load P.....	71
Figure 4.1 SEM image (a) and EDX results (b) of Alloy 800.....	76
Figure 4.2 Microstructures of Alloy 800 without (a and b) and without stress (c and d).....	77
Figure 4.3 Polarization curves of Alloy 800 in neutral crevice chemistries. (a): unstressed specimen in sulphate solution (NC1), (b): unstressed specimen in thiosulfate solution (NC2), and stressed specimen in thiosulfate solution (NC2). i is the current density (A/cm^2).....	79
Figure 4.4 Comparison of scratch testing results at different potentials on unstressed Alloy 800 C ring specimens in simulated NC1. (a) Current plots of potentiostat processes; (b) Peak current at different potentials.....	82

Figure 4.5 Comparison of scratch testing results at different potentials on stressed Alloy 800 C-ring specimens in simulated NC1. (a) Current plots of potentiostat processes; (b) Peak current at different potentials.....83

Figure 4.6 Comparison of scratch testing results at different potentials on unstressed Alloy 800 C-ring specimens in simulated NC2. (a) Current plots of potentiostat processes; (b) Peak current at different potentials.....86

Figure 4.7 Comparison of scratch testing results at different potentials on stressed Alloy 800 C-ring specimens in simulated NC2. (a) Current plots of potentiostat processes; (b) Peak current at different potentials.....86

Figure 4.8 Comparison of peak currents of scratch tests at different potentials in both NC1 and NC2 with and unstressed Alloy 800 C-ring specimens. (a): the peak current in four conditions; and (b): the synergistic effect of thiosulfate and stress on the peak current.....87

Figure 4.9 Comparison of the current at 0.0 V after a scratch under four conditions: the specimens (a) without stress and (b) with stress in NC1, the specimens (c) without stress and (d) with stress in NC2; and d: the specimen with stress in NC2.....92

Figure 4.10 Comparison of SEM images of scratched surface morphologies under different conditions in NC2.

- (a): -0.1 V on unstressed specimens;
- (b): -0.1 V on stressed specimens;
- (c): 0 V on unstressed specimens; and
- (d): 0 V on stressed specimens.....93

Figure 4.11 SECM images of Alloy 800 specimens. (a): without stress in NC1 with ferrocenemethanol (Fc), (b): without stress in NC2 with Fc, and (c): with stress in NC2 with Fc. Potential on tip: 0.50 V; and potential on specimen: 0.10 V. Tip had 5 μm in radius with RG of 5.95

Figure 4.12 PACs at different reactive regions on Alloy 800 specimens. (a): non reactive region; and (b): reactive region. Potential on tip: 0.50 V; and potential on specimen: 0.10 V. Tip had 5 μm in radius with RG of 5. Quiet time was 30 s; approach speed was 1 μm/s.....98

Figure 4.13 PACs toward different active regions on the Alloy 800 specimen with stress in NC2 at 0.1 V. (PT1 (circle): non-active region, PT2 (star): between non-active and active region and PT3 (diamond): active region). The solid lines close to the symbols are the simulation curves in the corresponding conditions, and the bottom solid line is the simulation data for an insulator surface and the dotted line is the simulation data for a conductive surface. Other parameters 4.13..101

Figure 4.14 Simulated data of apparent rate constants (k) obtained on different reactive regions of Alloy 800. (a): non-reactive region; (b): the region with current between the highest and lowest ones; and

(c): reactive region. Potential on tip: 0.65 V.....103

Figure 5.1 The calibration curve of actual potential values vs. real crack length for alloy 800 at room temperature.....114

Figure 5.2 The normalized calibration curve of normalized potential values vs. normalized crack length for alloy 800 at room temperature.....116

Figure 5.3 The temperature dependence of the normalized resistance of alloy 800 DCB specimen from 292 to 573 K.....118

Figure 5.4 Normalized potential of alloy 800 DCB specimen as a function of time in Pb-contaminated neutral crevice chemistries conditions.....122

Figure 5.5 Comparison of Alloy 800 DCB specimens with applied stress in Pb-contaminated (top) and Pb-free (bottom) neutral crevice chemistries conditions.....124

Figure 5.6 Comparison of different spots in (1) fast fracturing region (2) crack growth region, and (3) fatigue pre-crack region. (a) SEM image comparison of different spots, (b) Comparison of lead composition at different spots by EDX.....128

Figure 5.7 The expanded SEM image of the crack arrest on the alloy 800 DCB specimen in the Pb-contaminated neutral crevice chemistries conditions.129

Figure 5.8 SEM image of the cross-sectional view of the alloy 800 DCB specimen after potential drop measurement in Pb-contaminated environment.....135

Figure 5.9 SEM images of the crack arrest in Pb-contaminated condition with the crack length measurements at different spots of the crack (a) Left (b) Right and (c) Middle.....	137
Figure 5.10 SEM image of the cross-sectional view of the alloy 800 DCB specimen after potential drop measurement in Pb-free environment.....	139
Figure 5.11 SEM images of the crack arrest in Pb-free with the crack length measurements in the middle of the crack.....	140
Figure 5.12 Comparison of (a) potential fluctuation in crack propagation process and (b) reference potential signal of the same specimen.....	143
Figure 5.13 The SEM image of the crack arrest in the Pb-contaminated neutral crevice chemistries conditions, showing the periodic crack advance behaviors.....	144
Figure 5.14 The schematic representation of the DCB specimen with a load P.	146

List of Tables

Table 3.1 Compositions of materials used in the experiments	57
Table 3.2 Summary of the base crevice chemistries.....	58
Table 3.3 Proposed test matrix for degradation of SG tubing materials in reduced sulphur environments.....	59
Table 3.4 Simulated CANDU SG Crevice Chemistries with and without Lead Oxide.....	60
Table 4.1 Corrosion potentials, passive current density and pitting potentials obtained on the polarization curves in Figure 4.3.....	78
Table 4.2 Summary of repassivation time (unit: ms) in scratch test.....	90
Table 5.1 The values and standard errors of the constants in temperature dependence curve (shown in Equation 5.5).....	119
Table 5.2 Linear fitting results with stand errors of crack propagation curves for alloy 800 DCB specimen with applied stress in Pb contaminated and Pb-free conditions at 300°C.....	125
Table 5.3 The calculation table of the average crack length changes Δa_1 , Δa_2 , and Δa_3	138

List of Abbreviations and Symbols

AC	acidic
ACPD	alternating current potential drop
ACR	Advance CANDU Reactor
AcSCC	acidic stress corrosion cracking
AECL	Atomic Energy of Canada Limited
AFM	Atomic force microscopy
AkSCC	alkaline stress corrosion cracking
AVT	all volatile treatment
BC	basic
CANDU	Canada Deuterium Uranium
CE	counter electrode
CERT	constant extension rate test
COD	the crack opening displacement
CPR	crack propagation rate
CT	compact tension
DCB	double cantilever beam
DCPD	direct current potential drop
EAC	environmentally assisted cracking
EDX	energy-dispersive X-ray spectroscopy
E_{oc}	open circuit potential

E_p	pitting potential
E_{pp}	primary passivation potential
E_t	transpassive potential
Fc^+	ferroceniummethanol
FIC	film-induced cleavage
HE	hydrogen brittlement
HER	hydrogen evolution reaction
HPSCC	high-potential stress corrosion cracking
I_{crit}	critical potential
I_{pass}	the passive current density
IGA	intergranular attack
IGSCC	intergranular stress corrosion cracking
LTSCC	low-temperature stress corrosion cracking
NC	neutral
NOD	notch opening displacement
NSOM	near-field scanning optical microscopy
OCP	open circuit potential
OD	outside diameter
OgSCC	organic stress corrosion cracking
PAC	probe approaching curve
PbSCC	lead-induced stress corrosion cracking
PPS	pitting precursor sites
PTFE	polytetrafluoroethylene

PWR	pressurized water reactor
RE	reference electrode
SCC	stress corrosion cracking
SCE	saturated calomel electrode
SECM	scanning electrochemical microscopy
SG	steam generator
SG/TC	substrate generation/tip collection
SHE	standard hydrogen electrode
SS	stainless steel
SSRT	slow strain rate test
STM	scanning tunneling microscopy
S ^y -SCC	reduced sulphur species stress corrosion cracking
TD/SC	tip generation/substrate collection
UME	ultramicroelectrode
V _n	normalized potential
V _r	reference potential
V _Y	the crack opening displacement at loaded line
WE	working electrode

Chapter 1

Introduction

Nuclear power is a promising alternative in the future to solve the energy problem. A series of new nuclear power plants will be built in the next several decades. For example, China plans to extend the current pressurized water reactor (PWR) by 32 units by 2020, with a long term goal of putting about 200 reactors into action [1]. In Ontario, nuclear power has supplied more than 50% of the electricity consumption, as shown in Figure 1.1 [2]. To maintain the safe operation of nuclear reactors, lots of efforts have been made. However, degradation of the steam generator (SG) materials is still one of the major safety concerns.

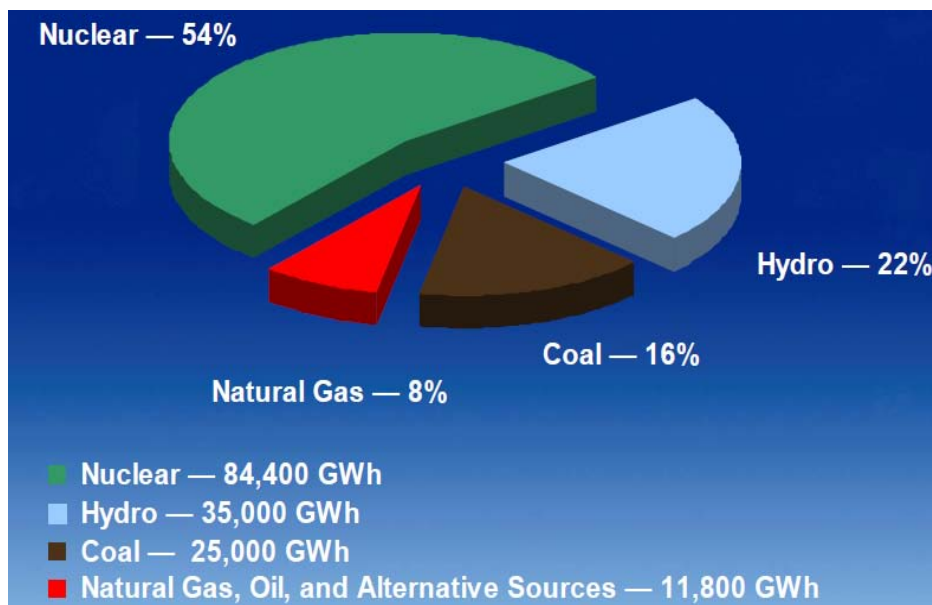


Figure 1.1 The electricity sources distribution in Ontario province.

Steam generator tubes, accounting for more than 50% of the pressure boundary surface of pressurized water reactors (PWRs), have experienced various forms of corrosive and mechanical degradation, and environmentally induced degradation through intergranular stress corrosion cracking (SCC) is the most serious degradation process at present. The SCC degradation, commonly occurring in crevice regions such as tube support plate, tube sheet locations or under sludge piles, contains different submodes, of which the lead induced SCC (PbSCC) and reduced sulphur species stress corrosion cracking (S^{y-} SCC) have drawn a great attention in the degradation of SG tube materials.

To obtain a better understanding of PbSCC, lots of efforts have been made to investigate the basic mechanisms, effect of temperature, environment, microstructure, passive film ductility and so on [3-6]. However, in the industrial application, the life prediction of the nuclear reactor becomes a very important topic. The investigation on crack propagation rates (CPRs) is essential for the prediction of service life. In this work, the crack propagation mechanism and CPRs of alloy 800 under 300°C in simulated neutral crevice solutions has been studied for the first time by the potential drop system.

In the CANDU* Steam Generator (SG) operations, the SCC caused by low valence sulphur species is also an important issue. The reduced sulphur species can deteriorate the Ni-based alloy and increase its SCC susceptibility. The mechanisms of S^{y-} SCC have been investigated for stainless steel and Alloy 600 [7-9]. However, the effect of applied stress on the S^{y-} SCC of Alloy 800 has never

* CANDU is a registered trademark of Atomic Energy of Canada Limited (AECL).

been studied before. The *in situ* localized electrochemical activity of passive film on the specimen surface has also been investigated for the first time by scanning electrochemical microscopy (SECM).

Chapter 2 will review the literature related to the PbSCC and S^y-SCC studies, and the experimental procedures will be described in Chapter 3. Chapter 4 and 5 will discuss the results for S^y-SCC and PbSCC, respectively, followed by the general conclusions and future work in Chapter 6.

References

1. F. P. Ford, "*Technical and Management Challenges Associated with Structural Materials Degradation in Nuclear Reactors in the Future*", proc. 13th Environmental Degradation of Materials in Nuclear Power Systems, Canadian Nuclear Society, 2007.
2. Source: *Independent Electricity System Operator (IESO)*, 2007.
3. T. Sakai, K. Aoki, T. Shigemitsu, Y. Kishi, *Corrosion* 48 (1992): p. 745.
4. T. Sakai and et al, Mechanism of Lead-Induced Stress Corrosion Cracking of Nickel-Based Alloys in High-Temperature Water, *Corrosion*, Vol. 54, No.7, 1998, p 515.
5. Y.C. Lu, Effect Of Lead Contamination On Steam Generator Tube Degradation, *Proceedings of 12th International Conference on Environmental Degradation of Materials in Nuclear Power Systems - Water Reactors* Edited by TMS (The Minerals, Metals & Materials Society), 2005.

6. B.T. Lu, J.L. Luo, Y.C. Lu, *Electrochimica Acta*, 53(12), 2008, p. 4122.
7. R.C. Newman, H.S. Isaacs and B. Alman, *Corrosion*, 38, (1982) p. 61.
8. P. Marcus, *J. Chem. Phys.*, 88, (1991), p. 1697.
9. S.J. Mulford and D. Tromans, *Corrosion*, 44, (1988) p. 891.

Chapter 2

Literature Review

2.1 Introduction

This chapter will give a brief introduction of Alloy 800 first, and then provide an overview of the general concept and mechanisms of SCC. After that, the reduced sulfate SCC (S^y -SCC) will be discussed, and lead-induced SCC (PbSCC) will also be presented in this chapter. These two types of SCC are the major focus of this work.

The research on the potential drop system will be reviewed to illustrate the advantage of this technique. The scanning electrochemical microscope (SECM) will also be introduced as an effective tool for the surface chemical activity analysis. In addition, the film rupture theory will be described as well to support the observation on the potential drop measurements of Alloy 800 under high pressure condition at 300°C.

2.2 Introduction of Alloy 800

Alloy 800 is a widely used material for construction or equipment that requires high strength and corrosion resistance under exposure to corrosive

environments and high temperatures. It is usually used for heat-treating equipment such as baskets, trays and fixtures. In nuclear power plants, it is used for SG tubing. In chemical and petrochemical processing the alloy is used for heat exchangers and other piping systems in nitric acid media especially where resistance to chloride SCC is required. In the production of paper pulp, digester liquid heaters are often made of alloy 800. The alloy is also used in domestic appliances for sheathing of electric heating elements. In addition, for high temperature applications requiring optimum creep and rupture properties, Incoloy® alloys 800H and 800HT® are often used.

2.3 Introduction of SCC

2.3.1 Basic Concepts of SCC

SCC is the unexpected sudden failure of normally ductile metals or tough thermoplastics subjected to a constant tensile stress in a corrosive environment, especially at elevated temperature (in the case of metals). SCC is a type of environmentally assisted cracking (EAC), which is a term that describes the formation of cracks caused by various factors combined with the surrounding environment [1]. All those factors together will reduce the pressure carrying capacity of the materials. For example, the minerals, gases, and ions in the water will create corrosion that attacks the steel, when water as an electrolyte comes into contact with the steel.

Typical SCC occurring in SGs includes: alkaline stress corrosion cracking (AkSCC), low potential stress corrosion cracking (LPSCC), acidic stress corrosion cracking (AcSCC), high-potential stress corrosion cracking (HPSCC), lead stress corrosion cracking (PbSCC), organic stress corrosion cracking (OgSCC), doped steam stress corrosion cracking (DSSCC), low-temperature stress corrosion cracking (LTSCC), and reduced sulphur stress corrosion cracking (S^y -SCC). In this work, we will mainly talk about the effects of S^y -SCC and PbSCC on the alloy 800 SG materials. EAC will be introduced briefly before we talk about SCC.

EAC includes two different mechanisms: SCC and corrosion fatigue. SCC involves corrosive mechanisms and depends on both an aggressive environment and tensile stress. The tensile stress opens up cracks in the material and can be either directly applied or residual in form. “Corrosion Fatigue” occurs when chemically reactive agents penetrate fatigue cracks. The chemical condition within the crack can be more aggressive than on the free surface. Even if the metal surface at the crack tip could be passivated (forms an inert barrier), the next fatigue loading can crack the brittle deposit and reactivate the whole process. Thus, corrosion fatigue is the joint action of a cyclic stress and a corrosive environment that decrease the number of cycles to failure. Therefore, SCC occurs under sustained tensile loads, while corrosion fatigue occurs under cyclic loading [1].

For example, a pipe in seawater with slowly applied cycles of loading will not crack due to stress corrosion cracking but it will develop corrosion fatigue

cracks if enough cycles of loading are applied. Another example is that a pipe in a carbonic acid environment (near-neutral pH) tends to crack due to SCC when subjected to slowly applied cycles of loading. e.g. less than one cycle per day. If the loading frequency is increased to hundreds of load cycles per day, corrosion fatigue cracks can develop. If the loading frequency is increased further, fatigue cracks can develop since the time in contact with the environment is too short for the environment to have an effect [2]. After careful comparison, we can see that the difference lies in the amount of time the environment is in contact with the steel during the tensile loading portion of the cycle.

The simultaneous effects of the following three factors are required to be present together for SCC to occur. The description is illustrated in detail in Figure 2.1 [1].

1. A potent environment at the material surface
2. A susceptible material
3. Sufficient tensile stress to induce SCC

EAC will be introduced briefly before we talk about SCC.

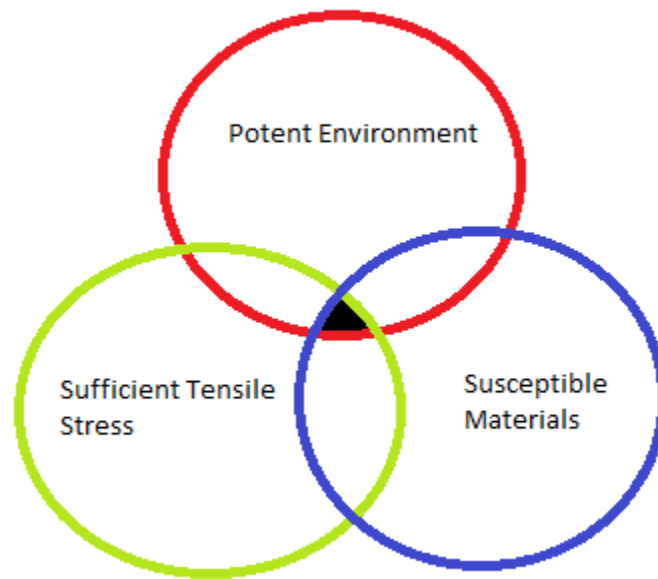


Figure 2.1 Three conditions necessary for SCC

2.3.2 Mechanisms of SCC

Three basic mechanisms of stress corrosion cracking have been identified as described below [28].

1. Anodic dissolution mechanism (Active path dissolution)

This process involves corrosion behavior along a path that has high corrosion susceptibility. The anodic current rises when the metals are stressed or strained, which will further accelerates the anodic dissolution of the materials [85-86].

The slip-dissolution mechanism is another type of dissolution mechanism, which is introduced in the film rupture theory [23]. When this process involves

oxidation and reduction reactions, it is usually called slip-oxidation mechanism. We will discuss more in detail in section 2.6 “Film Rupture Theory”.

2. Hydrogen-related mechanisms (Hydrogen embrittlement)

Hydrogen tends to be attracted to regions of high triaxial tensile stress where the metal structure is dilated. The dissolved hydrogen then assists in the fracture of the metal, possibly by making cleavage easier or possibly by assisting in the development of intense local plastic deformation. These effects lead to embrittlement of the metal; cracking is usually transgranular. Crack growth rates are typically relatively rapid, up to 1 mm/s in the most extreme cases [87-88].

3. Film-Induced cleavage (FIC) mechanism

If a normally ductile material is coated with a brittle film, then a crack initiated in that film can propagate into the ductile material for a small distance (around 1 μ m) before being arrested by ductile blunting. If the brittle film has been formed by a corrosion process then it can reform on the crack tip and the process can be repeated. The brittle films that are best established as causing film-induced cleavage are de-alloyed layers (e.g. in brass). The film-induced cleavage process would normally be expected to give a transgranular fracture [28].

2.4 Introduction of Reduced Sulfate Stress Corrosion Cracking (S^{y-}SCC)

Low valence sulphur SCC (S^{y-}SCC) is an important issue in the CANDU Steam Generator (SG) operations. Reduced sulfate species can increase the

susceptibility of Ni based alloy to SCC dramatically.

2.4.1 The origin of low valence sulfate species

Sulfate impurities and released resins accumulate in heat-transfer crevices and they will become low valence sulfate species in the reduced environment very easily. All volatile treatment (AVT) has been used for CANDU-6 SGs and is recommended for Advanced CANDU Reactor 1000 (ACR-1000) [29]. To maintain an alkaline environment at the operating temperature, the volatile bases, including either ammonia or an organic amine, were used. A volatile reducing agent, like hydrazine, is also used to scavenge oxygen from the feed water and to maintain reducing conditions in the SGs. The current full power hydrazine concentration specified for SG feedwater at CANDU stations in Ontario is typically 100 to 120 $\mu\text{g}/\text{kg}$. According to the recommended Atomic Energy of Canada Limited (AECL) specification, hydrazine in feedwater and SG blowdown, is usually set at five times of the final feedwater dissolved oxygen concentration or an amount sufficient to maintain a residual concentration in the SG between 25 to 50 $\mu\text{g}/\text{kg}$ [30].

However, low valence sulphur species can be produced by N_2H_4 in the reducing environment. The stable species of sulphur at 300°C are shown in Figure 2.2. The transition from the +6 state to the -2 state occurs slightly above the half-cell equilibrium potential of $\text{H}_2\text{O}/\text{H}_2$. However, in the acidic conditions, H_2S is the most stable species and is volatile. The sulphide is stable and generally insoluble above pH 7. During the reduction of SO_4^{2-} and HSO_4^- by N_2H_4 , intermediate

species of SO_3^{2-} , $\text{S}_3\text{O}_4^{2-}$, and $\text{S}_2\text{O}_3^{2-}$ may be present.

In addition, the lower potential conditions are present in SG secondary sites due to the presence of hydrazine in the SG water. It makes reduced forms of sulphur the thermodynamically stable species [31]. Although the rate of sulphate reduction is slow, it can be accelerated by the presence of magnetite that can serve as a catalyst for this reduction reaction.

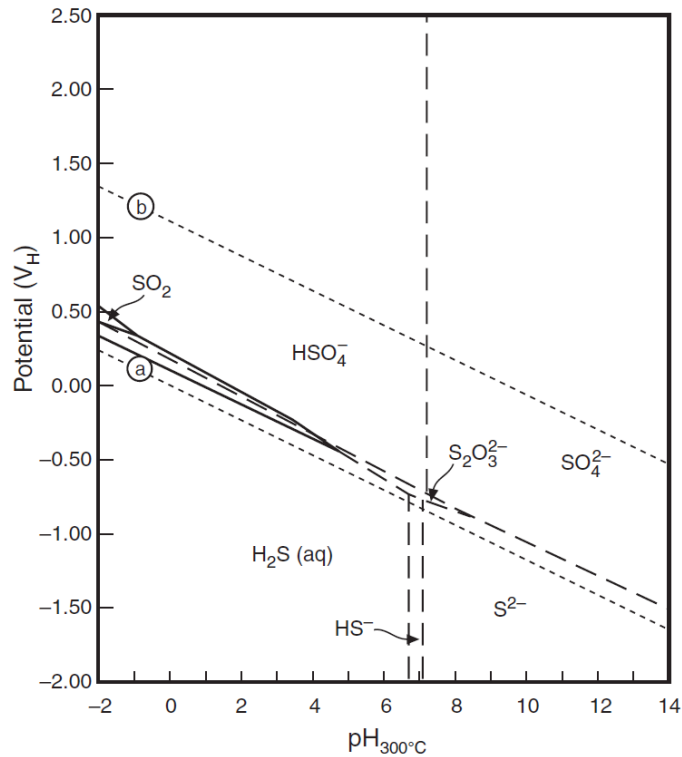


Figure 2.2 Potential vs. pH diagram for the stability of sulphur species in aqueous environments at 300°C [31]

Another reason for the low valence sulphur species present is from the reduction by Ni in the alloy. Figure 2.3 shows the potential vs. pH diagram at 25°C. It shows that NiS has good stability over a broad range of pH and potential.

This implies that the sulphates can be reduced by nickel to NiS due to its thermodynamic favor ability. It is also possible that Fe and Cr can reduce the sulphates to a low valence state.

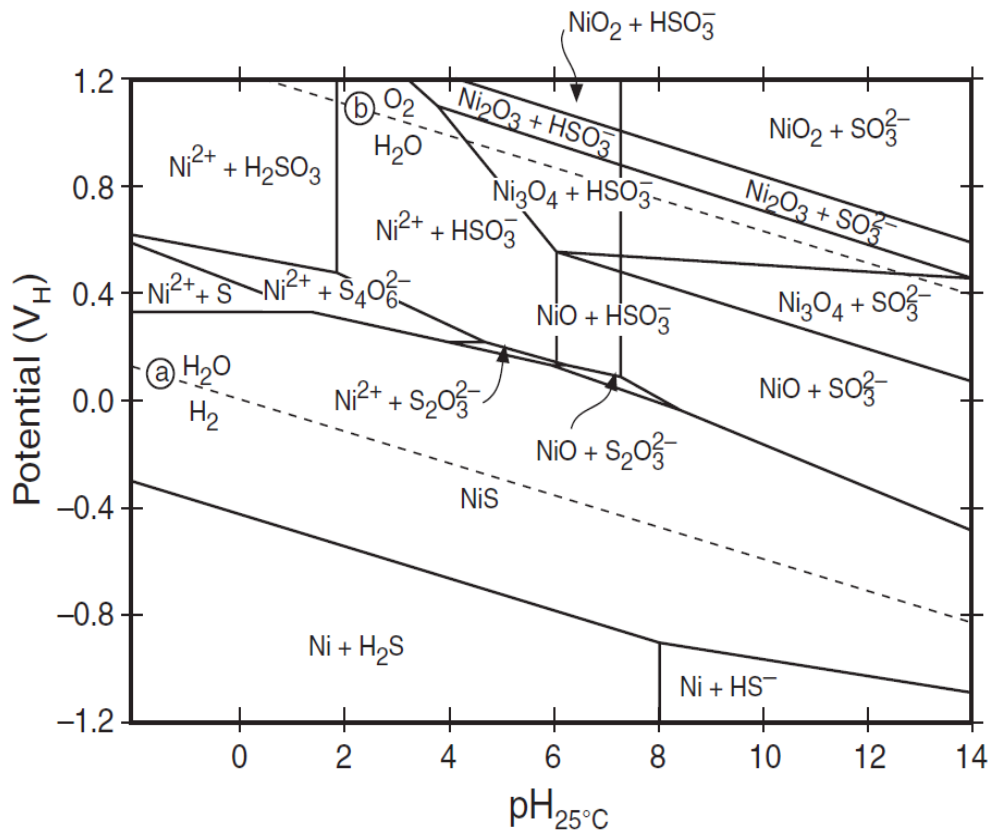


Figure 2.3 Potential vs. pH diagram for the stability of Ni-S-H₂O species in aqueous environments at 25 °C [31].

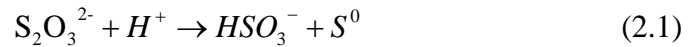
2.4.2 The effect of dissolved reduced sulfate species on SCC

The reduced state sulphur, has been known to interfere with the protective oxide films that form on high-nickel alloys such as those used as CANDU SG tubing materials. Reduced sulphur can cause intergranular attack and pitting of SG tubing over a wide pH range, by assisting in the breakdown of oxides.

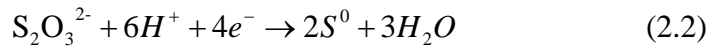
Reduced sulphur has also been found to increase the susceptibility to stress corrosion cracking of sensitized Alloy 600 at low temperatures, such as at operating conditions less than full power. However, the effect of the reduced sulphur species over the range of relevant pH has not been studied systematically.

The +6 sulphates and +4 valence sulphites, do not affect either hydrogen entry nor do they tend to accelerate general corrosion. However, sulphur species of lower valences, +2.5, +2, and -2 (tetrathionate, thiosulphate, and sulphide), have the tendency to accelerate the entry of hydrogen into metals and tend to accelerate general and localized corrosion [31].

Newman et al. investigated the effects of $S_2O_3^{2-}$, H_2S , $S_4O_6^{2-}$, SCN^- and SO_3^{2-} additions on the pitting behaviour of 304SS in 0.25 M NaCl solutions at pH values from 4.5 to 6 [32]. They found that thiosulfate had the greatest impact on decreasing the pitting potential. Thiosulfate was kinetically unstable and would form sulphur and sulfite ions in acidic solutions, shown in the Equation 2.1. Thiosulfate can also be electrochemically



reduced to sulphur and sulfide, shown in Equation 2.2 and 2.3. H_2S cannot electromigrate from the bulk solution into pits, so this means thiosulfate has a greater deterioration effect

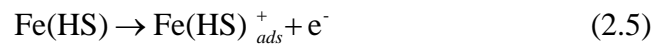


than H_2S . However, 0.5 M or higher concentration of $S_2O_3^{2-}$ was observed to inhibit the pitting behaviour, compared to the Cl^- only solutions. At higher

concentrations, the migration of $S_2O_3^{2-}$ into pit nuclei interfered with Cl^- accumulation and would mitigate or even prevent acidification via Equation 2.2. Marcus and coworkers proposed the main mechanism for the sulfur effects. It was found that a surface sulfur layer that was formed on the surface of the alloy prevents repassivation and promotes the dissolution kinetics of the alloy [33-35].

Mulford and Tromans [36] found that 1M thiosulfate solution did not lead to crevice corrosion of alloy 600 without the presence of Cl^- . Crevice corrosion initiated as micropits along polishing scratch marks, and then thiosulfate and Cl^- reportedly worked cooperatively to breakdown the passive film. They also proposed that after the passive film was damaged, thiosulfate was reduced to sulfide which accelerated the active dissolution of Ni.

Sury [37] investigated the role of H_2S on the electrochemical and corrosion behavior of Fe, Ni, Co and their alloys. It was proposed that H_2S acted as a catalyst due to its surface adsorption as either H_2S or HS^- . The formation of a surface catalyst was shown in the reaction Equations 2.4 to 2.6.



Iofa [38] and Bellaouchou et al. [39] proposed similar mechanisms for the catalytic effects of H_2S . The presence of H_2S also leads to an increase in the exchange current density for the hydrogen evolution reaction (HER) by acting as a proton transfer center.

Fang and Staehle [40] studied the effect of sulfur species on the stability of

Alloy 600MA at 95°C. Their results showed that decreasing valence decreases the breakdown potential and raises the passive current densities. The species $S_3O_4^{2-}$ and $S_2O_3^{2-}$ produce accelerated rates of reduction that retards the anodic behavior at lower potentials.

The mechanisms of the effects of $S_2O_3^{2-}$ on SCC have also been proposed by different researchers below. The crack on sensitized SS304 was detected to grow via discrete microfracture events at room temperature and the observations are more consistent with crack growth due to a hydrogen induced fracture mechanism rather than slip/dissolution [89], Chen et al. studied the SCC of type 321 SS under simulated petrochemical conditions containing $S_2O_3^{2-}$ and chloride, and it was found that TiC particles can possibly nucleate of SCC [90-91]. Upon plastic deformation of annealed and sensitized SS304, AFM results reveal that slip lines piled up at the grain boundaries which increase localized stresses at some grain boundaries, particularly at grain boundary triple points and grain boundary/twin boundary intersections [92]. In addition, some researchers proposed that a critical value of the $S_2O_3^{2-}$ concentration may exist for the initiation of SCC, which is contemplated based on SSRT experiments [93-94].

2.5 Lead-induced Stress Corrosion Cracking (PbSCC)

More and more pressurized water reactors (PWR) will be built to catch up with the increasing power supply demand [2]. On the SG secondary side, lead is a common impurity, which has a destructive effect on the degradation of SG tube alloys, such as Alloy 800. Both field experience and laboratory research told us

that all SG tube materials are susceptible to lead-induced stress corrosion cracking (PbSCC).

PbSCC was first investigated by Copson and Dean [3]. They showed that PbSCC was produced regardless of the form in which lead was used, and PbO induced SCC most rapidly. In 1972, Flint and Weldon reported their lead-containing environments used to evaluate alloys with higher chromium [4]. By the end of the 1970s, Pement, et al. [5] showed that Alloy 690, but not Alloy 600, would sustain SCC with PbO additives and that an arsenic additive would also produce SCC for Alloy 600 but not 690. In the middle 1980s, many more efforts were spent on the effect of Pb in SCC. In 1989, Agrawal and Paine identified sources of Pb in plants [6]. In the 1990s, polarization studies of Alloy 690 in a 1 M NaOH solution at 300 °C was undertaken by Kilian [7]. In 1997, the work by Takamastu, et al. demonstrated that PbSCC will propagate short distances if the specimens, which have been exposed previously to Pb environments, are later exposed without Pb in the environments. The dimensions of this effect are not clear but are important. In 2004, Staehle and Gorman provided a quantitative assessment of submodes of SCC on the secondary side of steam generator tubing in pressurized water reactors, including a short section on PbSCC [31].

There are many mechanisms proposed for PbSCC, but the actual mechanism is still under debate. In 1987, Kishida, et al proposed that the important reason for PbSCC was an increase in potential observed in lead-contaminated caustic environments [8].

In 1992, Sakai demonstrated that the presence of soluble lead enhanced the selective dissolution of nickel and also of iron from alloy 600 base metal. It suggested that an active electrochemical reaction between soluble lead and nickel/iron among alloy 600 constituents enhances the possibility of corrosion [9].

In 1998, Sakai showed that Alloy 690 had better corrosion resistance than alloy 600 in mildly acidic condition. They also used electrochemical measurements and constant extension rate test (CERT) to confirm that lead was incorporated into the oxide film of the alloys and caused disruption of the oxide film, resulting in an accelerated anodic selective dissolution of the metal elements (nickel and iron) [10]. Recently, Lu studied the effect of lead in steam generator tube degradation and made a comparison among alloy 600, 690, and 800 [77]. Lu and et al. investigated the correlation between film rupture ductility and PbSCC of alloy 800, and they found that the film fracture ductility decreased with rising potential and increasing lead impurity concentration [78].

The main goal of this research is to investigate the lead induced stress corrosion cracking of alloy 800 at high temperature. We will investigate the different crack propagation rates for both Pb-free and Pb contaminated conditions in autoclave chambers by a potential drop system. Slip-oxidation mechanism is a common explanation for the SCC of steam generators in lead free conditions, but the actual mechanism for lead contaminated conditions is still controversial. The combination of fracture mechanics, electrochemical measurements and materials characterizations will significantly advance our understanding of the role of lead in the SG SCC.

2.6 Film Rupture Theory

The mechanisms for SCC have been discussed for many years [11-21]. Some mechanisms were proposed as a pre-existing active path or a strain-assisted active path. In some other mechanisms, the various adsorption / absorption phenomena played an important role. After a decade's efforts, the major mechanisms have been narrowed to anodic dissolution, film-induced cleavage, and hydrogen brittlement (HE).

As mentioned in the previous sections, the anodic dissolution mechanism involves electrochemical reactions that consumed the specimen body. Hydrogen brittlement is the process by which various metals, most importantly high-strength steel, become brittle and crack following exposure to hydrogen. A typical HE mechanism starts with lone hydrogen atoms diffusing through the metal. When these hydrogen atoms re-combine in minuscule voids of the metal matrix to form hydrogen molecules, they create pressure from inside the cavity they are in. This pressure can increase to levels where the metal has reduced ductility and tensile strength up to the point where it cracks open [22]. The film-induced cleavage (FIC) mechanism involves a repeating process. A crack initiates in a brittle film can advance for a small distance before being arrested by ductile blunting. The crack propagates with the frequent occurrence described above.

Slip dissolution is another type of dissolution mechanism and it is used convincingly in many systems. Ford gave a detailed analysis of this model [23]. When the crack tip is ruptured, the crack propagation in many systems may be

correlated with oxidation. This is usually defined as the slip-dissolution mechanism, but slip-oxidation gives a more accurate concept since crack advance may be due to a combination of M/M^+ and M/MO oxidation reactions.

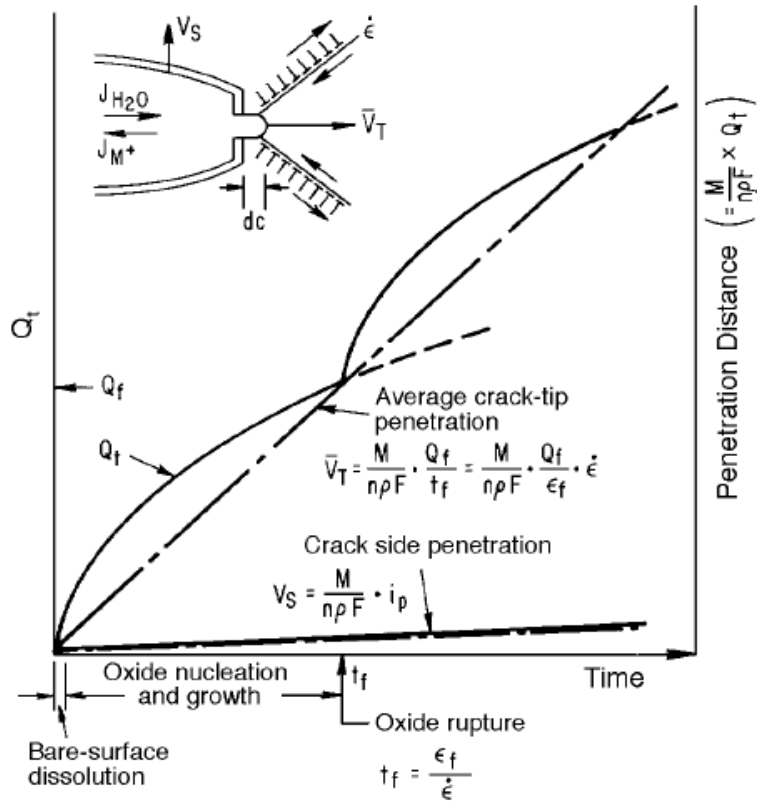


Figure 2.4 Schematic of Q_f vs. time relationship for a strained crack tip and unstrained crack sides [24].

Figure 2.4 gives a schematic representation of the change with time during the rupture of a protective film at the crack tip. The total oxidation rate will slow with time. The crack propagation rate (CPR) is controlled by the change in O_f with time and the frequency of film rupture at the strained crack tip. This frequency of film rupture is determined by the fracture strain of the film (ϵ_f) and crack-tip strain rate ($\dot{\epsilon}_{ct}$) in Equation 2.7.

$$f = \varepsilon_f / \dot{\varepsilon}_{ct} \quad (2.7)$$

By Faraday's law, the controlled CPR, \bar{V}_t , can be related to the oxidation charge density passed between film rupture processes. So we can obtain the following equation 2.8 as:

$$\bar{V}_t = \frac{M}{z\rho F} \frac{Q_f}{\varepsilon_f} \dot{\varepsilon}_{ct} \quad (2.8)$$

where M and ρ are the atomic weight and density of the crack-tip metal. F is Faraday's constant and z is the number of positive charges of the cation. The oxidation charge density on a bare surface changes with time, so the equation can also be written as:

$$\bar{V}_t = A(\dot{\varepsilon}_{ct})^n \quad (2.9)$$

where A and n are constants that depend upon the material and environment compositions at the crack tip and are related to the oxidation reaction rates or current densities [25].

2.7 Electrochemistry of localized corrosion

A polarization curve is often used to understand the passivity behavior. The polarization curve is an experimentally determined potential vs. current density diagram. A metal or alloy will develop a potential difference across its interface spontaneously, and it is called open circuit potential (E_{oc}). It represents

the potential at which the rates of anodic and cathodic reactions on the surface balance. The polarization curves can represent the effect of potential on the electrochemical kinetics, such as open circuit potential, passive potential range, primary passivation potential (E_{pp}), pitting potential (E_p), and transpassive potential (E_t), shown in Figure 2.5.

In most cases, linear increase of the potential of the interface from E_{oc} results in an exponential increase in the current density. By plotting the potential-current data on semi-logarithmic axes, such behavior appears as a straight line designated as the “active region” in the figure. The measured current density continues to increase to a maximum, I_{crit} , at E_{pp} (called the primary passivation potential) and then begins to decrease. This decrease in current density happens at the “active-passive transition”, meaning that dissolution of the metal has gone from a state of active dissolution to passive dissolution due to the formation of the passive film. The current density starts to drop at E_{pp} , and remains at low values, I_{pass} (the passive current density), for a certain range (the “passive potential range”). The potential at the point, from which current density increases again, is called transpassive potential (E_t). However, in acidified Cl^- solutions, the current density increase is observed at lower potential, and is accompanied by the formation of corrosion pits on the metal surface. That is why we call this potential a pitting potential (E_p). The polarization behavior of different materials is strongly dependent upon the electrolyte and alloy composition.

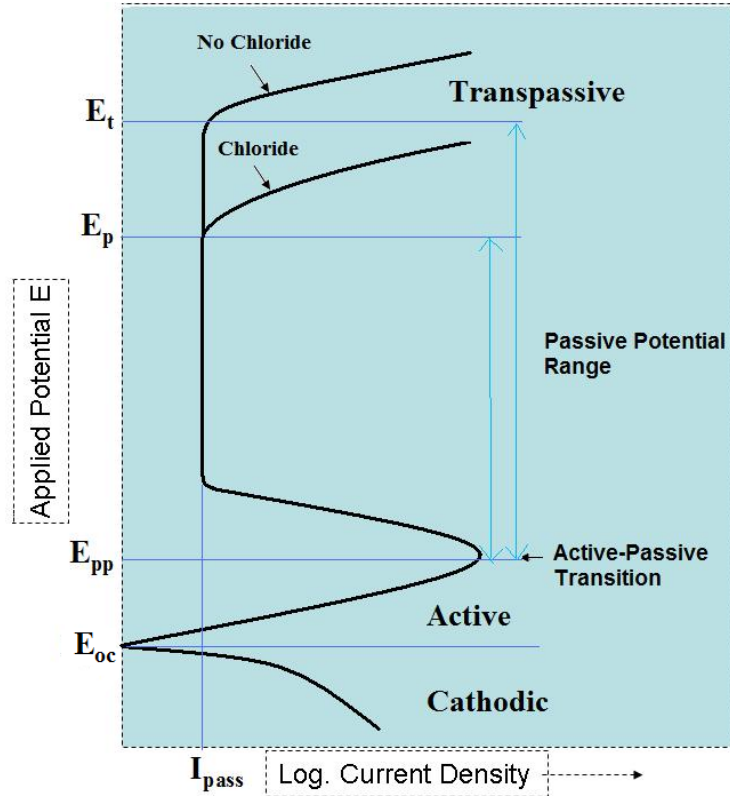


Figure 2.5 Schematic polarization curve (plot of applied potential vs. log current density) showing the active region, passive region, open circuit potential (E_{oc}), the primary passivation potential (E_{pp}), the pitting potential (E_p), the transpassive potential (E_t), and the critical current density (I_{crit})

2.8 Potential Drop Technique

2.8.1 Introduction

Potential drop techniques can be used to measure growth of a flaw or a crack in any conductive material. This technique involves connecting the

specimen to a circuit such that a constant current is flowing through it, then measuring the potential change in the specimen during the crack propagation process. The increased crack would change the geometry of the specimen, so the resistance of the specimen would change accordingly. Consequently, the change in potential would be correlated to crack growth.

Potential drop techniques can involve either alternating or direct currents. If a direct current is injected into the material, then the technique is known as a direct current potential drop / difference (DCPD) technique. If an alternating current is used, then it known as alternating current potential drop / difference (ACPD) technique. The ACPD technique was not investigated in the present research, and is thus not being discussed within this thesis.

Potential drop techniques have numerous applications beside basic crack detection. They have been successfully applied to fracture problems such as velocity measurement of fast running cleavage cracks and crack initiation detection in different environments. They can also be used in determination of slow crack growth rates under sustained loading, fatigue loading, constant displacement, stress corrosion cracking, hydrogen embrittlement, and creep [41]. The actual individual application techniques would depend upon the sensitivity of the crack measurements, the nature of the specimen, stress condition and the experimental environment.

The DCPD has been used by many researchers in attempts to investigate the crack propagation. It was reported by McKeighan and Smith that the first successful use of the potential drop method for crack length determination was by

Barnett and Troiano, who investigated the effect of hydrogen embrittlement in notched tension specimens of steel by DCPD [42, 43]. Vasatis and Pelloux investigated the crack initiation and propagation of creep specimens of IN-X750 under sustained load condition. They found that the crack initiation in the V-notched bars was controlled by creep deformation. The creep rupture, crack initiation, and crack propagation in the IN-X750 are controlled by the constrained cavity growth process [44]. Nekar Merah also used DCPD to monitor crack growth under high gross inelastic deformation (plastic and creep) conditions. They proposed a correction of the measured length at high temperature, based on the analysis of DCPD-NOD (notch opening displacement) [45]. In 1997, Oppermann, Hofstotter, and Keller [46] used a long-term DCPD in four nuclear power plants and the accuracies were evaluated. They found that the DCPD is suitable for inspecting and monitoring material regions such as, e.g. weld seams in pipework, for crack initiation and crack growth at power plant temperature using permanently installed potential probes. The total exposure to radiation can be reduced in comparison to other inspection methods.

Recently, the DCPD technique draws more attention in new applications. Tada evaluated the distribution of multiple circular cracks with random radii and angles by the DCPD method. He proposed a method for non-destructive evaluation of the distribution of circular cracks by DCPD and derived a relationship between the normalized potential difference and the crack radius, as well as crack angle. The relationship works well for any crack distribution condition discussed in their study [47]. Spitas and et al. investigated the real-time

measurement of the closed cracks propagating in Mode II (in plane shear). They derived a correlation between the crack propagation and the stress intensity factor K_{II} at high temperature. It also proved to be a successful non-destructive measurement method for fatigue crack growth [48]. The crack growth behavior of X-65 pipeline steel in near-neutral pH environments was investigated by Chen and Sutherby [49]. They found that the crack growth rate can be correlated with $\Delta K^2 K_{max}/f^{0.1}$. The determination of threshold $\Delta K^2 K_{max}/f^{0.1}$ values can demarcate the boundary between active growth and dormancy.

2.8.2 Theoretical Aspects of Direct Current Potential Drop

The DCPD technique is applied by inputting a direct current into a specimen, and measuring a potential difference across the crack. The current goes through the body of the specimen as opposed to along the surface skin as in the case of an alternating current. At a constant current, then the voltage value becomes a function of the resistance of the specimen indicating the crack growth behavior.

At certain temperatures, the major factors affecting DCPD measurements are the cross-sectional area of the direct current path, the length of the path, and the resistivity of the material. For a given test, the length of the current path was identical since the distance between the potential differences probes remained the same. The material, the distance between the probes and the environment were all kept constant, so that the resistivity of the material would only change if the temperature or the cross-sectional area of the current path changed.

Large currents are usually injected across the entire body of materials in the DCPD technique, causing specimen heating (therefore altering specimen physical properties). In addition, large currents can increase the danger of the working environment. One technique to avoid the increase in temperature related to the use of large currents is the use of thermally stabilized connections. Another method is to use the “reversed” DCPD technique. The reversing DCPD method was successfully used by Catlin et al. as early as 1985 [50]. A fundamentally different approach is to inject current locally, confining the potential distribution to the flawed area. This change in potential distribution allows the use of smaller currents. Costanza and Mohaupt have successfully used currents as low as 2.5 A, and this is 40 times lower than conventional DCPD techniques [51]. A possible limitation of the localized DCPD technique is detecting crack initiation in fatigue testing. In this case, the crack initiation sites are unknown and difficult to locate. This will make probe positioning a problem.

2.8.3 DCPD Calibration

DCPD calibration is very important in determining the relationship of voltage drop to crack depth. It can be done either experimentally, numerically or analytically. For situations where geometry is simple, analytical methods would be the best choice. For more complicated geometries, experimental calibration was often used to provide an easier and equally reliable method of determining the relationship between crack depth and voltage difference. In more critical situations, finite element analysis can be used to simulate a situation that is hard to

set up in reality, like unique geometry or extremely high temperature and pressure.

All voltage readings should be normalized regardless of the calibration being used. The potential normalization could minimize the system error, and remove any specimen dependent effect [52]. The normalized voltage can be achieved by dividing the voltage difference between measured voltage and reference voltage by the same reference voltage. The reference voltage can be the initial voltage value in the measurement or it can be obtained by measuring the voltage of the non-crack-growth specimen in the experimental condition. Sometimes, the reference voltage can be achieved by finite element analysis simulation.

Equation 2.10 describes the calculation of the voltage normalization as follows,

$$V_n = \frac{V - V_r}{V_r} \quad (2.10)$$

where: V_n = normalized potential (V)

V = signal voltage (V)

V_r = reference potential (V)

This procedure make the potential values entirely a function of the change in specimen resistance resulting from crack growth. Also, there is no unit for V_n , which makes the comparison between different experiments much more easier.

A similar approach was used by Pishva et al. [53] by defining a potential ratio parameter beta (β). This procedure was calibrated against crack length in

order to eliminate the effects of temperature, material and current fluctuations caused by system error. This parameter is defined as follows,

$$\beta = \frac{(V_{on} - V_{off})_{test}}{(V_{on} - V_{off})_{reference}} \quad (2.11)$$

where: V_{on} = potential drop when current is on (V)

V_{off} = potential drop when current is off (V)

Pishva et al. also expanded on Aker's work [54] by experimentally developing a calibration equation based on a/w (the area/width of a specimen) and β . They developed a room temperature calibration curve for nickel-based alloys and applied it to a different alloy at high temperature (550 °C). The actual crack sizes were consistent with the results by optical measurements.

The electrolyte-bath technique has also been used for calibration of a potential drop system [55, 56]. The procedure is based on the assumption that an electrolyte bath with the identical shape as the specimen can precisely model the current conducting process in the specimen, such as current distribution etc. Different electrodes are located at each end of the tank to simulate potential probes. Crack growth was simulated by inserting insulating material cut in the electrolyte-bath. The calibration method has many limitations as well. For example, it only applies when a uniform potential distribution was produced by the input current.

Another technique used to determine crack size is the use of conducting

paper. Hicks and Pickard [57] successfully used this technique to determine crack lengths. The assumption of this technique is that the current distribution is only a function of specimen shape, rather than the thickness. Another premise in this method is that we assume no crack tunnelling occurs, which means the surface crack length is a true length. Under these assumptions, a two dimensional conducting paper can represent the real specimen. The potential at different simulated crack lengths can be measured to produce a calibration curve.

Finite element methods have also been widely used in order to calibrate the DCPD technique since the current distribution can be modeled using Laplace's equation. This technique was successfully used by Ritchie and Bathe [58] and Gangloff et al. [59] for compact tension (CT) specimens. An obvious disadvantage of this technique is that various crack growth stages must be modeled to obtain the calibration data. However, it is relatively inexpensive to calibrate the DCPD by finite element methods since less experimental work is involved.

Recently, Belloni and et al. [60] set up a system for monitoring deep cracks in notched specimens in creep and fatigue laboratory tests. They studied the effect of thermoelectromotive force due to the interface resistance of the bimetallic connections (i.e., specimen-probe and probe-wire), and electrical field distribution in order to improve the experimental calibration. Merah [61] also worked on the DCPD calibration in creep-fatigue loading conditions. He calibrated the DCPD system at both room temperature and 600°C for SS-304 plate specimens. They introduced a correction factor, G , in the calibration function. The correction factor

takes into account mainly the difference in crack-tip plasticity at different temperatures.

2.8.4 Effect of Temperature on DCPD

Temperature has a significant effect upon the magnitude of the DCPD measurements. The potential fluctuation could be fatal with only a small temperature fluctuation. From Ohm's law,

$$V = I \cdot R \quad (2.12)$$

The resistance of a material can be described by the Equation 2.13 as follows,

$$R = \rho \cdot \frac{L}{A} \quad (2.13)$$

where ρ is the electrical resistivity of the material, and L and A are the length and cross-sectional area of the specimen, respectively. A change of temperature may result in a change in the resistivity of the material used in the system. If two measurements are taken on the same specimen at different temperatures, then we can use the equations below,

$$\frac{V_{T1}}{V_{T2}} = \frac{C}{C} \cdot \frac{\rho_{T1}}{\rho_{T2}} \quad (2.14)$$

$$\frac{V_{T1}}{V_{T2}} = \frac{\rho_{T1}}{\rho_{T2}} \quad (2.15)$$

In order to eliminate the effects of temperature and system errors, the normalization mentioned in the previous section can also be used. Jones and Frise found that the normalization of the data efficiently eliminates the effect of

temperature, while not affecting the potential increase due to crack propagation [62].

2.8.5 Applications of DCPD in detecting SCC propagation of nuclear materials

The applications of DCPD in nuclear materials have been used due to its capability to collect real-time data. In 1996, both DCPD and ACPD approaches were used by Fries and Sahney [79] to evaluate the fracture toughness properties of pressure tubing materials “cold-worked Zr-2.5Nb” in Canadian CANDU heavy water nuclear reactors, and it was found that DCPD gave satisfactory results on flat plate specimens of the material. Oppermann and his colleagues [80] engaged a long-time installation of DCPD methods to inspect and monitor the cracks on the internal surface of the pipework in both the laboratory and four nuclear power plants. The cracks found can be measured more accurately than was previously possible with conventional ultrasonic and radiographic inspections. The total exposure to radiation can also be reduced in comparison to other methods of inspection. In 2000, the DCPD method was also used by Hub and et al [81] in predicting the pipe failure in the nuclear power plants. It was considered an economical method in the replacement of a full-scale pipe test. A modified DCPD method was also used by Černý [82] in the measurement of subcritical growth of defects in large components of nuclear power plants at elevated temperatures. He found that high temperature is not a limiting factor for exact measurement of crack length if a compensation and computer controlled device is used. In 2006,

Lee et al [83] developed an on-line monitoring system for accelerated corrosion failures, which were observed in aged nuclear piping materials. The DCPD method was also integrated into this developed frame work to support the thickness measurement for a wide-area. Recently, Alexandreanu and et al [84] summarized crack growth rates and metallographic examination of Alloy 600 and Alloy 82/182 from field components tested in PWR environment, and the crack length was monitored by a DC potential drop system in this work. The report also presented the crack growth rate as a function of temperature between 290 °C and 350 °C.

2.9 Scanning Electrochemical Microscope (SECM)

2.9.1 Introduction

Scanning probe microscopy (SPM) technologies, including atomic force microscopy (AFM) and near-field scanning optical microscopy (NSOM), have been developed very quickly, since scanning tunneling microscopy (STM) was invented. Those techniques can provide localized electronic, topographic, photonic and phase information at the micro or nano-scale, or even atomic scale. As a result, these techniques are playing a more and more important role in surface analyses, surface fabrication, molecular imaging and surface modification.

Scanning electrochemical microscopy (SECM) is one of the powerful scanning probe microscopes that can be used for topographic imaging and mapping of chemical reactivity at interfaces. SECM relies on the amperometric

feedback current resulting from redox reactions at the tip electrode, so it requires the presence of an electroactive species in solution. In this technique, an ultramicroelectrode (UME) is used as the scanning probe, which is also called a “tip”. In the SECM experiments, an ultramicroelectrode (UME) with a diameter of 2 μm to 25 μm is widely used as a scanning probe. The UMEs are fabricated as a conductive disk of noble metal or carbon fiber in an insulating sheath of glass or polymer. The current at this probe is measured as a signal, when the tip is held or moved in a solution in the vicinity of a substrate, which can be different types of solid surfaces (e.g., metal, glass, thin film, polymer and biological material) or liquids (e.g., mercury, immiscible oil, etc.).

The movement of the tip is usually controlled by drivers based on piezoelectric elements, which is widely used in STM. In most cases, inchworm drivers are used, because they can move larger distance than simple piezoelectric tube scanners. When the higher resolution is needed, piezoelectric pushers can be combined with inchworm drivers. Piezoelectric pushers behave as a precise nm scale drivers, while inchworms provide coarse drivers [63-65].

Figure 2.6 illustrates the setup of a SECM system. There are three main parts in the SCEM. The first one is the electrochemical system including bipotentiostat and electrolyte cell with working electrode (WE), reference electrode (RE) and counter electrode (CE). A bipotentiostat is more often used in SECM than a single potentiostat since the potential on both the tip and substrate (sample) should be controlled in the experiments in most cases. The reference electrode is usually made of a silver wire coated with silver chloride immersed in

a saturated potassium chloride solution, called KCl-saturated Ag/AgCl RE. The counter electrode is normally a Pt wire or plate, whose area is larger than the working electrode. The second part is the positioning system including three dimension piezo or inchworm positioner and their controller. Their functions were discussed in the previous paragraph. The third part is the data acquisition system, including the computer and the related interfaces to record the data. The computer is also used to collect the tip 3D position data, the tip current and the substrate current data. To achieve better performance, the SECM instrument is usually set up inside a Faraday cage on a vibration-isolated optical table to avoid environmental vibration and electromagnetic noise, especially for high resolution and low tip current operation. In our work, alloy 800 specimen is used, to which can be applied a stress by the C-Ring configuration. The applied stress by C-Ring will be discussed in the Chapter 3.

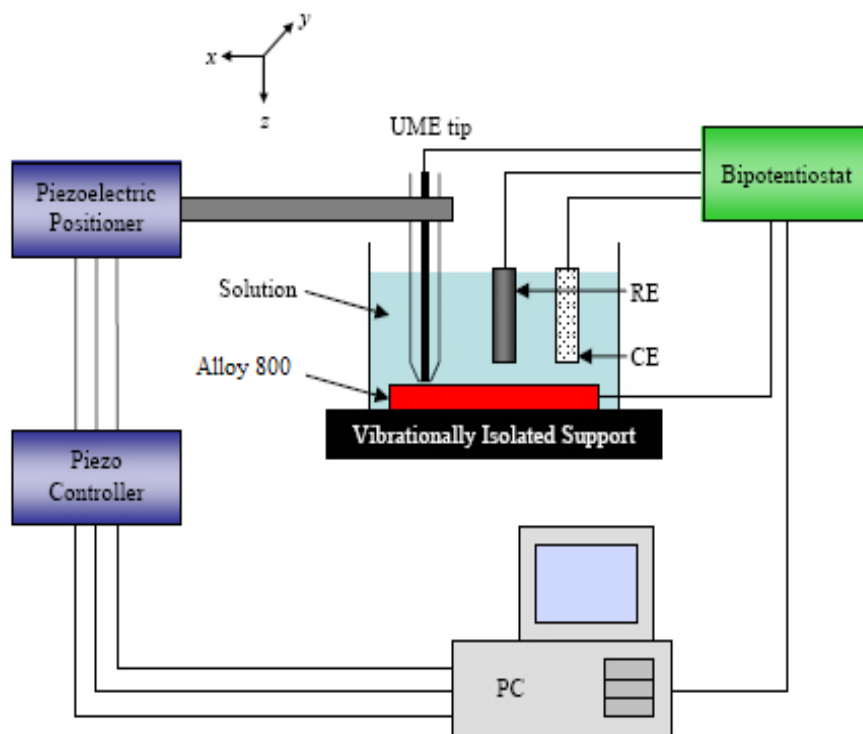


Figure 2.6 Schematic Illustration of a SECM setup in our work

2.9.2 Principles of SECM

2.9.2.1 Ultramicroelectrodes

An understanding of electrochemistry at small electrodes will help understand the operation of the SECM and the quantitative aspects of measurements with this instrument. Take a simplified electrochemical experimental setup for an example, as shown in Figure 2.7. The solution contains a species, O (oxidized state), at a concentration of c ; a supporting electrolyte is used to decrease the solution resistance. When a suitable potential is applied on UME, a reduction reaction happens on the UME (2.16). In the electrochemical

cell, the counter electrode completes the circuit via the power supply.



A plot of the current flowing as a function of the potential of the UME is called a voltammogram, which looks like an S-shaped curve, shown in Figure 2.8. In Figure 2.8, the current eventually reaches a limiting value that is completely controlled by the rate of mass transfer, with the hemispherical diffusion of O species from the bulk solution to the electrode surface, where the electrochemical reaction has decreased its concentration to essentially zero. This steady-state diffusion-controlled current when the tip is far from a surface is given by [66]:

$$i_{T,\infty} = 4nFDca \quad (2.17)$$

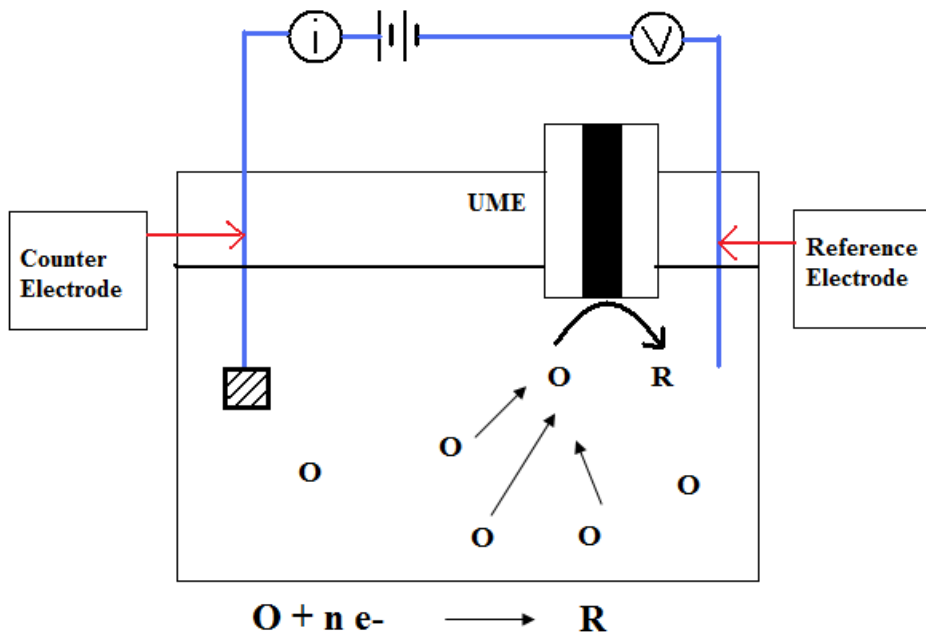


Figure 2.7 Schematic diagram of a cell for ultramicroelectrode voltammetry.

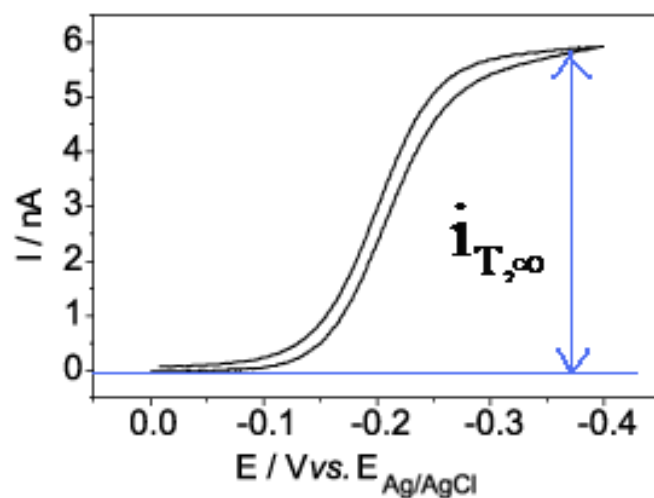


Figure 2.8 Typical voltammogram for an ultramicroelectrode

where F is the Faraday constant, D is the diffusion coefficient of species O , n is the number of electrons involved in Equation 2.16, c is the oxidation species concentration, and a is the radius of a conductive disk of UME. The disk-shaped electrodes show the best sensitivity, so they are widely used in SECM experiments. The current at a small disk reaches steady state in a relatively short time. For instance, a $10\ \mu\text{m}$ radius disk can reach steady state in a fraction of a second [70, 71].

2.9.2.2 Feedback Mode

There are several modes of operation of the SECM, like tip generation/substrate collection (TG/SC), substrate generation/tip collection (SG/TC) and feedback mode. The most frequent mode of operation of the SECM is the feedback mode, so we will mainly focus on this mode. Only the tip current

is monitored in feedback mode. The tip current is also perturbed by the presence of the substrates by blockage of the diffusion of solution species to the tip (negative feedback, insulating surface) or by regeneration of redox species at the substrate (positive feedback, conductive surface). Both electrically insulating and conducting surfaces can be studied under this mode, and it makes possible imaging of surfaces and the reactions that occur locally. Bard and Kwak first described this mode of operation with surface imaging, as well as the apparatus and theory in the late 1980s [67-69].

By solving the diffusion equations for the situation of a disk electrode and a planar substrate, we can obtain a quantitative description of approach curves [70]. The typical approach curves for a conductive substrate and insulating substrate are different from each other. In the conductive case, the rate of regeneration of O species from R is unlimited, but the rate of regeneration of O species in the insulating substrate is essentially zero. Figure 2.9 shows typical approach curves for both conductive and insulating situations. The tip current is normalized by the current obtained in the bulk solution, and the distance is normalized by the tip radius:

$$I = i_{ss} / i_0; L = d / a \quad (2.18)$$

where I is the normalized tip current, i_{ss} is the real tip current, i_0 is the tip current obtained in the bulk solution, L is the normalized tip-substrate distance, d is the real tip-substrate distance and a is the tip radius. The plot does not depend upon the diffusion coefficient and concentration of redox species, since only dimensionless variables are involved. If the substrate is between conductive and

insulating conditions, such as a semiconductor, the PACs will be between those two limiting cases. The rate constant of reaction equation 2.19 can be determined from their PACs, which indicates the electron transfer behaviour on the substrate.



2.9.2.3 SECM Surface Imaging

SECM images can be obtained by plotting the current, recorded by scanning the SECM tip in the vicinity of the x-y planes. The lateral resolution of the image depends upon the tip size more than the resolution of inchworm or piezo positioners used in the instrument [66]. It has been proven in the experiments that the smaller the tip-to-substrate distance is, the clearer the image will be [70]. SECM images show the unique surface information of in-situ electrochemical properties. The practical scan range of SECM varies from 4 μ to the physical limitations of the positioning device [71]. The surface chemical reactivity can be obtained from the SECM images. If the surface is so well polished that the surface can be considered as flat, the SECM images of a sample surface can be considered to represent only the localized chemical information, because the topographic signal is much smaller than the signal from chemical responses.

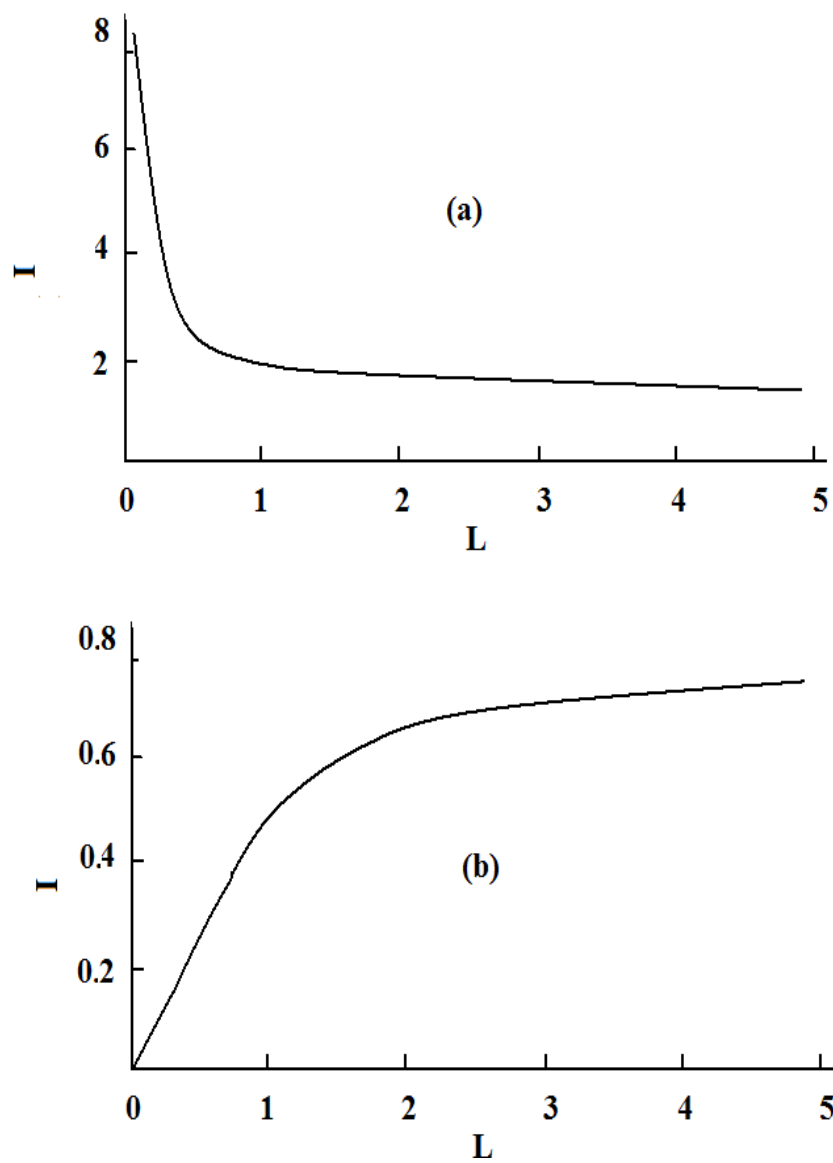


Figure 2.9 Typical probe approach curves, diffusion-controlled steady-state tip current as a function of tip-substrate separation distance. (a) Substrate is a conductor; (b) Substrate is an insulator.

2.9.3 Applications of SECM

SECM is a powerful and useful surface analytical technique for semi-quantitative and qualitative investigations of interfacial physical and chemical processes in many fields, such as cell biological studies, surface modifications and corrosion science.

There are three major application fields for SECM. The first one is to determine the electron transfer or ion transfer kinetics at an interface. The second is to record chemical images of a surface by plotting the tip current vs. the corresponding positions. The third one is surface modification or nanometer/submicrometer fabrications by deposition of metals or other materials.

In this work, we will discuss the SECM applications in corrosion studies. SECM methodology is ideally suited to investigating the phenomena underpinning corrosion processes for the following reasons. First of all, it is a technique that is applicable to insulating and conducting surfaces, and the high lateral resolution enable surface structural effects to be correlated with chemical activity. In addition, the UME tip can be used to initiate the reaction and to detect the corrosion products, and the tip and substrate current can also provide quantitative information on the processes.

On a corroding surface, some sites which are susceptible to pit initiation are considered as pitting precursor sites (PPS). White and coworkers investigated the relationship between electroactivity and pitting precursor sites on a Ti foil surface by SECM [72, 73]. The SECM images revealed some microscopic sites where the local Br_2 concentration was relatively higher. The video images were

compared with the SECM in identifying the pitting initiation spots. Their studies were the first experimental evidence of a correlation between electrochemical activity of the surface and the subsequent occurrence of oxide film breakdown. Garfias-Mesias et al. also used the SECM to identify pitting precursor sites on the surface of polycrystalline Ti covered with a 50 Å TiO₂ thin film. They found that Fe(CN)₆⁴⁻ is the most reliable mediator, compared to Br⁻ [74].

Another attractive advantage of the SECM is its ability to electrogenerate a local solution species with known concentration by positioning the UME tip close to a target interface. Wipf and Still generated a local concentration of the Cl⁻ ion in close proximity to passivated iron [75] and stainless steel [76]. The sample dissolved was detected by substrate current and the dissolution products were detected cathodically by tip current.

As mentioned before, the SECM can also be used for chemical imaging of active pitting corrosion spots. The active pitting corrosion on the surface of 304 stainless steel was imaged by Wipf [76]. A 12.5 µm radius Au tip electrode was scanned on the surface of a corrosion pit at an initial tip-substrate separation of 20 space µm. The heterogeneous current distribution in the pit indicated that the rate of corrosion is non-uniform.

2.10 Summary

To understand passive film formation and the reduced sulfate SCC susceptibility of alloy materials, localized electrochemical surface reactivity

information is important. Surface characterization methods have been widely used in the corrosion research, such as SEM, EDX, AFM and Kelvin probing method [30-38], but they can only slightly provide *in-situ* localized electrochemical information at the micro- and submicro-scale. In this work, scanning electrochemical microscopy (SECM) has been used for the first time to investigate the *in-situ* electrochemical behavior of alloy 800 in reduced sulfate simulated crevice solutions, by providing information on local electrochemical reactivity, microstructures, localized dissolution and corrosion. The combination of scratch tests and electrochemical measurements were also used to study the role of $S_2O_3^{2-}$ in corrosion initiation and its synergistic effects with applied stress on alloy 800 specimens.

PbSCC have been a serious issue in nuclear power plants and lots of efforts have been made to investigate the role of lead in the stress corrosion cracking of steam generators [3-7, 9, 10, 77, 78]. However, the mechanisms for lead-induced passivity-degradation are still not fully understood, and no well-accepted theory has been reported to describe this degradation mechanism [31, 95-97]. In this work, the effect of Pb on the crack propagation rates of alloy 800 has been studied for the first time by using a potential drop system at 300°. It is also the first investigation of the crack propagation mechanism of alloy 800 by combining fracture mechanism, film rupture theory and crack growth behavior.

References

1. (a) National Energy Board, *Report of Public Inquiry concerning Stress Corrosion Cracking on Canadian Oil and Gas Pipelines*, MH-2-95, November 1996. (b) B. N. Leis and R. J. Eiber, “*Stress-Corrosion Cracking on Gas-Transmission pipelines: History, Causes, and Mitigation*”, Invited paper, Proceedings, First International Business Conference on Onshore Pipelines, Berlin, December 1997. (c) Michael Baker Jr., Inc., pp 15-28 Chapter 4, *Stress Corrosion Cracking Study*, Department of Transportation Research and Special Programs Administration Office of Pipeline Safety, TPO Number 8.
2. F. P. Ford, “*Technical and Management Challenges Associated with Structural Materials Degradation in Nuclear Reactors in the Future*”, proc. 13th Environmental Degradation of Materials in Nuclear Power Systems, Canadian Nuclear Society, 2007.
3. H.R. Copson, S.W. Dean, *Corrosion* 21 (1965): p. 1.
4. G.N. Flint, B.A. Weldon, “*Some Investigations into the Stress Corrosion Behaviour of Fe-Ni-Cr Alloys in High-Temperature Water,*” *Conf. Cycle on Chemistry of Water and Aqueous Corrosion in Steam Generators* (Conventional and Nuclear (Ecuelles, France: Electricite de France, 1972), p. 17.
5. F.W. Pement, I.L.W. Wilson, R.G. Aspden, *Mater. Perform.* 19 (1980): p. 43.
6. A.K. Agrawal, J.P.N. Paine, “*Lead Cracking of Alloy 600—A Review,*” *Proc. 4th Int. Symp. on Environmental Degradation of Materials in Nuclear*

- Power Systems—Water Reactors*, ed. D. Cubicciotti (Houston, TX: NACE, 1990), p. 7-1.
7. R. Kilian, “*Influence of Lead on the SCC Behavior of SG Tubing Materials*,” IAEA Specialists Meeting on Steam Generator Problems and Replacement (Madrid, Spain: International Atomic Energy Agency, 1993), p. 137.
 8. A. Kishida, et al, *Proc. 3rd int. Symp. Environmental Degradation of Materials in Nuclear Power Systems – Water Reactors*, Traverse City, Michigan (Warrendale. PA: TMS, 1987), p. 465.
 9. T. Sakai, K. Aoki, T. Shigemitsu, Y. Kishi, *Corrosion* 48 (1992): p. 745.
 10. T. Sakai, N. Nakagomi, T. Kikuchi, K.Aoki, F. Nakayasu and K. Ymakawa, *Corrosion*, Vol. 54, No.7, (1998): p. 515.
 11. “*Environmental-Sensitive Mechanical Behavior*,” Baltimore, Maryland, eds. A.R.C. Westwood, N.S. Stoloff (Gordon and Branch, 1965).
 12. “*Fundamental Aspects of Stress Corrosion Cracking*,” Ohio State University, eds. R.W. Staehle, A.J. Forty, D. van Rooyen (Houston, TX: NACE, 1967).
 13. “*Theory of Stress Corrosion Cracking*,” Ericera, Portugal, ed. J.C. Scully (Brussels, Belgium: NATO, 1971).
 14. “*Corrosion Fatigue Chemistry, Mechanics, and Microstructure*,” University of Connecticut, Storrs, June 1971, eds. O. Devereaux, A.J. McEvily, R.W. Staehle (Houston, TX: NACE, 1972).
 15. *L’Hydrogene Dans Les Metaux*, ed. M.P. Bastein (Paris, France: Science et Industrie, 1972).

16. Hydrogen in Metals, ed. I.M. Bernstein, W.W. Thompson (Materials Park, OH: ASM, 1973).
17. “*Stress Corrosion Cracking and Hydrogen Embrittlement of Iron-Based Alloys*,” Firminy, France, June 1973, eds. R.W. Staehle, J. Hochmann, R.D. McCright, J.E. Slater (Houston, TX: NACE, 1977).
18. “*Effect of Hydrogen on Behavior of Materials*,” Jackson Lake, Wyoming, eds. A.W. Thompson, I.M. Bernstein (New York, NY: AIME, 1975).
19. “*Surface Effects on Crystal Plasticity*,” Hohegeiss, Germany, September 1975, eds. R.M. Latanision, J.T. Fourie (Noordhof- Leyden, 1977).
20. “*Mechanisms of Environment-Sensitive Cracking of Materials*,” University of Surrey, United Kingdom, eds. P.R. Swann, F.P. Ford, A.R.C. Westwood (Warrendale, PA: TMS, 1977).
21. “Corrosion Fatigue,” *Met. Sci.* 13 (1979).
22. Jewett, R.P. *Hydrogen Environment Embrittlement of Metals*. NASA CR-2163 (1973).
23. F.P. Ford, *Quantitative prediction of environmentally assisted cracking*, *Corrosion* 52 (1996) (5), pp. 375.
24. F.P. Ford, “*Mechanisms of Environmental Cracking Peculiar to the Power Generation Industry*,” EPRI Report NP2589 (Palo Alto, CA: EPRI, 1982).
25. F.P. Ford, “*The Crack-Tip System and Its Relevance to the Prediction of Environmentally Assisted Cracking*,” Proc. 1st Int. Conf. Environment-Induced Cracking of Metals, Kohler, Wisconsin (Houston, TX: NACE, 1988), p. 139.
26. Wenk, R. L., 1974, “*Field Investigation of Stress Corrosion Cracking*,” 5th

- Symposium on Line Pipe Research, American Gas Association, Inc., Arlington, VA, Catalog No. L30174, Paper No. T.
27. Justice, J. T., and Mackenzie, J. D., 1988, “*Progress in the Control of Stress Corrosion Cracking in a 914 mm O.D. Gas Transmission Pipeline,*” Proc. NG-18/EPRG Seventh Biennial Joint Technical Meeting on Line Pipe Research, Pipeline Research Committee of the American Gas Association, Arlington, VA, Paper No. 28.
 28. R.A. Cottis from Corrosion and Protection Centre, UMIST, “*Guides to Good Practice in corrosion control---- Stress Corrosion Cracking*”, an update of a US Department of Trade and Industry publication.
 29. M. Huang, *Use of ChemSolv to predict crevice chemistry in ACR-1000 SG*, Atomic Energy of Canada Ltd. Report, 10820-36000-470-001, Revision 0, 2009 January.
 30. M. Huang, *Test Plan for ACR-1000 Crevice Chemistry Experiments*, Atomic Energy of Canada Ltd. Report, 10820-33110-430-005, Revision 0, 2008 January.
 31. R. W. Staehle and J.A. Gorman, *Quantitative Assessment of Submodes of Stress Corrosion Cracking on the Secondary Side of Steam Generator Tubing in Pressurized Water Reactors: Part 3*, Corrosion, 60(2), 2004, p.115.
 32. R.C. Newman, H.S. Isaacs and B. Alman, Corrosion, 38, (1982), p.61.
 33. P. Marcus and H. Talah, 11th Int. Corrosion Congress, 5, (1990), p.263.
 34. P. Marcus and J. Oudar, Chemistry and Physics and Fracture, eds, R. M. Latanision and R. H. Jones, *Martinus Nijhoff*, Boston, MA, (1987), p.670.

35. P. Marcus, *J. Chem. Phys.*, 88, (1991), p.1697.
36. S.J. Mulford and D. Tromans, *Corrosion*, 44, (1988), p.891.
37. P. Sury, *Corrosion Science*, 16, (1976), p. 879.
38. Z. A. Iofa, *Zashchita Metallov.*, 6, (1970), p. 491.
39. A. Bellaouchou, G. Guenbour and A. Benbachir, *Corrosion*, 49, (1993), p. 656.
40. Z. Fang, R.W. Staehle, *Corrosion*, 55, (1999), p. 355.
41. G. H. Aronson and R. O. Ritchie, "Optimization of the Electrical Potential Technique for Crac Growth Monitoring in Compact Test Pieces Using Finite Element Analysis," *Journal of Testing and Evaluation*, JTEVA, Volume 7, No. 4, July, (1979), p. 208.
42. P. C. McKeighan, C. P. Tabrett, and D. J. Smith, "*The influence of Crack Deflection on Bifurcation on DC Potential Drop Calibration*," Special Applications and Advanced Techniques for Crack Size Determination, ASTM STP 1251, J. J. Rushau and J. K. Donald, Eds., Amercian Society for Testing and Materials, Philadelphia, (1995), p. 51.
43. W. J. Barnett, and A. R. Trioano, "*Crack propagation in the Hydrogen Induced Brittle Fracture of Steel*," *Transactions, American Institute of Mining, Metallurgical, and Electronic Engineers*, Volume 20, No. 4, (1957), p. 486.
44. I. P. Vasatis and R. M. Pelloux, *Metallurgical Transactions A*, Volume 19A, April (1988), p. 863.
45. Merah, N., "DC Potential Drop Calibration in Creep-Fatigue Loading Conditions," *Journal of Testing and Evaluation*, JTEVA, Vol. 28, No. 4, July

- 2000, pp. 301–306.
46. W. Oppermann, P. Hofstetter, H.P. Keller, *Nuclear Engineering and Design* 174 (1997), p. 287.
 47. N. Tada, *International Journal of Fracture*, 141 (2006), p. 49.
 48. V. Spitas et al., *Measurement* 41 (2008), p. 424.
 49. W. Chen and R. L. Sutherby, *Metallurgical and Materials Transactions A*, Volume 38A, June, (2007), p. 1260.
 50. W. R. Catlin, D. C. Lord, T. A. Prater and L. F. Coffin, “The Reversing DC Electrical Potential Method,” *Automated Test Methods for Fracture and Fatigue Crack Growth*, ASTM STP 877, W. H. Cullen, R. W. Landgraf, L. R. Daisand, and J. H. Underwood, Eds., American Society for Testing and Materials, Philadelphia, Pennsylvania, (1985), p. 67.
 51. V. Costanza, U. H. Mohaupt, “A Local Field Potential Drop Crack Measurement System for Sizing and Characterizing Cracks,” Abstracts and Summaries of Canadian Fracture Conference 21, J. R. Mathews ed., Defence Research Establishment Atlantic, Halifax, Nova Scotia, April, (1990), p. 350.
 52. Wei, R. P. and Bazill, R. L., “An Assessment of AC and DC potential Systems for Monitoring Fatigue Crack Growth,” *Fatigue Crack Growth Measurement and Data Analysis*, ASTM STP 738, S. J. Hudak Jr., and R. J. Bucci, eds., American Society for Testing and Materials, Philadelphia, Pennsylvania, (1981), p. 103.
 53. Pishva, M. R., Bellinger, N. C., Terada, T., and Koul, A. K., “DCPD Technique for Crack Length Measurements at Elevated Temperatures,”

- Report No. LTR-ST-1635, National Aeronautical Establishment, National Research Council, Ottawa, Ontario, October, (1987).
54. Aker, G. F., “*A Damage Tolerance Approach for the Life Extension of J85-CAN 40/15 Compressor Disks,*” Master’s Thesis, Carleton University, Ottawa, Ontario, (1986).
55. Burns, D. J., Pick, R. J., and Romilly, D., “*A Calibration Technique for the DC Potential Drop Method of Monitoring Three Dimensional Crack Growth,*” Modelling Problems in Crack Tip Mechanics, Conference Proceedings, Waterloo, Ontario, August, (1993), p. 287.
56. Soboyejo, W. O., Reed, R. C., and Knott, J. F., “*On the Calibration of the Direct Current Potential Difference Method for the Determination of Semi-Elliptical Crack Lengths,*” International Journal of Fracture, Volume 44, (1990), p. 27.
57. Hicks, M. A. and Pickard, A. C., “*A Comparison of Theoretical and Experimental Methods of Calibrating the Electrical Potential Drop Technique for Crack Length Determination,*” International Journal of Fracture, Volume 20, (1982), p. 91.
58. Ritchie, R. O. and Bathe, K. J., “*On the Calibration of the Electrical Potential Technique for Monitoring Crack Growth Using Finite Element Methods,*” International Journal of Fracture, Volume 15, February, (1979), p.47.
59. Gangloff, R. P., Slavik, D. C., Piascik, R. S., and Van Stone, R. H., “*Direct Current Electrical Potential Measurement of the Growth of Small Cracks,*” Small-Crack Test methods, ASTM STP 1149, J. M. Larsen and J. E. Allison,

- eds., American Society of Testing and Materials, Philadelphia Pennsylvania, (1992), p.116.
60. G. Belloni, E. Gariboldi A. Lo Conte, M. Tono, and P. Speranzoso, "On the Experimental Calibration of a Potential Drop System for Crack Length Measurements in a Compact Tension Specimen," *Journal of Testing and Evaluation*, JTEVA, Vol. 30, No. 6, November (2002), p. 1.
61. Merah, N., "DC Potential Drop Calibration in Creep-Fatigue Loading Conditions," *Journal of Testing and Evaluation*, JTEVA, Vol. 28, No. 4, July (2000), p. 301.
62. Jones, K. I., and Frise, P. R., "Temperature Effects on DC potential Drop Measurements Made on a Zirconium Alloy Plate Specimen," *INSIGHT*, Volume 38, No. 5, May 1996.
63. A. J. Bard, F.-R. F. Fan, D. T. Pierce, P. R. Unwin, D. O. Wipf, and F. Zhou, *Science* 254, (1991), p.68.
64. A. J. Bard, F.-R. F. Fan, and M. V. Mirkin, in *Electroanalytical Chemistry*, Vol. 18, A. J. Bard, ed., Marcel Dekker, New York, (1994), p. 243.
65. M. Area, A. J. Bard, B. R. Horrocks, T. C. Richards, and D. A. Treichel, *Analyst* 779, (1994), p.719.
66. Bard, A. J.; Mirkin, M. V.; Editors, *Scanning Electrochemical Microscopy*, (2001), p. 650.
67. A. J. Bard, F. R. F. Fan, J. Kwak, and O. Lev, *Anal. Chem.* 61, (1989), p. 132.
68. J. Kwak and A. J. Bard, *Anal. Chem.* 61, (1989), p. 1221.
69. J. Kwak and A. J. Bard, *Anal. Chem.* 61, (1989), p.1794.

70. Zhu, R.; Ding, Z., *Canadian Journal of Chemistry*, 83, (2005), p. 1779.
71. Wipf, D. O., *Instrumentation In Scanning Electrochemical Microscopy*; Bard, A. J., Mirkin, M. V., Eds., Marcel Dekke: New York, (2001), p 17.
72. N Casillas, SJ Charlesbois, WH Smyrl, HS White. *J Electrochem Soc* 140: (1993), p. 142.
73. N Casillas, SJ Charlesbois, WH Smyrl, HS White. *J Electrochem Soc* 141: (1994), p. 636.
74. Lf Garfias-Mesias, M Aodan, PI James, WH Smyrl, *J Electrochem Soc* 145: (1998), p. 2005.
75. JW Still, DO Wipf. *J Electrochem Soc* 144: (1997), p. 2657.
76. DO Wipf. *Colloids Surfaces A Physicochem Eng Aspects* 93: (1994), p. 251.
77. Y.C. Lu, Effect Of Lead Contamination On Steam Generator Tube Degradation, *Proceedings of 12th International Conference on Environmental Degradation of Materials in Nuclear Power Systems - Water Reactors* Edited by TMS (The Minerals, Metals & Materials Society), (2005)
78. B.T. Lu, J.L. Luo, Y.C. Lu, *Electrochimica Acta*, 53(12), (2008), p. 4122.
79. P.R. Frise, R. Sahney, *INSIGHT*, Volume 38, 2, (1996), p. 96.
80. W. Oppermann, P. Hofstötter, H.P. Keller, *Nuclear Engineering and Design*, 174 (1997), p. 287.
81. N.S. Nuh, H.J. Cha, J.B. Choi, Y.J. Kim, C.R. Pyo, “Fracture and Strength of Solids, Pts 1 & 2”, *Key Engineering Materials*, Volume 183-1 (2000), p. 655.
82. Ivo Černý, *International Journal of Pressure Vessels and Piping*, 78 (2001), p. 893.

83. Na Young Lee , Seung Gi Lee, Kyung Ha Ryu, Il Soon Hwang, *Nuclear Engineering and Design*, 237 (2007), p. 761.
84. B. Alexandreanu, O.K. Chopra, and W. J. Shack, *Crack Growth Rates and Metallographic Examinations of Alloy 600 and Alloy 82/182 from Field Components and Laboratory Materials Tested in PWR Environments*, NUREG/CR-6964, ANL-07/12, Argonne National Laboratory, (2008).
85. R.W. Staehle and A.J. Forty, *Fundamental Aspects of Stress Corrosion Cracking*, eds., ASTM, Philadelphia, PA, (1969), p. 337.
86. R.N. Parkins, *Metall. Rev.*, vol.35, (1964), p. 201.
87. H.K. Birnbaum, I.M. Robertson, P. Sofronis, D. Teter, *Mechanisms of hydrogen related fracture. A review*, Proc. 2nd Int. Conf. Corrosion Deformation Interaction, The Institute of Materials, London (1997), p. 172.
88. Balch, D.K., et al., *Microstructural Effects on Hydrogen-Assisted Fracture of Austenitic Stainless Steel Welds*, in Corrosion 2004, 04561, NACE International, Houston, TX, 1-12, (2004).
89. M. Gomez-Duran and D. D. Macdonald, Stress corrosion cracking of sensitized Type 304 stainless steel in thiosulfate solution: I. Fate of the coupling current, *Corros. Sci.* 45 (2003), p. 1455.
90. Y. Y. Chen, H. C. Shih, Y. M. Liou, L. H. Wang, and J. C. Oung, Stress corrosion cracking of type 321 stainless steels under simulated petrochemical conditions containing thiosulfate and chloride, *Corrosion* 62 (2006), p. 781.
91. Y. Y. Chen, Y. M. Liou and H. C. Shih, Stress corrosion cracking of type 321 stainless steels in simulated petrochemical process environments containing

- hydrogen sulfide and chloride, *Mater. Sci. Eng. A407* (2005), p. 114.
92. M. P. H. Brongers, G. H. Koch and A. K. Agrawal, The use of atomic force microscopy to detect nucleation sites of stress corrosion cracking in type 304 stainless steel, *ASTM Spec. Tech. STP 1401* (2000), p. 394.
93. A. H. Qureshi, N. Hussain, J. I. Akhtar, and K. A. Shahid, Stress corrosion cracking (SCC) behaviour of low alloy steel in thiosulfateO environment, *Adv. Mater.-2001, Proc. Int. Symp., 7th, Islamabad, Pakistan, Sept. 17-21, 2001* (2001), p. 380.
94. F. Zucchi, G. Trabanelli and V. Grassi, Stress corrosion cracking of 13% Cr martensitic steels in sodium chloride solutions in the presence of thiosulphate, *Mater. Corros.* 51 (2000), p. 207.
95. R. W. Staehle, in *Proceedings of the 11th International Symposium on Environmental Degradation of Materials in Nuclear Power Systems—Water Reactors*, Vol. 1 (2003).
96. S. S. Hwang and J. S. Kim, *Corrosion (Houston)*, **58**, (2002), p. 392.
97. M. Helie, I. Lambert, and G. Santarini, in *Proceedings of the 7th International Symposim Environmental Degradation of Materials in Nuclear Power Systems— Water Reactors*, Vol. 1 (1995).

Chapter 3

Experimental Apparatus and Procedures

3.1 Materials and Solutions

3.1.1 Test materials – Alloy 800 (UNS N08800)

Alloy 800 (UNS N08800) is a widely used material of construction for equipment that should retain a high corrosion resistance, high strength and high oxidation resistance. It can also resist carburization and other harmful effects of high-temperature exposure. The high nickel content keeps the alloy ductile by maintaining an austenitic structure. The Nickel also increases the resistance to scaling, general corrosion and stress corrosion cracking. The nickel content, at around 33%, is close to the parting limit of 42% that gives unconditional immunity to de-alloying and de-alloying-related SCC [1]. The chromium content in the alloy provides further resistance to oxidation and corrosion.

Alloy 800 is used in a variety of applications involving exposure to corrosive environments and high temperatures. It is used for heat-treating equipment such as baskets, trays and fixtures. In chemical and petrochemical processing the alloy is used for heat exchangers and other piping systems in nitric acid media especially where resistance to chloride stress-corrosion cracking is required. In the production of paper pulp, digester liquid heaters are often made of alloy 800. In petroleum processing, the alloy is used for heat exchangers that cool

the process stream by air. In nuclear power plants, it is used for steam-generator tubing. The materials used in this work were received from Atomic Energy of Canada Limited (AECL), and different types of UNS N08800 have been used. Table 3.1 shows the chemical composition of alloy 800 used in this work.

Material	Al	C	Cr	Mn	S	Si	Fe
UNS N08800 (Coupon)	0.49	0.007	19.7	0.82	< 0.001	0.14	Bal. (46.32)
UNS N08800 (Small tube) Heat No: HH9043A	0.41	0.01	21.7	0.80	0.002	0.10	Bal. (42.41)
UNS N08800 (Small tube) Heat No: 516809	0.29	0.017	21.87	0.5	0.001	0.46	Bal. (43.2)
Material	Ti	Cu	P	Co	N	Ni	
UNS N08800 (Coupon)	0.57	0.30				31.52	
UNS N08800 (Small tube) Heat No: HH9043A	0.42	0.03	0.009	0.01	0.02	34.11	
UNS N08800 (Small tube) Heat No: 516809	0.48	0.02	0.12	0.1	0.016	32.78	

Table 3.1 Compositions of materials used in the experiments.

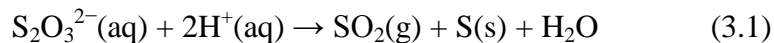
3.1.2 Solutions for S^{y-}SCC Studies

In the study of reduced sulphur effects on the SCC of steam generator tubings, different crevice solutions with sulphate and thiosulfate are used, respectively. The main components of typical crevice solutions in CANDU SG are believed to be Na₂SO₄, NaCl, KCl, CaCl₂ and SiO₂. The three solutions used to represent base crevice solutions are listed in Table 3.2. They are designated as neutral (NC), basic (BC), and acidic (AC) [4]. It would be desirable to keep the test conditions as close to Table 3.2 as possible.

Simulated Crevice Environment	Composition
Neutral (NC)	0.15 mol/kg Na ₂ SO ₄ 0.30 mol/kg NaCl 0.05 mol/kg KCl 0.15 mol/kg CaCl ₂ 0.05 mol/kg SiO ₂
Basic (BC)	NC + 0.40 mol/kg NaOH
Acidic (AC)	NC + 0.05 mol/kg NaHSO ₄

Table 3.2 Summary of the base crevice chemistries [4]

Thiosulphates are chemically stable only in neutral or alkaline solutions, but not in acidic solutions, due to its decomposition:



In this work, the effect of sulphur in the neutral condition will be investigated. Based on the above information, a test matrix for testing the degradation of SG tubing materials in reduced sulphur environments was

proposed by AECL. The solution compositions used in this work are shown in Table 3.3.

Simulated Crevice Environment	Test ID	Chemical composition	
		Base composition	Sulphur additive(s)
Neutral	NC-1	0.30 mol/kg NaCl 0.05 mol/kg KCl	0.15 mol/kg Na₂SO₄
	NC-2	0.15 mol/kg CaCl ₂ 0.05 mol/kg SiO ₂	0.075 mol/kg Na₂S₂O₃

Table 3.3 Proposed test matrix for degradation of SG tubing materials in reduced sulphur environments

3.1.3 Solutions for PbSCC Studies

The crack length determination test of SG tubing alloys was studied in the simulated CANDU[®] SG crevice chemistries listed in Table 3.4. All the results in the PbSCC work were obtained at 300°C. The test solution used included neutral CANDU SG crevice chemistries without and with the addition of 2.2 mM PbO (~500 ppm), which is the average lead level found in the sludge of most steam generators. PbO was added to the base solutions without changing the overall chloride concentration, since the chloride concentration play a very important role in high temperature corrosion.

Crevice Environment Simulated	Solution Composition (Pb free condition)	Solution Composition (Pb contaminated condition)
“Neutral” CANDU SG crevice environment	0.15 M Na ₂ SO ₄ 0.3 M NaCl 0.05 M KCl 0.15 M CaCl ₂ pH _{300°C} = 6.10; pH _{neutral} = 5.16	0.15 M Na ₂ SO ₄ 0.3 M NaCl 0.05 M KCl 0.15 M CaCl ₂ 500 mg PbO in 1L of solution pH _{300°C} = 6.88; pH _{neutral} = 5.16

Table 3.4 Simulated CANDU SG crevice chemistries with and without lead oxide.

3.2 Test Specimen Preparation

3.2.1 C-ring specimen for S^y-SCC Studies

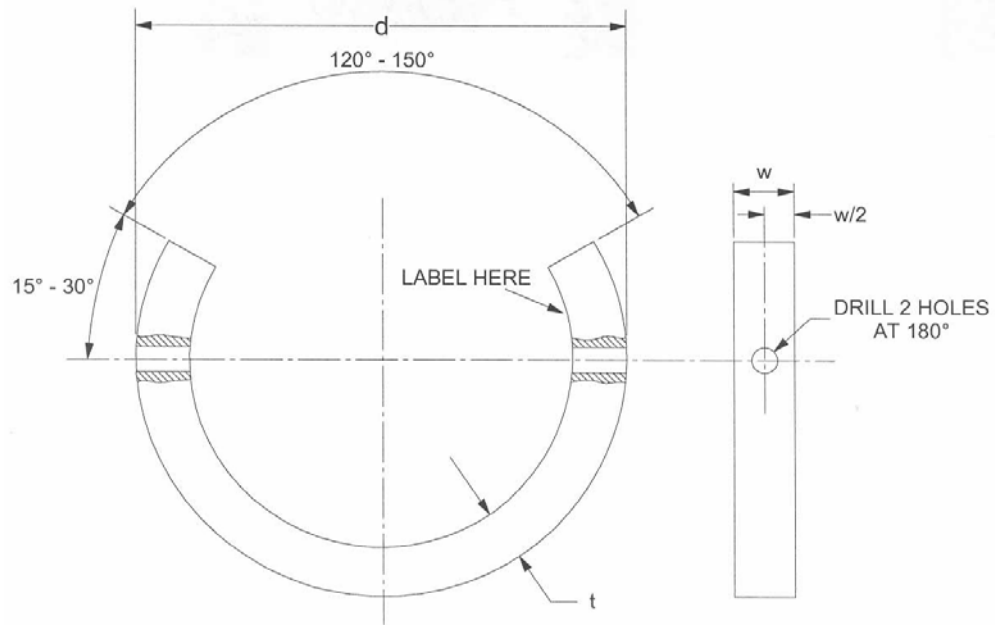
The C-ring is a versatile, economical specimen for quantitatively determining the susceptibility to stress-corrosion cracking of all types of alloys in a wide variety of product forms. To investigate the effect of stress on the S^y-SCC, a C- ring specimen was used in this work. The C-ring specimen was manufactured from alloy 800 tube according to NACE TM0177-2005 21212[5]. The tube has an outside diameter (OD) of about 15.88 mm and thickness of 1.13 mm and was cut to pieces with a length of 20 mm. After that, one third of the small pipe piece was cut away (Figure 3.1), and a bolt was inserted in the center of the specimen to

produce the desired stress. Figure 3.1 shows a scheme for a C-ring specimen from both an outlook and a side view. The bolt was coated with Teflon tape to insulate the bolt from the C-ring specimen; this may also minimize the galvanic effects during the experiments.

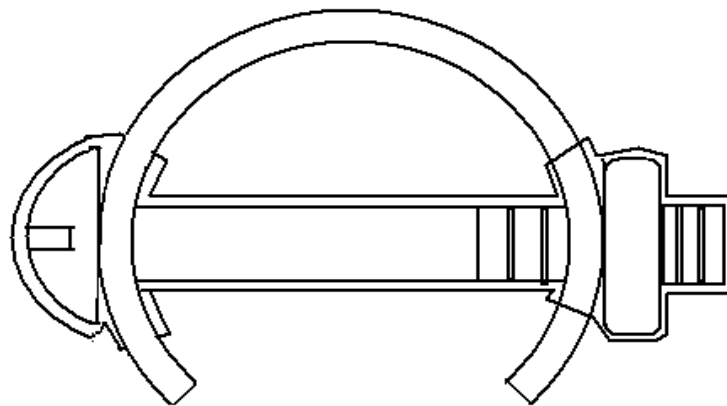
The C-ring, as generally used, is a constant-strain specimen with tensile stress produced on the exterior of the ring by tightening a bolt centered on the diameter of the ring. The desired stress can be achieved by adjusting the deflection to a necessary degree, as shown in the following equation 3.2,

$$D = \frac{\pi d(d-t)S}{4tE} \quad (3.2)$$

where D = deflection of C-ring test specimen across the bolt holes; d = C-ring test specimen outer diameter; t = C-ring test specimen thickness; S = desired outer fiber stress; and E = modulus of elasticity of the material. The two sets of C-ring specimens, one with the desired stress, and the other without stress, are connected with a copper wire and sealed in epoxy. Prior to each experiment, the surface was mechanically polished with wet silicon carbide paper (Buehler Ltd.) in the sequence of 320, 600, 800 and 1200 grit. The specimens were then rinsed with a copious amount of deionized water, and then dried in air. The specimen surface was not further treated and those specimens were used in experiments directly.



(a)



(b)

Figure 3.1 Schematic representation of C-ring specimen (a) side view [5] (b) outlook.

3.2.2 Double cantilever beam (DCB) specimen with constant opening displacement

A DCB alloy 800 specimen was used in the lead induced stress corrosion cracking (PbSCC) studies. The schematic illustration of the specimen is shown in Figure 3.2. The standard DCB test specimen design is in accordance with Figure 3.3 [5]. The precrack in the DCB specimen is initiated first by frequent loading. The DCB specimen test is a popular test to investigate crack propagation.

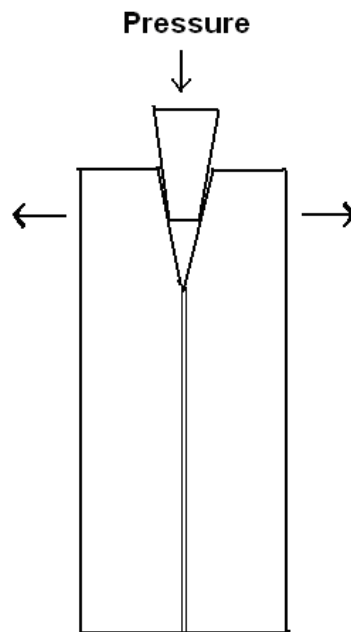
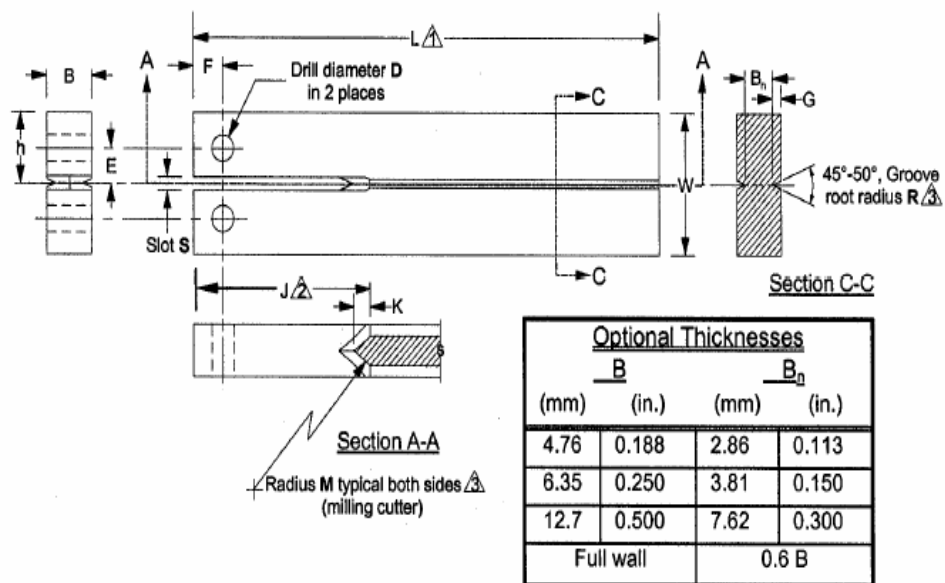


Figure 3.2 The Schematic representation of the potential drop measurement on an alloy 800 double cantilever specimen with a wedge.

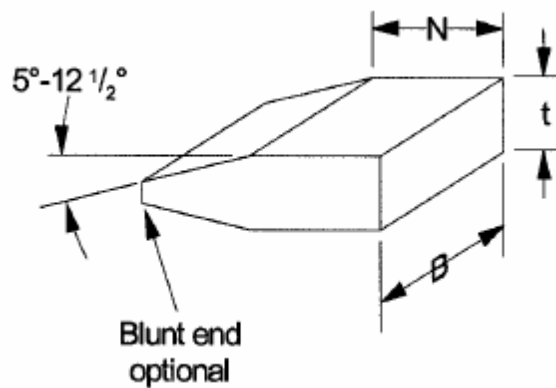


NOTES:

Dimension	Size	
	(mm)	(in.)
B	9.53 ±0.05	0.375 ±0.002
B _n	5.72 ±0.05	0.225 ±0.002
D	4.85	0.191 (No. 11 Drill)
E	6.4 +0.2/-0.0	0.25 +0.01/-0.00
F	6.35 ±0.10	0.250 ±0.004
G	1.91 ±0.05	0.075 ±0.002
h	12.70 ±0.05	0.500 ±0.002
J	38.10 ±1.59	1.500 ±0.0630
K	3.17 ±0.77	0.125 ±0.031
L	101.60 ±1.59	4.000 ±0.0630
M	51 ±13	2.0 ±0.5
N	6.35 ±0.10	0.250 ±0.004
R	0.25 ±0.05	0.010 ±0.002
S	2.38 ±0.05	0.094 ±0.002
U	130	5
W	25.40 ±0.05	1.000 ±0.002
X	0.3	0.01
Y	41.3	1.63
Z	±0.05	±0.002

Figure 3.3 The design and dimension of DCB specimen [5]

A double-tapered wedge was also used to load the DCB test specimen, and the design is shown in Figure 3.4. The double-tapered wedge is made of the same material as the DCB test specimen or of the same class of material as the DCB test specimen. The wedge material may be heat treated or cold worked to increase its hardness and thereby help prevent galling during wedge insertion. Wedges have been shielded with a 0.75 mm thick Teflon sheet to reduce corrosion in the wedge region, as well as to perform as an insulating layer to avoid short cuts during the potential drop measurement.



$$N = 6.35 \pm 0.10 \text{ mm}; B = 9.53 \pm 0.05 \text{ mm}; t = 5.14 \text{ mm}$$

Figure 3.4 The schematic representation of the double-tapered wedge

3.3 Experimental Apparatus, Setups and Procedures

3.3.1 Scratch Test

The three electrode cell was used with nitrogen flow prior to and during the measurements. The volume of the electrolyte used in the cell is about 250 mL.

The scratch test setup consists of the specimen as a working electrode, a platinum wire as the counter electrode and a saturated calomel electrode (SCE) connected with a salt bridge as the reference electrode. The reference electrode was positioned close to the working electrode in order to reduce the ohmic resistance between working and reference electrode. A schematic diagram of the scratch test system is shown in the Figure 3.5. The electrolyte was stirred magnetically, and the experiments were carried out at room temperature.

The specimen was first cleaned by milli-Q water and ethanol for 15 minutes each. Prior to the scratch test, the electrolyte was degassed using nitrogen flow for 1 hour. The specimen was passivated at -0.1 V for 15 minutes to form a passive film, and then a scratch was made across the surface of the passive film by using an alumina tip loaded on a compressed spring. The alumina tip moved an identical distance and covers the same area during each scratch. During each scratch, an Auto lab electrochemical measurement system was used to maintain a constant potential and the scratching lasts quite a short time (e.g. less than 1 ms). Damage to the passive film would result in a transient current increase, which is recorded as a function of time with an interval of 1 ms by the Auto lab system.

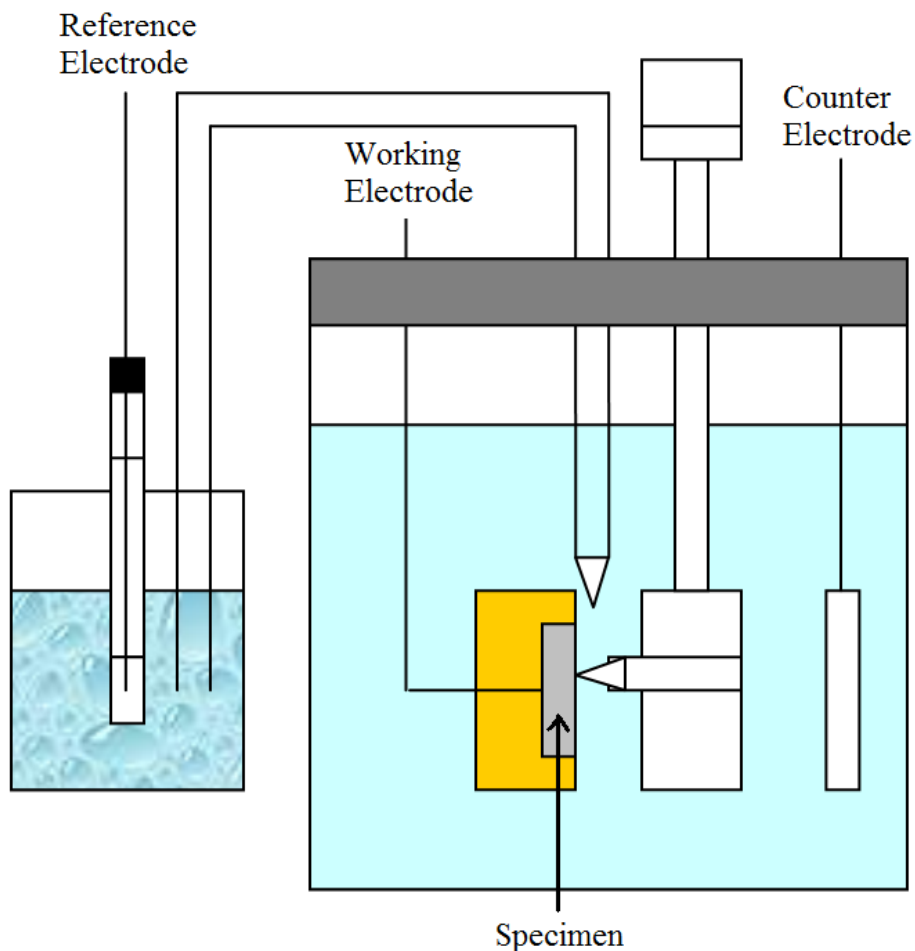


Figure 3.5 The schematic representation of the scratch test system

3.3.2 Scanning Electrochemical Microscopy Test

The structure and principles of scanning electrochemical microscopy (SECM) is discussed in section 2.9. The detailed experimental procedure is discussed in this section. The C-ring specimen preparation can be seen in Section 3.2.1.

Ultramicroelectrodes were from CHI (CHI, USA). All the tip surfaces of UMEs were also polished in succession by polishing pads coated with alumina

which have diameters of 3.0 μm , 0.3 μm , and 0.05 μm , respectively. The diamond pads sharpened the glass sheath quite well. The RG ratio, the radius of the tip insulating sheath (e.g., glass) to the radius of the central tip conductor, is 6 to 8 for 5 μm radius Pt UMEs. The polishing wheel can be spun at high speed and had minor plane vibration by using a used hard drive disk [2, 3].

All electrochemical measurements were performed on an electrochemical analyzer (CH 910B, CH Instruments), which combined a bipotentiostat and positioning system controller.

In the experiments, a potential was applied to the SECM probe to generate a steady-state current on it and the current was measured by the electrochemical system. Meanwhile, the positioning and data acquisition system were used to displace the probe and record the current and position data simultaneously. The mediator of ferrocenemethanol (Fc) was used in the redox media. The biased SECM probe was slowly moved (at a speed of 1 $\mu\text{m/s}$) to a specimen, until we could obtain a normalized negative feedback current of 0.3 when the specimen was at open circuit situation. In approach curve experiments, UME current was recorded vs. tip-to-substrate distance when the probe was moving closer to the specimen. In the constant-height imaging mode, the current was recorded as a function of lateral coordinates when the electrode was scanned in a plane at a fixed height above the substrate. In the SECM imaging, the interval is 2 μm . The tip is 5 μm in radius with RG of ~ 5 . The gap distance between tip and substrate was about 10 μm . The potential on the tip was 0.50 V. Interesting spots or small regions on images were zoomed in by relocating the tip and rescanning the

substrate in closed-loops. All experiments were carried out at ambient temperature.

3.3.3 Potential Drop Technique

The basis of the potential drop technique is measuring the electrical potential between two points by applying a steady current through the specimen, which is schematically shown in the Figure 3.6. A current of 10 A was applied between wire is B and C, by an Agilent 6642A system dc power supply (0-20V/0-10A). The potential difference between wire is A and D was simultaneously measured every one minute by an Agilent 33458A 8(1/2) digital multimeter.

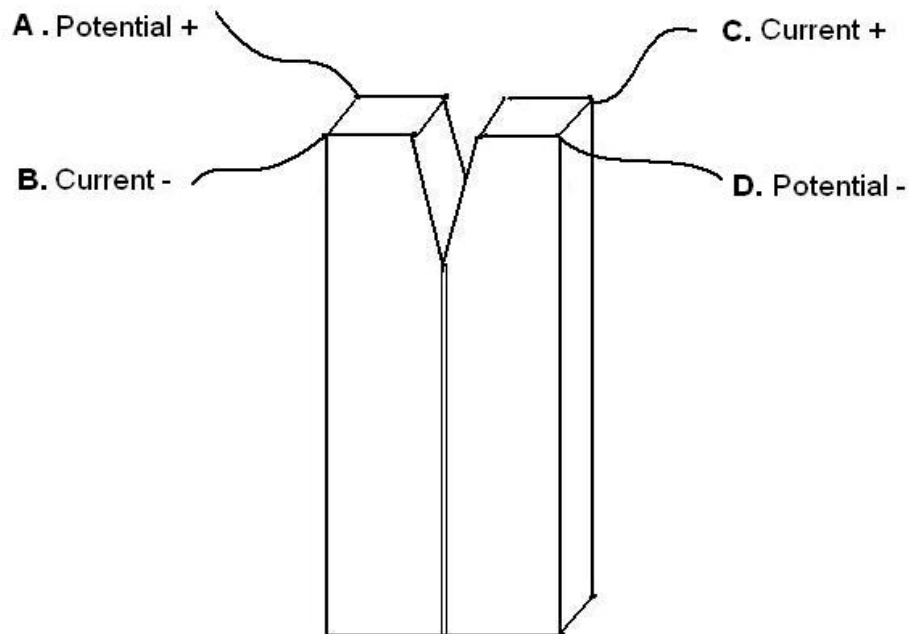


Figure 3.6 The illustration of voltage measurement and dc current going through the alloy 800 specimen

The double cantilever specimen was placed in an autoclave with a constant temperature of 300°C. Four electrical wires were connected with the specimen in the autoclave, and they are giving a constant current to the specimen as well as measuring the corresponding potential on the specimen through the potential drop system. Heat shrinkable polytetrafluoroethylene (PTFE) tube was used to seal the nickel chromium wire and the connection between the wire and alloy 800. A Teflon pad was placed at the bottom of the autoclave to insulate the specimen from the metal container inside the autoclave. Prior to the test, the electrolyte was deaerated by purging nitrogen for one hour. The autoclave was then sealed and a heater was connected with a temperature controller. The voltage values were monitored with time from the beginning of the heating.

3.3.4 Calculation of the stress intensity factor K for DCB specimen

Stress intensity factor, K , is an important parameter used in fracture mechanics to accurately predict the stress state near the crack tip. The DCB specimen is very convenient for the fracture mechanics calculation. Figure 3.7 provides a schematic representation of the specimen dimension and the load P , applied by an inserted wedge [6]. The height of each cantilever beam is H , and the thickness of the specimen is represented by B . The crack length, a , is defined as the distance between the loaded line and the crack tip. The ratio of a / H is very critical in determining the fracture toughness of materials. Many researchers have been dedicating a lot of effort to understand the fracture toughness with different

a / H ratios. According to elementary beam theory [7], the stress intensity factor is given for large values of a / H as follows,

$$K = P \left(\frac{12}{H} \right)^{1/2} \left(\frac{a}{H} \right) \quad (3.3)$$

where P is the magnitude of the loads per unit thickness.

For the cases with very small values of a / H , Irwin's solution for a semi-infinite crack in an infinite sheet can be used as an approach to obtain the stress intensity factor [8],

$$K = P \left(\frac{2}{\pi a} \right)^{1/2} \quad (3.4)$$

Later, in 1966, Gross and Srawley [9] extended the elementary beam solution to smaller values of a / H , and the expression is shown below based on boundary collocation,

$$K = P \left(\frac{12}{H} \right)^{1/2} \left[\left(\frac{a}{H} \right) + 0.687 \right] \quad (3.5)$$

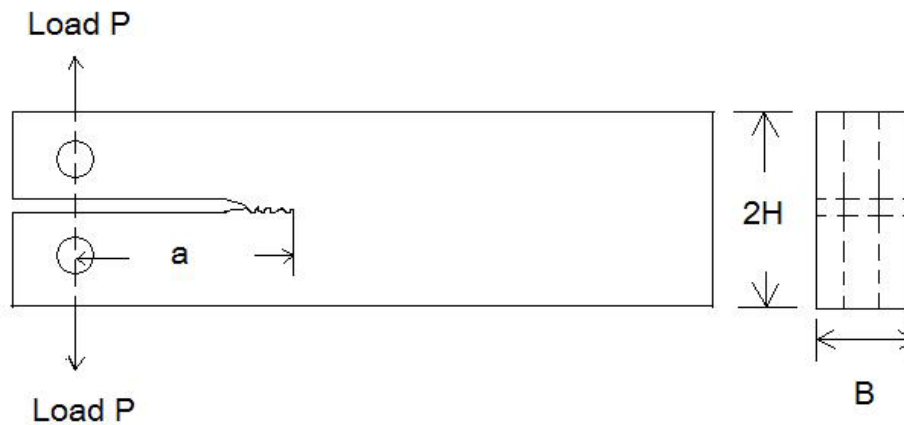


Figure 3.7 The schematic representation of the DCB specimen with a load P .

In 1985, Foote and Buchwald proposed a simple approximation formula for stress intensity factor, K , and they claimed that the values differ from the theoretical K values by less than 1.1 percent [10]. The formula is give below,

$$\frac{KH^{1/2}}{P} = \sqrt{12} \left(\frac{a}{H} + 0.673 \right) + \sqrt{\frac{2H}{\pi a}} - \left(0.815 \left(\frac{a}{H} \right)^{0.619} + 0.429 \right)^{-1} \quad (3.6)$$

This equation applied for all values of a / H , with $c / H > 2$ where c is the uncracked ligament.

Recently, the calculation of the mode I stress intensity factor, K_I , is given by Sedriks [6] as follows,

$$K_I = \frac{E \cdot V_Y \cdot H (3H(a + 0.6H)^2 + H^3)^{1/2}}{4((a + 0.6H)^3 + H^2 a)} \quad (3.7)$$

$$\text{Range of Applicability } 2 \leq \frac{a}{H} \leq 5$$

where V_Y : The crack opening displacement (COD) at loaded line.

E: Young's modulus

This equation can be used to calculate the K_I in situations where the load P is difficult to measure, so it is appropriate to use equation 3.7 in this work. For alloy 800 DCB specimen, the value $H = 12.68$ mm, $a_0 = 41.42$ mm before inserting the wedge. According to the alloy product data bulletin [11], Young's modulus, E , of alloy 800 at 400°F and 600°F is 26.81×10^6 psi, and 25.71×10^6

psi, respectively, so the E at 300°C (572°F) is 25.86×10^6 psi. In this work, $a / H = 3.3$, so it satisfies the range of applicability of equation 3.7.

References

1. Z. Coull, Proceedings. Canadian Nuclear Society, 28th Annual CNS conference & 31st CNS/CAN Student Conference June 3-6, 2007 Saint John, New Brunswick, Canada.
2. Renkang Zhu, Ph.D. Thesis, The University of Western Ontario (Canada), 2008.
3. Renkang Zhu, and et al., Chem. Mater., 2007, 19 (10), pp 2533–2543.
4. Y.C. Lu, M. Huang, D. Burns and M. Dupuis, *Electrochemical Studies on the Interactive Effect between Calcium, Copper, Aluminum, Magnesium and Lead on SG Tube Corrosion*, CANDU Owner's Group, TN-08-4067, 2008 May.
5. NACE TM0177-2005 21212, "Laboratory Testing of Metals for Resistance to Sulfide Stress Cracking and Stress Corrosion Cracking in H₂S Environments" (Houston, TX: NACE).
6. A. J. Sedriks, *Corrosion of Stainless Steels: Stress Corrosion Cracking*, John Wiley & Sons, New York, (1979), p.139.
7. J.J. Gilman, *Fracture*, Ed. B.L. Averbach et al., John Wiley and Sons, Inc., New York (1959), p. 193.
8. G.R. Irwin, *Transactions ASME, Journal of Applied Mechanics* 24 (1957), p. 361.

9. B. Gross and J.E. Srawley, "*Stress Intensity Factors by Boundary Collocation for Single-Edge Notch Specimens Subjected to Splitting Forces*", NASA TN D-3295 (1966).
10. R.M.L. Foote and V.T. Buchwald, *International Journal of Fracture*, 29 (1985) p. 125.
11. Product Data Bulletin C 800/800H, G. O. Carlson, Inc.

Chapter 4

The Study of Thiosulfate Stress Corrosion Cracking of Alloy 800 using Scratch Testing and Scanning Electrochemical Microscopy*

4.1 Results and discussion

4.1.1 Investigation of microstructures of alloy 800 specimens

Alloy 800 specimens without stress were investigated using SEM and a typical SEM image is shown as Figure 4.1a. Some darker spots were clearly found on the image. The compositions of these spots and bulk surface (area other than the dark spots) were investigated using EDX and the results are shown in Figure 4.1b. These inclusions mainly contain either Ti (Spot 1) or Si (Spot 3). The relative concentrations of Ti or Si are normally much higher than those in the bulk surface. Therefore, the surface composition of alloy 800 specimens is not uniform.

* A version of this chapter has been submitted for publication to Corrosion Science with a Ref. No.: CORSCI-D-10-00939.

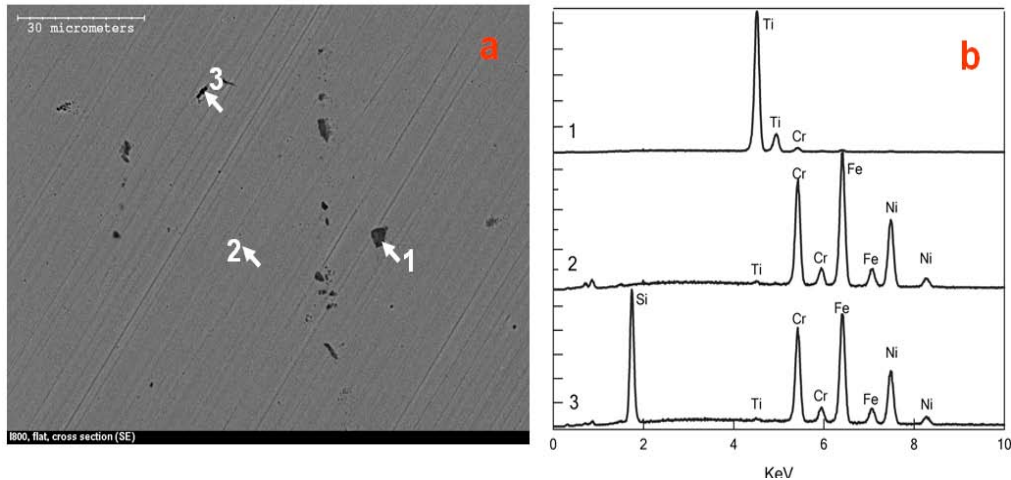


Figure 4.1 SEM image (a) and EDX results (b) of alloy 800

In order to observe the microstructure transformation under applied stress, two sets of specimens (one with stress and the other without stress) were well-polished and etched in the solution. The optical micrographs are shown in Figure 4.2. Images 4.2a and 4.2b were observed on the specimen without stress. The grain boundaries and inclusions are seen very clearly. The grain size and grain shape were quite different. At the same etching condition, the optical images taken from the specimen (Images 4.2c and 4.2d) with stress were quite different from Images 4.2a and 4.2b. Some grain boundaries on the stressed specimen were wider than others on the same images. These wider than average boundaries were considered to be activated by the applied stress. This phenomenon was also seen around some inclusions, such as the part at the lower left corner on Image 4.2c. These observations are very similar with what was reported in reference [26]. For

the C-ring specimen, the tensile stress reaches a maximum at the apex of the C-ring, decreasing to zero at the bolt holes [42]. Hence, the activated grain boundary

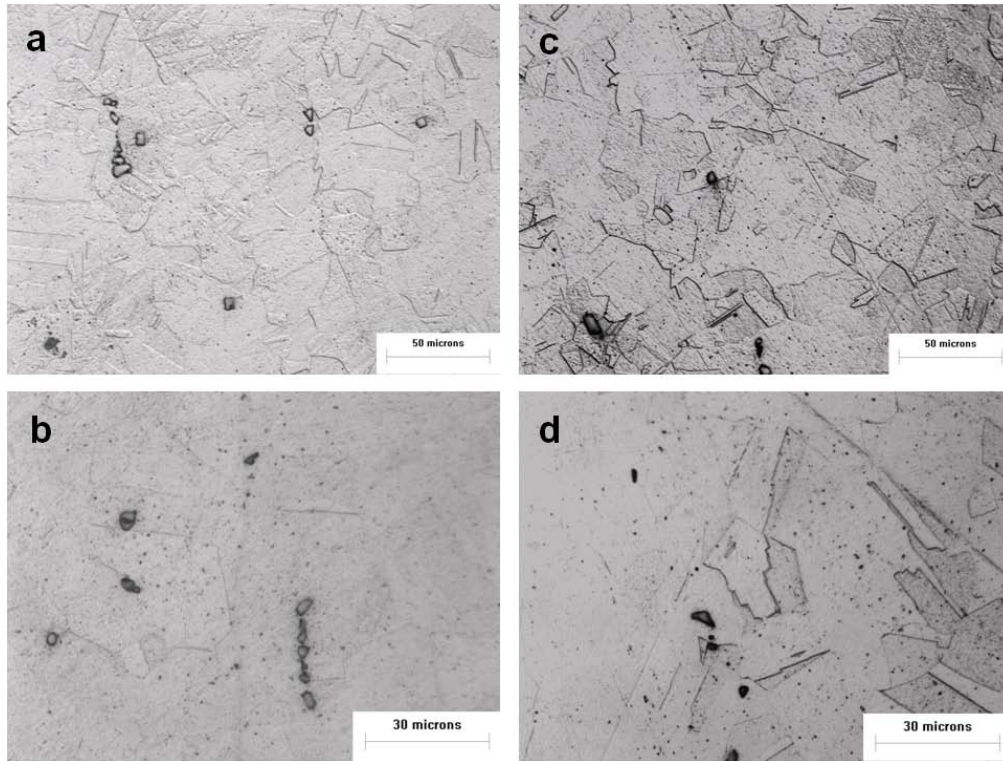


Figure 4.2 Microstructures of alloy 800 without (a and b) and with stress (c and d).

density should be the highest at the apex of the C-ring and lowest at the edge of the C-ring gap. This kind of phenomena was observed in our experiments. The activated grain boundaries were found in the area close to the apex of the C-ring and less or no activated grain boundaries were observed at the two edges. Due to the high stress applied on the C-ring specimen, tension has been accumulated at grain boundaries, which increases the local reaction rate and, therefore, the tension effect on grain boundaries were observed clearly on etched sample surfaces.

4.1.2 Effects of stress and thiosulfate on the pitting potential of alloy 800 specimen

Figure 4.3 shows the typical polarization behaviour of unstressed alloy 800 in neutral crevice NC1 (SO_4^{2-} , a, solid-line) and NC2 ($\text{S}_2\text{O}_3^{2-}$, b, dash-line), and the stressed specimens in NC2 (c, dot-line). The corrosion potentials, passive current densities and pitting potentials are summarized in Table 4.1 for comparison. $\text{S}_2\text{O}_3^{2-}$ discretely changes the corrosion potential, pitting potential and passive current density. Due to the strong interaction of $\text{S}_2\text{O}_3^{2-}$ with Fe, Ni, Cr, etc., in alloy 800, the corrosion potential in the $\text{S}_2\text{O}_3^{2-}$ solution was anodically shifted 269 mV in comparison with the one in NC1. However, the pitting potential in NC2 was cathodically shifted 538 mV and the passive current increased 2.7 fold, also implying the strong $\text{S}_2\text{O}_3^{2-}$ effects on corrosion behaviour of alloy 800. This result indicates that $\text{S}_2\text{O}_3^{2-}$ clearly degrades the oxide film. A similar phenomenon was also found in saturated ammonium chloride solution with $\text{S}_2\text{O}_3^{2-}$ [18].

Curve	Solution	Stress (MPa)	Corrosion potential (mV)	Passive current density ($\mu\text{A}/\text{cm}^2$)	Pitting potential (mV)
a	NC1	No	-281	2.78	846
b	NC2	No	-12	10.3	308
c	NC2	450	-651	90.8	223

Table 4.1 Corrosion potentials, passive current density and pitting potentials obtained on the polarization curves in Figure 4.3.

When stress was applied on the alloy 800 specimen, the corrosion potential was cathodically shifted 639 mV, the pitting potential was also cathodically shifted, in this case 85 mV,

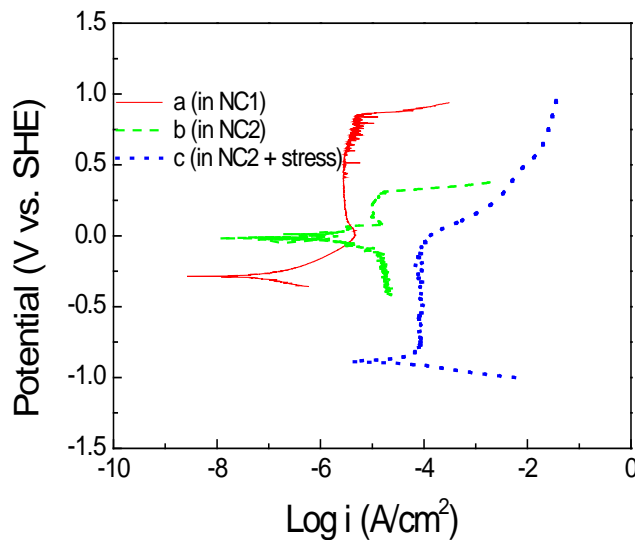


Figure 4.3 Polarization curves of Alloy 800 in neutral crevice chemistries. (a): unstressed specimen in sulphate solution (NC1), (b): unstressed specimen in thiosulfate solution (NC2), and stressed specimen in thiosulfate solution (NC2). i is the current density (A/cm^2).

and the passive current increased almost 9 fold, compared to the corresponding parameters obtained from the unstressed specimens. At this applied stress, the nucleation of cracks might have formed and enhanced the interaction between the alloy surface and $S_2O_3^{2-}$, resulting in a significant increase in the passive current density. Also, due to the nucleation of cracks, the corrosion potential of such areas was shifted more negatively and the pitting potential decreased. Stress reduced the corrosion resistance of alloy 800 in a $S_2O_3^{2-}$ environment. Stress possibly

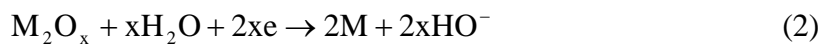
activated the grain boundaries, particularly at grain boundary triple points and grain boundary/twin boundary intersections [26]. These could result in the high passive current density observed on the cyclic polarization curves on stressed specimens. The cathodic shift of corrosion potential is possibly due to the highly negative starting potential applied on the surface and cause Reaction 1 to occur on the specimen meaning the surface is covered with a sulfide layer instead of an oxide layer.



Figure 4.4a shows the current transient plots for alloy 800 specimen without stress in NC1 at different potentials (-0.7, -0.2 and 0.0 V). Before the scratch, the background current was quite low, and approached a stable value, $1.0 \mu\text{A}/\text{cm}^2$, which was very stable in the potential range between -0.7 V and 0.0 V. The current increased dramatically during the scratch, due to the exposure of a bare metallic surface without oxide film in the solution. The fresh surface reacted with water quickly. After the scratch stopped, the current reached a maximum value and then started to decrease with time and return to a stable value. Burstein et al. reported that the anodic current measured during repassivation was consumed mainly for the formation of a passive film on the scratched surface when the metal dissolution was not dominated by pitting or general corrosion [46-48]. From -0.7 V to 0.0 V, the current after a scratch decreased to values which were close to the value before the scratch, indicating that the passive film was reformed on the scratched surface. Even at 0.1 V, the current density after

repassivation remained at $10 \mu\text{A}/\text{cm}^2$, which indicates that pitting did not occur due to weak attack of the ions in NC1 on this material. In this solution, pitting occurred when the potential on alloy 800 was over 0.846 V (Table 4.2).

Figure 4.4b shows a comparison of the peak currents for the specimen without stress at different potentials in NC1. The peak currents increased from 50 μA at -0.7 V to 770 μA at 0.1 V. When quite a negative potential was applied to the alloy 800, the oxide film was partially reduced (Reaction 2), and as a result, the oxide film on the alloy 800 was very thin. Water was expected to be reduced on the surface through Reaction 3 (hydrogen evolution). As long as the naked metallic surface was exposed in the solution and the material was biased at a very negative potential, the hydrogen evolution reaction would take place with a significant high rate and contribute to the cathodic current, therefore affecting the measured current density peak. At the applied potential, the surface still could form a layer of oxide film on the new exposed metallic surface, but the contribution from this reaction relevant to film formation was small, and therefore, the maximum current that appeared at an applied potential less than -0.4 V was quite low. When the applied potential increased, Reaction 3 was depressed, but the oxidation reactions of metal increased dramatically and the anodic dissolution of metallic elements from alloy 800 specimen into solution also occurred through Reactions 4 and 5. The maximum current was mainly contributed from Reaction 4.



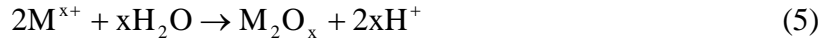


Figure 4.5 shows the current transient plots of the alloy 800 specimen with stress in NC1 at different potentials. The initial current density observed on the specimens before a scratch ranged between 1 and 4 $\mu\text{A}/\text{cm}^2$, which was very close to the values observed on unstressed specimens (Figure 4.4). However, when the potential on

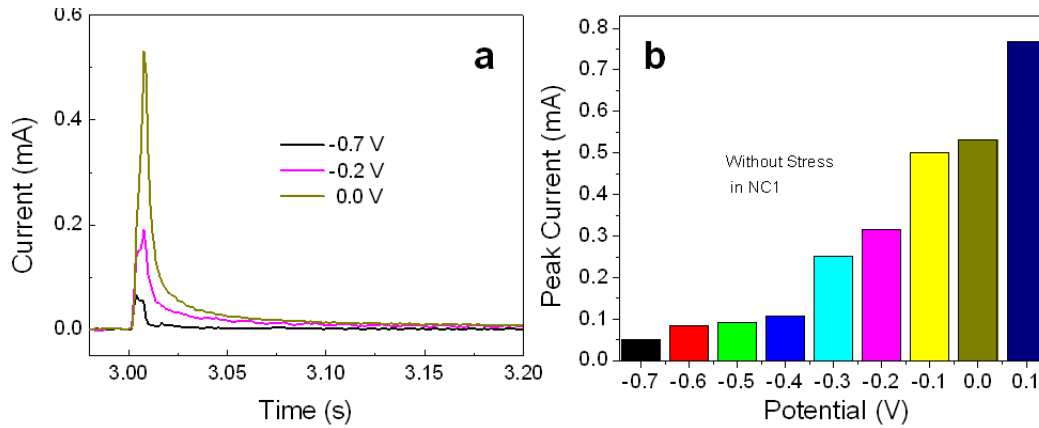


Figure 4.4 Comparison of scratch testing results at different potentials on unstressed Alloy 800 C-ring specimens in simulated NC1. (a) Current plots of potentiostat processes; (b) Peak current at different potentials.

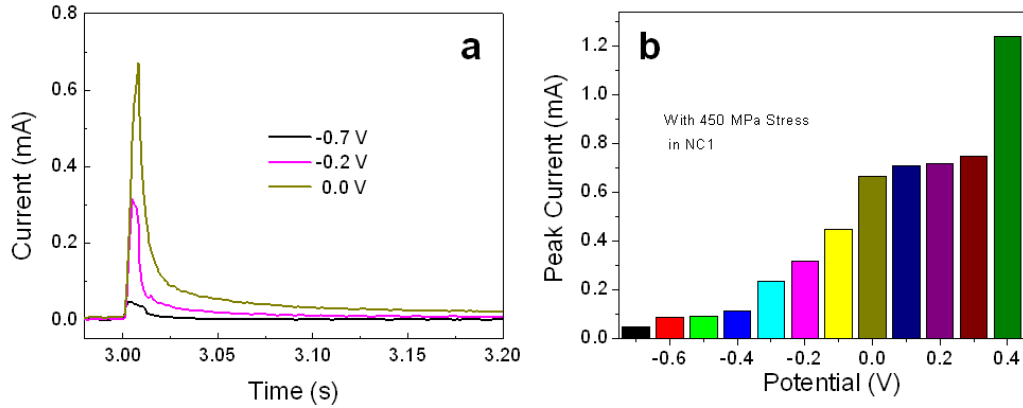


Figure 4.5 Comparison of scratch testing results at different potentials on stressed Alloy 800 C-ring specimens in simulated NC1. (a) Current plots of potentiostat processes; (b) Peak current at different potentials

the stressed specimen was shifted anodically, the initial current density increased, indicating that the stress activated the specimen surface. After a scratch broke the passive film at potentials between -0.7 V to 0.3 V, the anodic current from the scratch surface increased dramatically to a maximum due to an anodic oxidation reaction and decreased as repassivation proceeded thereafter. When the potential was increased to 0.4 V, an anodic current jump was observed right after the scratch peak current, but repassivation still dominated afterwards. No pitting or serious general corrosion was observed in NC1 in both stress and non-stress conditions. The sulphate anion did not accelerate the susceptibility of stress corrosion cracking of Alloy 800 under the neutral crevice conditions, which is consistent with the Staehle's statement that the sulphates (+6) and sulphite (+4), do not affect either hydrogen entry or general corrosion [1].

Figure 4.6a shows the current transient plots for an alloy 800 specimen without stress in NC2 at different potentials. The initial current observed on specimens before a scratch ranged from 2 to 70 $\mu\text{A}/\text{cm}^2$, which was significantly higher than the values observed in NC1, indicating the strong interaction of $\text{S}_2\text{O}_3^{2-}$ with the oxide film on alloy 800. The more positive the potential bias on alloy 800, the higher the initial current was. At -0.7 V and -0.1 V, the complete reformation of the passive film indicated that no pitting behaviour was observed in this potential range. With an increase of potential to 0 V, the anodic current stayed around 70 $\mu\text{A}/\text{cm}^2$ and increased slowly with time. Pitting behaviour was observed at this potential. The pitting behaviours became more severe when the potential was increased to 0.2 V and 0.3 V, and the anodic current kept increasing after the specimen surface was scratched, even though the potential was constant. Figure 4.6b shows the maximum peak current during the scratch in NC2. The current increase tendency was quite different in NC1, implying that the $\text{S}_2\text{O}_3^{2-}$ effects on repassivation were quite different from that of either sulphate or chloride.

The current transient plots for alloy 800 specimen with applied stress in NC2 at different potentials is shown in Figure 4.7a. The initial current before a scratch ranged from 4 to 120 $\mu\text{A}/\text{cm}^2$. These values were much higher than those observed on either the unstressed specimens in NC2 or the stressed specimens in NC1. The synergistic effect of $\text{S}_2\text{O}_3^{2-}$ and stress was clearly observed. It was seen that the passive films were reformed at potential -0.7 V and -0.1 V, and pitting occurred at 0 V. Figure 4.7b indicates that the anodic peak current increased with

the potential increase, and the anodic peak current changed from about 0.7 mA/cm² at -0.1 V to 1.15 mA/cm² at 0 V. At a potential over 0.0 V, pitting behaviour was observed. It indicates that the stress did increase the anodic current dramatically in the scratch process for the same environmental conditions. The applied stress increased the surface reactivity, which agrees well with what was observed in cyclic polarization experiments.

Figure 4.8a summarizes the current transient peak current during the scratch test at different potentials for 4 different conditions. The peak currents (the columns with left-tilted lines and right-tilted lines in Figure 4.8a) in NC1 increased slowly with a potential lower than -0.4 V and the increase became relatively fast until the potential reached -0.1 V. The quite similar trend of peak current changes indicates that the effect of stress level did not make a significant difference in NC1. However, it was observed that the stress dramatically increased the slope of peak current vs. potential in NC2. It indicates that the stress increased the anodic dissolution of passive film on the alloy 800 surface.

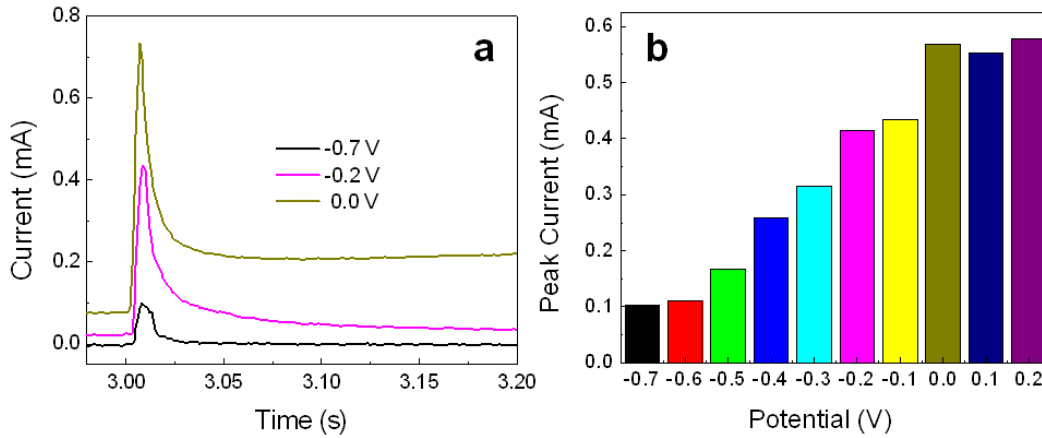


Figure 4.6 Comparison of scratch testing results at different potentials on unstrained alloy 800 C-ring specimens in simulated NC2. (a) Current plots of potentiostat processes; (b) Peak current at different potentials.

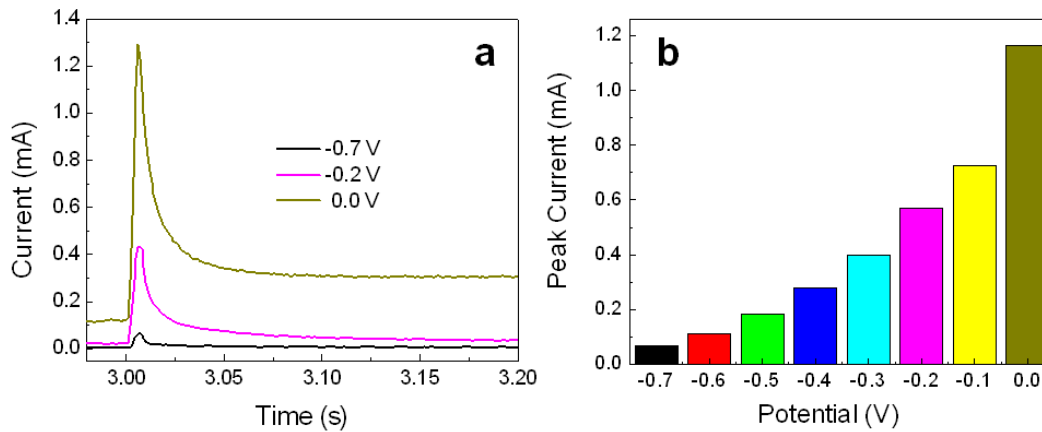
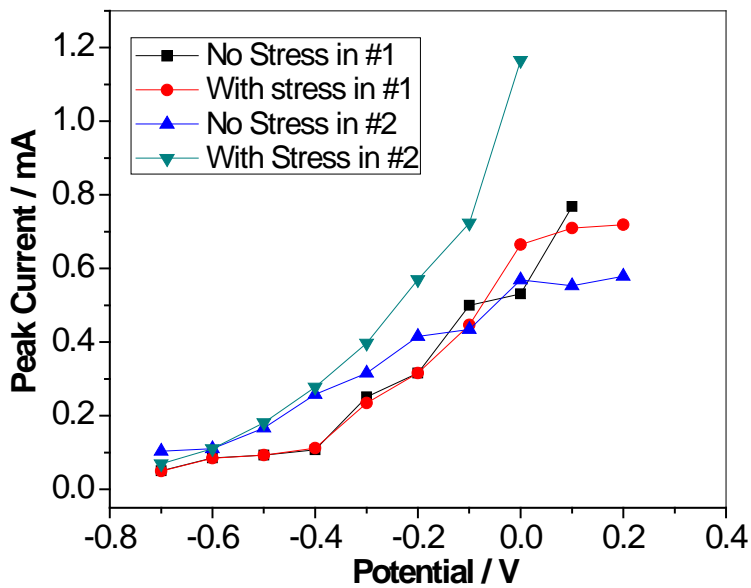
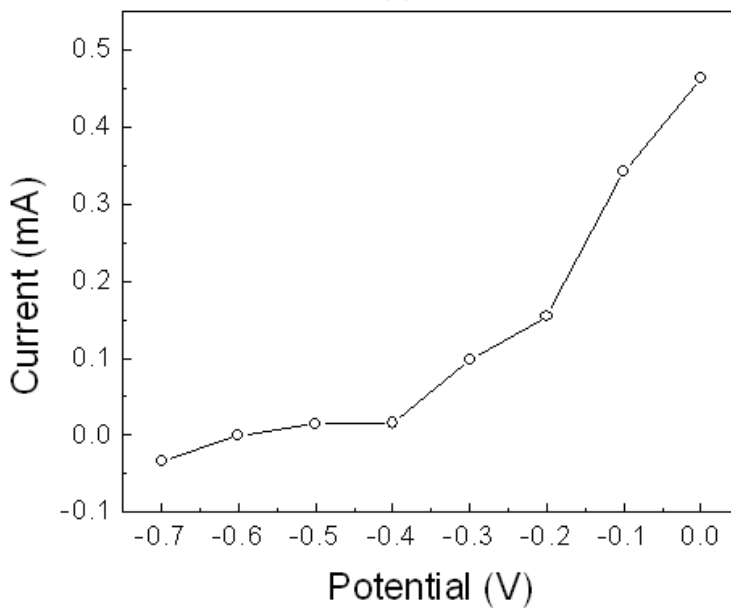


Figure 4.7 Comparison of scratch testing results at different potentials on stressed alloy 800 C-ring specimens in simulated NC2. (a) Current plots of potentiostat processes; (b) Peak current density at different potentials.



(a)



(b)

Figure 4.8 Comparison of peak currents of scratch tests at different potentials in both NC1 and NC2 with and unstressed Alloy 800 C-ring specimens. (a): the peak current in four conditions; and (b): the synergistic effect of thiosulfate and stress on the peak current.

in the presence of $S_2O_3^{2-}$. Thiosulfate could induce pitting, IGA and SCC, which have been intensively studied in the references on various materials [4, 7, 13-15, 22, 25, 49, 50]. When the applied potential was more negative than -0.2 V, the peak currents in NC2 were higher than the values observed in NC1. This was possibly due to the fact that $S_2O_3^{2-}$ enhances the anodic dissolution of alloying elements into the solution. However, when the potential shifts to a more positive value, the surface covers with oxide and as a result, this interaction is suppressed. Also, due to the stronger interaction of $S_2O_3^{2-}$ with oxide film of alloy 800, namely strong chemical absorption of $S_2O_3^{2-}$ on the surface, the maximum peak current decreased. $S_2O_3^{2-}$ could also be involved in the corrosion process as an oxidant, which would reduce to sulphide or sulphur (Reactions 6, 7 and 1). The SEM/EDX results proved that the sulphur/sulfide did exist in the corrosion products in our experiments, which was also reported in the literature [6, 23, 28, 29]. These show the evidence of $S_2O_3^{2-}$ reduction reaction happening during the process.



The synergistic effects of $S_2O_3^{2-}$ and stress were investigated in our experiments, as shown in Figure 4.8b. The current density in Figure 4.8b was obtained by Equation 8:

$$i_{synergy} = (i_{thio+stress} - i_{background}) - (i_{thio} - i_{background}) - (i_{stress} - i_{background}) \quad (8)$$

where, $i_{synergy}$ means the net current density caused by the synergistic effect of

$S_2O_3^{2-}$ and stress; the first bracket is the total current density increase due to $S_2O_3^{2-}$ and stress against the value in sulphate solution, the second bracket is the current density increase due to $S_2O_3^{2-}$ against the value in sulphate solution, and the third bracket is the current density increase due to stress against the value in sulphate solution. For potentials below -0.4 V, the synergistic effect was not very obvious. However, when the potential was higher than -0.3 V, the synergistic effect of $S_2O_3^{2-}$ and stress was clearly observed. With an increase in the potentials, the corrosion of alloy 800 increases significantly and the synergistic effect between stress and the effect of $S_2O_3^{2-}$ became more evident.

After a scratch, the freshly exposed metallic surface can be repassivated and the current decreases to a stable value or to a low value, and then increases again when pitting occurs on the surface. The repassivation time can be defined by the difference between the time when a maximum peak current was reached and the time when a stable or the lowest current was reached. The repassivation times observed in the above experiments are listed in Table 4.2. It is clearly seen that the repassivation time in NC1 solution increased with the applied potential increasing. When a stress was applied on the specimen, the repassivation time showed the same tendency of change as the applied potential did, but it was longer than that for an unstressed specimen at the same potential. Stress could significantly retard the repassivation process of this material.

Solution	Stress	Potential (V)				
		-0.7	-0.6	-0.2	-0.1	0.0
NC1	No	76	92	125	149	146
	Yes	95	106	176	200	265
NC2	No	69	134	260	264	70
	Yes	84	153	330	356	121

Table 1.2 Summary of repassivation time (unit: ms) in scratch test

In NC2, the repassivation time still had the same tendency with potential as that in NC1. Comparing the data in NC2 to NC1, it was concluded that $S_2O_3^{2-}$ delayed the material repassivation. The synergistic effect on repassivation time was not clear, but repassivation times for the stressed specimen in the NC2 were longer than those obtained on all other three conditions at the same potential except at -0.7 V and 0.0 V. However, because alloy 800 had pitting at 0.0 V in NC2, the repassivation time for a fresh surface could be regarded as infinite. The values listed in Table 1.2 are the time when the current reached a minimum value during the whole recorded processes. The current observed on specimen without stress in NC2 was stable from 70 ms to 350 ms and then increased slowly with time (Figure 4.9), indicating the periods of pitting initiation and propagation. For a stressed sample in the NC2 at 0.0 V, the current density on the specimen reached a minimum value and then slowly increased immediately. The pitting initiation period was very short in this case. The detrimental effect of $S_2O_3^{2-}$ and stress enhancing pitting of alloy 800 was clearly observed.

Figure 4.9 shows the current vs. time plot measure during scratch tests at a potential of 0.0 V. As mentioned above, the current decrease was due to the

repassivation on the fresh surface formed by a scratch. If there was no pitting, the current should return to or close to its original value before the scratch, as curves a and b demonstrate in Figure 4.9. However, when pitting occurred in NC2, the minimum current after the scratch on an unstressed specimen was much higher than that before the scratch, and the minimum current value was 0.07 mA/cm^2 , which was over 3 fold higher than that obtained on specimens with or without stress in NC1. For stressed specimens in NC2, the minimum current density after the scratch was 0.19 mA/cm^2 , which was over 2.5 times higher more than that obtained on the unstressed specimens in the same solution. This indicates a synergistic effect between thiosulfate and stress on pitting.

Figures 4.10a and 4.10b show SEM images of the scratch surface morphologies of Alloy 800 at -0.1 V in the NC2 without and with stress, respectively. There was no pitting observed on the scratched surface at -0.1 V for both conditions. However, when the potential increased to 0 V under the same conditions, pits were observed, as shown in Figure 4.10c and 4.10d. The diameters of the pits ranged from $10 \text{ }\mu\text{m}$ to $50 \text{ }\mu\text{m}$, and smaller pits were also observed at the bottom of some large pits. The pits in the stressed specimens were larger and with more population than that in the unstressed specimens, indicating that the stress also increased the pit area and density. The synergistic effect between stress and $\text{S}_2\text{O}_3^{2-}$ on pitting corrosion of alloy 800 was again demonstrated clearly by the SEM images.

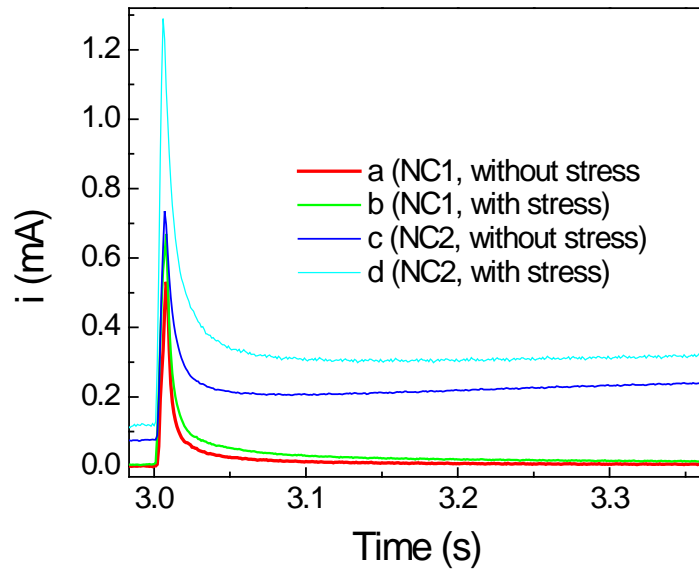


Figure 4.9 Comparison of the current at 0.0 V after a scratch under four conditions: the specimens (a) without stress and (b) with stress in NC1, the specimens (c) without stress and (d) with stress in NC2;

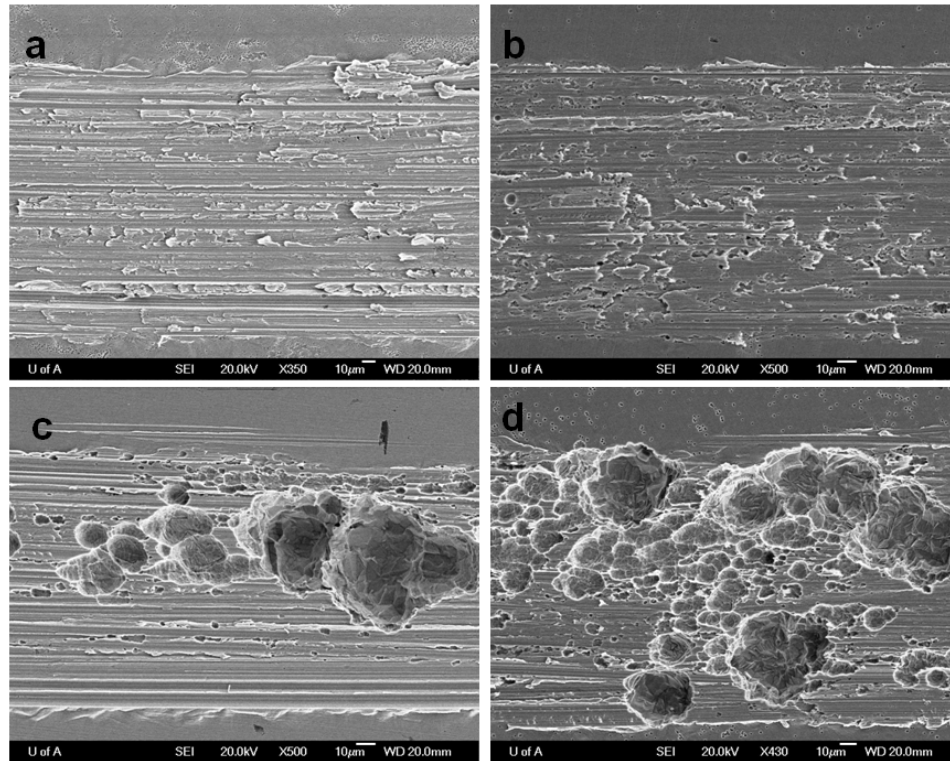


Figure 4.10 Comparison of SEM images of scratched surface morphologies under different conditions in NC2.

- (a): -0.1 V on unstressed specimens;
- (b): -0.1 V on stressed specimens;
- (c): 0 V on unstressed specimens; and
- (d): 0 V on stressed specimens.

4.1.3 Localized corrosion effects of thiosulfate and stress

Due to its outstanding advantages, SECM was employed to study the localized reactivity on stressed and unstressed alloy 800 specimens in the NC1

with Fc and the NC2 with Fc. Fc is intensively used in the experiments as a redox medium [45]. It can oxidize to ferroceniummethanol (Fc^+) as described by Reaction 9.



Figure 4.11a shows the SECM image obtained on an alloy 800 specimen without stress in NC1 with 0.9 mM Fc. The gap distances between tip and substrate are about 8 μm for Image a, 9 for Image b, and 5 for Image c. The labeled regions are for PAC experiments in Figure 4.12. Scan range is 200 μm by 200 μm , and the scan rate is about 120 $\mu\text{m}/\text{s}$. Several spots (blue color) with higher current than their surroundings were clearly seen, where the reverse reaction of Reaction 9 happened more quickly. These active spots were possibly due to inclusions, triple points or grain boundaries which cause a slightly thinner oxide film on the localized region or higher conductivity. Zhu et al. studied the localized surface conductivity/reactivity on Ti alloys and concluded that the reactivity difference on the Ti alloy surface is caused by the triple points, grain boundaries or inclusions [35, 51]. Nowierski correlated the SECM images with SEM images and found that the reactive regions were related to the grain boundaries [52]. In the material used in our experiments, the inclusions with high contents of Si or Ti were found easily on SEM images and the content of Ti or Si was higher than 90 atom% according to EDX analysis results (Figure 4.1b). However, the reactivity difference between inclusions and bulk region were quite small at this applied potential (0.1 V),

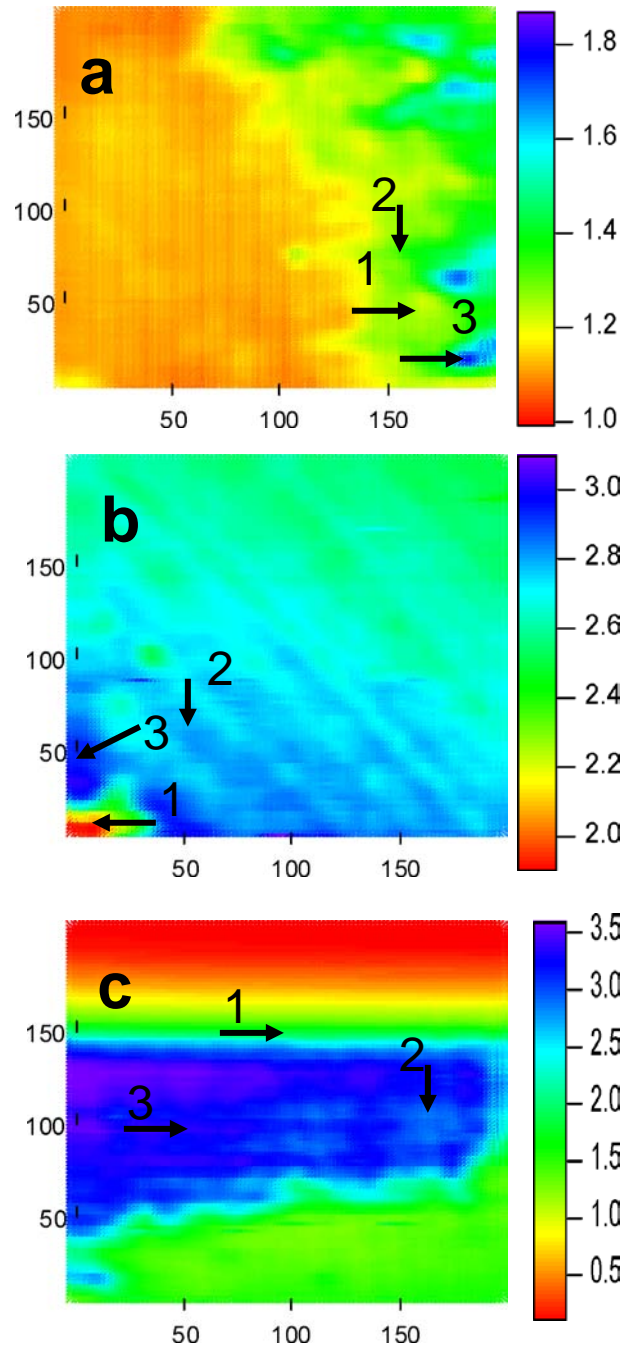


Figure 4.11 SECM images of Alloy 800 specimens. (a): without stress in NC1 with ferrocenemethanol (Fc), (b): without stress in NC2 with Fc, and (c): with stress in NC2 with Fc. Potential on tip: 0.50 V; and potential on specimen: 0.10 V. Tip had 5 μm in radius with RG of 5.

comparing Curves 1 (square) in Figure 4.12a and 4.12b which will be discussed later. Figure 4.11b shows the image obtained on an alloy 800 specimen without stress in the NC2. The active spots are not as clear as those in Figure 4.11a. However, the average current was obviously higher than that in Figure 4.11a, which indicated a higher reactivity/conductivity on the surface in NC2. This result agreed well to the potential polarization and scratch testing results. When a stress was applied on the alloy 800 specimens, the current pattern of the SECM image shown in Figure 4.11c was totally different from Figure 4.11a or 4.11b. A belt zone with higher current appeared on the image which was vertical to the stress direction. The current in this region was much higher than other regions, which agrees well with the results in Figure 4.3, and also with the conclusions from optical observations of etched specimens with stress (Figure 4.2). With the stress applied on a C-ring specimen, the tensile stress reaches a maximum at the apex of the C-ring [42]. The stress gradually decreases from the apex to the two bolt holes. It is expected that the highest reactivity region appears at the apex of the C-ring and the direction of the higher reactivity belt is vertical to the stress direction. All these have been observed in our SECM experiments.

In order to verify that the current difference in different regions is caused by the different surface reactivity instead of topography, two regions, one on an active region (labelled 3 in Figure 4.11) and another on a bulk region (labelled 1 in Figure 4.11) with lower current on SECM images, were selected for PAC experiments. The results are shown in Figure 4.12. Figure 4.12 show 3 PACs of bulk regions on the alloy 800 specimens without stress in NC1 (Curve 1, square)

and NC2 (Curve 2, circle) with Fc and specimens with stress in NC2 (Curve 3, triangle) with Fc. It is clear that the specimen in a $S_2O_3^{2-}$ solution was more reactive at the applied potential (0.1 V) which agreed well to the results from Figure 4.3, and the passive current in NC1 was lower than it in NC2. When a stress was applied on the specimen (Curve 3, triangle), the surface reactivity on the bulk was only a little higher than that on the specimen without stress. In this region, stress possibly did not seriously affect the surface film. Sun et al. investigated a similar phenomenon on Type 316 SS using $Ru(NH_3)_6^{3+/2+}$ redox couple and found that the oxidation rate decreased with increasing stress [53]. However, a higher stress was applied on our specimens, which is close to the ultimate tensile stress of alloy 800 (450-500 MPa [43]), while the tensile stress Sun et al. applied to Type 316 SS was much lower than its yield stress. Since the stress effect normally focuses on very small structures, such as grain boundaries, inclusions and/or triple points, a small probe (radius: 5 μm) was used in our experiments to improve the spatial resolution so that the localized surface ET enhanced by an applied stress was successfully measured.

Figure 4.12b shows 3 PACs obtained above the distinguishable active spots on unstressed alloy 800 specimens in NC1 (Curve 1, square) and NC2 (Curve 2, circle) with Fc and a stressed specimen in NC2 with Fc (Curve 3, triangle). The effect of $S_2O_3^{2-}$ in enhancing the surface reactivity was very clearly shown. After the stress was applied on the specimen, the reactivity on the active region was much higher than other regions (triangle curve in Figure 4.12a and 4.12b). The reactivity of the active regions on the stressed specimen was much

higher than that on the unstressed specimen, indicating that the stress significantly increased the localized reactivity. The higher reactivity on the stressed specimen indicated that crack nucleation formed on the surface. This conclusion is consistent with the results from observation of optical micrographs. It was reported

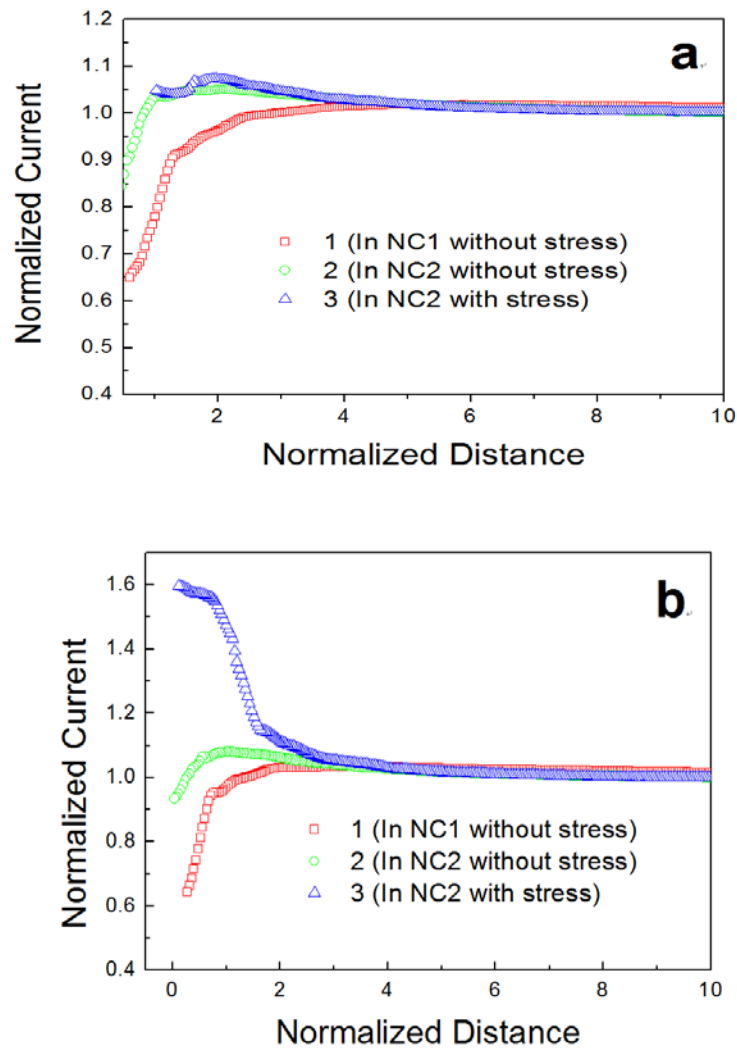


Figure 4.12 PACs at different reactive regions on Alloy 800 specimens. (a): non reactive region; and (b): reactive region. Potential on tip: 0.50 V; and potential on specimen: 0.10 V. Tip had 5 μm in radius with RG of 5. Quiet time was 30 s; approach speed was 1 $\mu\text{m}/\text{s}$.

that upon plastic deformation of the annealed and sensitized SS304, the AFM results reveal that slip lines piled up at the grain boundaries which increases localized stresses; some of the grain boundaries open, particularly at grain boundary triple points and grain boundary/twin boundary intersections [26]. Dinu et al claimed that alloy 800 C-ring specimens showed about 5 μm deep cracks on the stressed surface when the C-ring deflected for an approximately 390 MPa stress ($\Delta=0.6$ mm) and 15 μm deep cracks on the ones with about 490 MPa ($\Delta=6.6$ mm) stress [43]. These research results support our conclusions.

4.1.4 Semi-quantitative results of localized reactivity

The PACs toward the different regions on alloy 800 specimens with or without stress were simulated using COMSOL in order to obtain the localized electron transfer rate which is a significant parameter related to the localized reactivity at the different positions. The principle is well described elsewhere [37, 51], and the model used in our simulation is briefly described here. The 5 μm -radius UMEs with RG of about 5 were used as a SECM probe and also in the simulations. Alloy 800 specimens were used as the substrate. The size of active spots found on the substrate was estimated in SECM images and used in the numerical simulations. A cylindrical coordinate was used in the simulation. It was assumed that the center of the active spot was at the symmetric axis and there were no other active spots around it. The tip geometry was adjusted to be very similar to the true probe shape (corn-shape) used in our experiments.

As an example for comparison, the experimental data with simulated data are plotted in Figure 4.13. The PACs obtained on the three different regions with different activities were plotted here (the circle for the non-active region, the diamond for the active region and the star for the region between these two limits). The simulation data overlapped with the experimental data very well in all three cases. Due to the fact that the surface was a metallic alloy with a thin layer of oxide film, all three cases are more active than the insulator (bottom solid line) and less active than the conductor surface (top dotted line). The reactivity was quite different on different regions on alloy 800 which were seen from the simulated data. For the non-active region, the apparent rate constant was about 0.00062 cm/s, and it was about 0.053 cm/s for the active region, which is 85 times higher than in the non-active region. For the region between these two limiting cases, the apparent rate constant was about 0.0023, which is almost 3.7 fold higher than for the non-active region.

While different potentials biased on alloy 800, the data of PACs to the different active regions has been simulated and the simulation results are plotted in Figure 4.14. Figure 4.14a shows the simulation results obtained on the non-active region on alloy 800 specimens in NC1 without stress (curve1, black square), in NC2 without stress (curve 2, red circle) and in NC2 with stress (curve 3, blue triangle). The apparent rate constants on the unstressed specimen were the lowest in these three cases, except the data at -0.1 V. $S_2O_3^{2-}$ increased the apparent rate constant by 1.4 to 8.8 times in this potential range, and stress and $S_2O_3^{2-}$ increased it by 0.56 to 4.4 fold. On the active spots (Figure 4.14c), $S_2O_3^{2-}$ increased the

apparent rate constant by 1.6 to 5 times, and $S_2O_3^{2-}$ with stress increased it by 13 to 34 times. On the region between these two limiting cases, $S_2O_3^{2-}$ increased the apparent rate constant by 2.3 to 5.4 times, and $S_2O_3^{2-}$ with stress increased it by 5-45 times. Therefore, it was concluded that the $S_2O_3^{2-}$ effect on

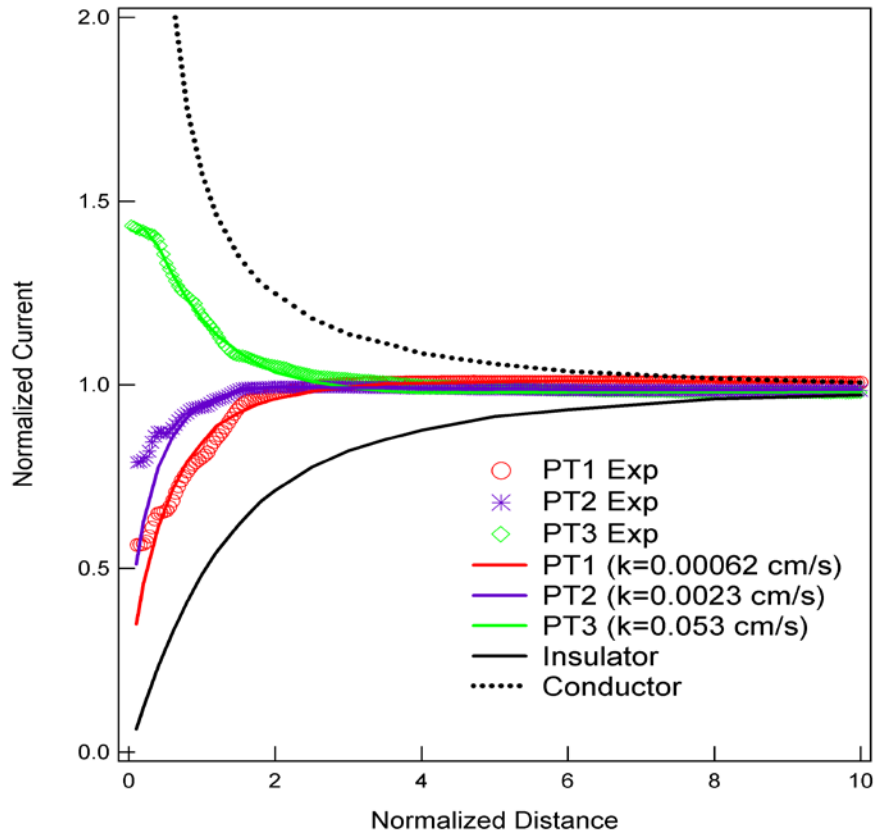
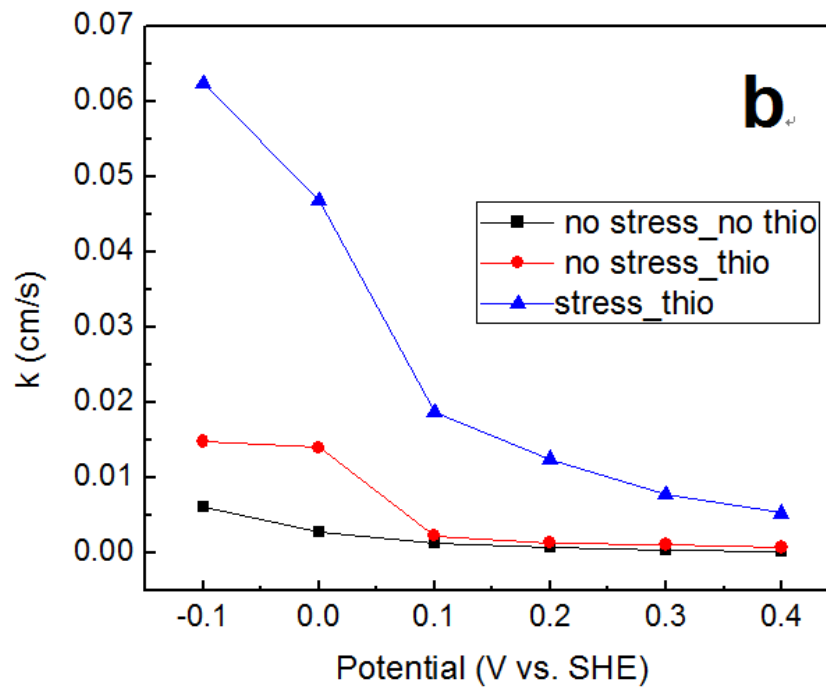
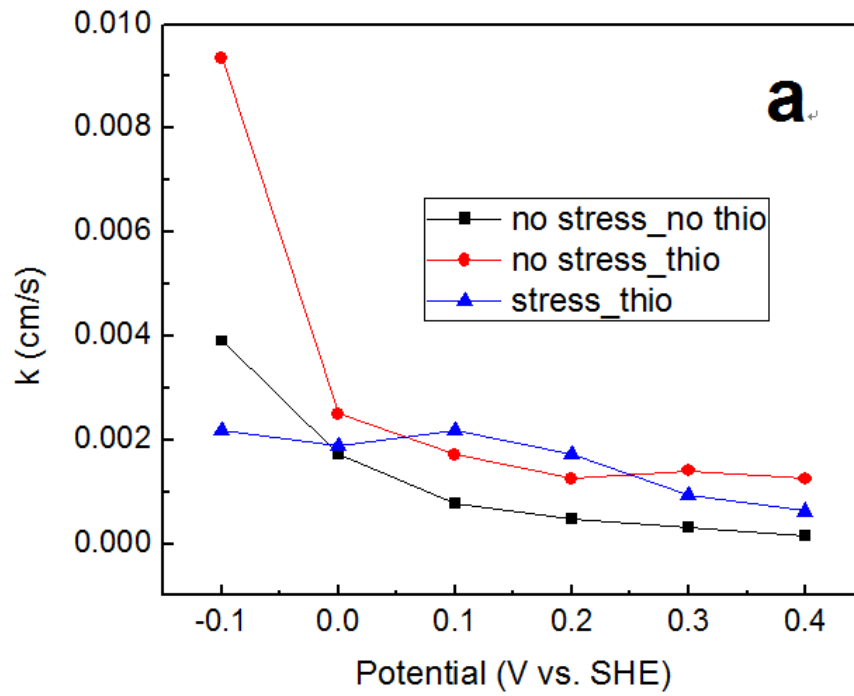


Figure 4.13 PACs toward different active regions on the Alloy 800 specimen with stress in NC2 at 0.1 V. (PT1 (circle): non-active region, PT2 (star): between non-active and active region and PT3 (diamond): active region). The solid lines close to the symbols are the simulation curves in the corresponding conditions, and the bottom solid line is the simulation data for an insulator surface and the dotted line is the simulation data for a conductive surface. Other parameters are the same as those in Figure 4.12.



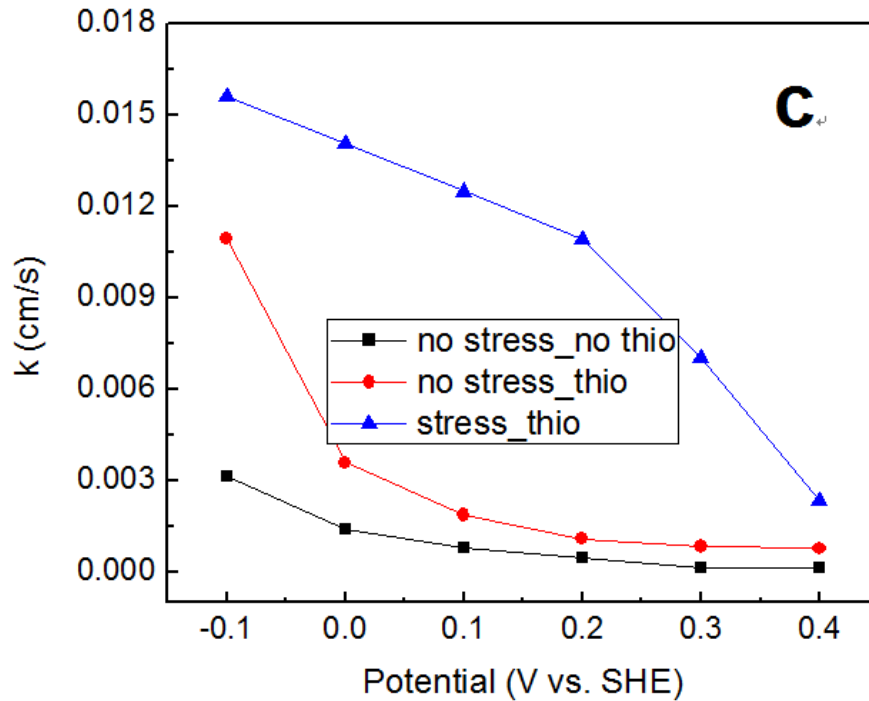


Figure 4.14 Simulated data of apparent rate constants (k) obtained on different reactive regions of Alloy 800. (a): non-reactive region; (b): the region with current between the highest and lowest ones; and (c): reactive region. Potential on tip: 0.65 V.

degradation of the oxide film was mainly on the active regions, and the same phenomenon was observed due to $S_2O_3^{2-}$ and stress. The synergistic effect of $S_2O_3^{2-}$ and stress was mainly contributed by the active regions.

4.2 Conclusions

Scratch tests with electrochemical measurements and SECM were

employed to study the effects of $S_2O_3^{2-}$ and stress on the corrosion behavior of alloy 800 in simulated nuclear steam generator secondary side crevice chemistries suggested by AECL. Cyclic potentiodynamic polarization tests showed that $S_2O_3^{2-}$ significantly reduced the corrosion potential and pitting potential and increased the passive current. Scratch tests and SECM experiments revealed that $S_2O_3^{2-}$ enhanced the metal/oxide dissolution and retarded the repassivation process after the passive film was mechanically damaged by a scratch. On the other hand, stress applied to alloy 800 degraded the corrosion resistance of the alloy by decreasing pitting potentials, increasing passive current and surface reactivity/conductivity. Upon breaking down the passive film, stress increased the repassivation time. Stress activated the grain boundaries on the C-ring specimens, and caused crack initiation possibly at grain boundaries, at triple points and at inclusions in an aggressive solution, such as NC2. Optical investigations on the tested specimens support the above observations and conclusions. A synergistic effect between $S_2O_3^{2-}$ and stress on the corrosion degradation of alloy 800 was also clearly observed in our experiments. The semi-quantitative simulation results of the apparent rate constants revealed that the synergistic effect between $S_2O_3^{2-}$ and stress was mainly contributed by the active regions on the specimen surface.

References

1. R. W. Staehle and J. A. Gorman, Quantitatively Assessment of Submodes of Stress Corrosion Cracking on the Secondary Side of Steam Generator Tubing in Pressurized Water Reactors: Part 3, *Corrosion* 60 (2004), p. 115.

2. H. H. Horowitz, Chemisorption and catalysis in polythionic/thiosulfate stress corrosion cracking, *J. Electrochem. Soc.* 132 (1985), p. 2064.
3. T. Shibata, R. Toyota and T. Haruna, Effect of thiosulfate ions on the stress corrosion cracking of type 304 stainless steel, Paper 228/1 (1996).
4. R. Bandy, R. Roberge and R. C. Newman, Low-temperature stress corrosion cracking of sensitized Inconel 600 in tetrathionate and thiosulfate solutions, *Corrosion* 39 (1983), p. 391.
5. R. C. Newman, K. Sieradzki and H. S. Isaacs, Stress-corrosion cracking of sensitized type 304 stainless steel in thiosulfate solutions, *Metall. Trans., A: Physical Metallurgy and Materials Science* 13 (1982), p. 2015.
6. E.-H. Lee, K.-M. Kim and U.-C. Kim, Stress combination cracking of Alloy 600 in a high-temperature water containing sulfate and thiosulfate, *Key Eng. Mater.* 277-279 (2005), p. 644.
7. I. J. Yang, Localized corrosion of alloy 600 in thiosulfate solution at 25 DegC, *Corrosion* 49 (1993), p. 576.
8. J. G. Gonzalez-Rodriguez, V. M. Salinas-Bravo and A. Martinez-Villafane, Low-temperature stress corrosion cracking of alloy 601 in thiosulfate and chloride solutions, *Corrosion* 55 (1999), p. 38.
9. T. Shibata, T. Haruna, S. Fujimoto, and S. Nakane, Stress corrosion cracking of SUS 316L stainless steel in the chloride solution containing thiosulfate ion by the slow strain rate technique, *Tetsu to Hagane* 77 (1991), p. 1511.

10. M. Huang, Use of ChemSolv to predict crevice chemistry in ACR-1000 SG, Atomic Energy of Canada Ltd. (Report), 10820-36000-470-001, 2009.
11. R. H. Dinegar, R. H. Smellie and V. K. La Mer, Kinetics of the acid decomposition of sodium thiosulfate in dilute solutions, *J. Am. Chem. Soc.* 73 (1951), p. 2050.
12. M. Gomez-Duran and D. D. Macdonald, Stress corrosion cracking of sensitized Type 304 stainless steel in thiosulfate solution: I. Fate of the coupling current, *Corros. Sci.* 45 (2003), p. 1455.
13. E. A. Ashour, E. A. Abd El Meguid and B. G. Ateya, Effects of thiosulfate on susceptibility of type 316 stainless steel to stress corrosion cracking in 3.5% aqueous sodium chloride, *Corrosion* 53 (1997), p. 612.
14. Z. Fang and R. W. Staehle, Effects of the valence of sulfur on passivation of alloys 600, 690, and 800 at 25 DegC and 95 DegC, *Corrosion* 55 (1999), p. 355.
15. Z. Fang and R. W. Staehle, The effects of chloride and thiosulfate on the passivation of Alloys 600, 690 and 800, TMS Annual Meeting and Exhibition, New Orleans, Louisiana, 2001.
16. R. W. Staehle and J. A. Gorman, Quantitatively Assessment of Submodes of Stress Corrosion Cracking on the Secondary Side of Steam Generator Tubing in Pressurized Water Reactors: Part 1, *Corrosion* 59 (2003), p. 931.

17. R. W. Staehle and J. A. Gorman, Quantitatively Assessment of Submodes of Stress Corrosion Cracking on the Secondary Side of Steam Generator Tubing in Pressurized Water Reactors: Part 2, *Corrosion* 60 (2004), p. 5.
18. H.-S. Kuo, H. Chang and W.-T. Tsai, The corrosion behavior of AISI 310 stainless steel in thiosulfate ion containing saturated ammonium chloride solution, *Corros. Sci.* 41 (1999), p. 669.
19. Y. Y. Chen, H. C. Shih, Y. M. Liou, L. H. Wang, and J. C. Oung, Stress corrosion cracking of type 321 stainless steels under simulated petrochemical conditions containing thiosulfate and chloride, *Corrosion* 62 (2006), p. 781.
20. Y. Y. Chen, Y. M. Liou and H. C. Shih, Stress corrosion cracking of type 321 stainless steels in simulated petrochemical process environments containing hydrogen sulfide and chloride, *Mater. Sci. Eng. A407* (2005), p. 114.
21. S. Roychowdhury, S. K. Ghosal and P. K. De, Role of environmental variables on the stress corrosion cracking of sensitized AISI type 304 stainless steel (SS304) in thiosulfate solutions, *J. Mater. Eng. Perform.* 13 (2004), p. 575.
22. H. M. Ezuber, Corrosion behavior of heat-treated duplex stainless steels in saturated carbon dioxide-chloride solutions, *J. ASTM Int.* 2 (2005), p. No pp. given.
23. E. H. Lee, K. M. Kim and U. C. Kim, Effects of reduced sulfur on the corrosion behavior of Alloy 600 in high-temperature water, *Mater. Sci.*

- Eng., A: Structural Materials: Properties, *Microstructure and Processing* A449-A451 (2007), p. 330.
24. W. Yang, Z. Lu, D. Huang, D. Kong, G. Zhao, and J. Congleton, Caustic stress corrosion cracking of nickel-rich, chromium-bearing alloys, *Corros. Sci.* 43 (2001), p. 963.
 25. P. M. Singh, J. J. Perdomo, J. E. Oteng, and J. Mahmood, Stress corrosion cracking and corrosion fatigue cracking of a duplex stainless steel in white water environments, *Corrosion* 60 (2004), p. 852.
 26. M. P. H. Brongers, G. H. Koch and A. K. Agrawal, The use of atomic force microscopy to detect nucleation sites of stress corrosion cracking in type 304 stainless steel, ASTM Spec. Tech. STP 1401 (2000), p. 394.
 27. A. H. Qureshi, N. Hussain, J. I. Akhtar, and K. A. Shahid, Stress corrosion cracking (SCC) behaviour of low alloy steel in thiosulfateO environment, *Adv. Mater.*-2001, Proc. Int. Symp., 7th, Islamabad, Pakistan, Sept. 17-21, 2001 (2001), p. 380.
 28. F. Zucchi, G. Trabanelli and V. Grassi, Stress corrosion cracking of 13% Cr martensitic steels in sodium chloride solutions in the presence of thiosulphate, *Mater. Corros.* 51 (2000), p. 207.
 29. M. Casales, M. A. Espinoza-Medina, A. Martinez-Villafane, V. M. Salinas-Bravo, and J. G. Gonzalez-Rodriguez, Predicting susceptibility to intergranular stress corrosion cracking of Alloy 690, *Corrosion* 56 (2000), p. 1133.

30. B. T. Lu and J. L. Luo, Crack initiation and early propagation of X70 steel in simulated near-neutral pH groundwater, *Corrosion* 62 (2006), p. 723.
31. B. T. Lu and J. L. Luo, Relationship between yield strength and near-neutral pH stress corrosion cracking resistance of pipeline steels-an effect of microstructure, *Corrosion* 62 (2006), p. 129.
32. B. T. Lu, J. L. Luo and Y. C. Lu, A Mechanistic Study on Lead-Induced Passivity-Degradation of Nickel-Based Alloy, *J. Electrochem. Soc.* 154 (2007), p. C379.
33. Y. F. Cheng and J. L. Luo, A comparison of the pitting susceptibility and semiconducting properties of the passive films on carbon steel in chromate and bicarbonate solutions, *Appl. Surf. Sci.* 167 (2000), p. 113.
34. R. Dehmlaei, M. Shamanian and A. Kermanpur, Microstructural changes and mechanical properties of Incoloy 800 after 15 years service, *Mater. Charact.* 60 (2009), p. 246.
35. R. Zhu, C. Nowierski, Z. Ding, J. J. Noeel, and D. W. Shoesmith, Insights into Grain Structures and Their Reactivity on Grade-2 Ti Alloy Surfaces by Scanning Electrochemical Microscopy, *Chemistry of Materials* 19 (2007), p. 2533.
36. A. Davoodi, J. Pan, C. Leygraf, and S. Norgren, Probing of local dissolution of Al alloys in chloride solutions by AFM and SECM, *Appl. Surf. Sci.* 252 (2006), p. 5499.
37. R. Zhu, Development and applications of scanning electrochemical microscopy (*Ph. D. Thesis*), 2008.

38. W. Li and D. Y. Li, Determination of the yield locus using a Kelvin probing method, *J. Phys. D: Appl. Phys.* 37 (2004), p. 948.
39. M. E. Broczkowski, R. Zhu, Z. Ding, J. J. Noel, and D. W. Shoesmith, Electrochemical, SECM, and XPS studies of the influence of H₂ on UO₂ nuclear fuel corrosion, *Materials Research Society Symposium Proceedings* 932 (2006), p. 449.
40. A. Davoodi, J. Pan, C. Leygraf, and S. Norgren, Integrated AFM and SECM for in situ studies of localized corrosion of Al alloys, *Electrochim. Acta* 52 (2007), p. 7697.
41. M. Huang, Degradation of SG Tubing Materials in Reduced Sulphur Environments, 2009.
42. G38-01, *Standard practice for Making and Using C-Ring Stress-Corrosion Test Specimens* (Reapproved 2007).
43. A. Dinu, M. Fulger, D. Ionescu, L. Velciu, and M. Radulescu, Electrochemical studies on stress corrosion cracking of Incoloy-800 in caustic solution Part I: As received samples, *Nuclear Technology & Radiation Protection* (2005), p. 74.
44. E. El-Magd, G. Nicolini and M. Farag, Effect of carbide precipitation on the creep behavior of alloy 800HT in the temperature range 700 to 900 Deg, *Metall. Mater. Trans. A Physical Metallurgy and Materials Science* 27A (1996), p. 747.

45. R. Zhu and Z. Ding, Enhancing image quality of scanning electrochemical microscopy by improved probe fabrication and displacement, *Can. J. of Chem.* 83 (2005), p. 1779.
46. G. T. Burstein and D. H. Davies, The effects of anions on the behavior of scratched iron electrodes in aqueous solutions, *Corros. Sci.* 20 (1980), p. 1143.
47. G. T. Burstein and P. I. Marshall, Growth of passivating films on scratched 304L stainless steel in alkaline solution, *Corros. Sci.* 23 (1983), p. 125.
48. P. I. Marshall and G. T. Burstein, The effects of pH on the repassivation of 304L stainless steel, *Corros. Sci.* 23 (1983), p. 1219.
49. R. Ke and R. Alkire, Surface analysis of corrosion pits initiated at manganese sulfide inclusions in 304 stainless steel, *J. Electrochem. Soc.* 139 (1992), p. 1573.
50. W. T. Tsai, Z. H. Lee, J. T. Lee, M. C. Tsai, and P. H. Lo, Pitting and stress corrosion cracking behavior of Inconel 600 alloy in thiosulfate solution, *Mater. Sci. Eng., A: Structural Materials: Properties, Microstructure and Processing* A118 (1989), p. 121.
51. R. Zhu, Z. Qin, J. J. Noeel, D. W. Shoesmith, and Z. Ding, Analyzing the influence of alloying elements and impurities on the localized reactivity of titanium Grade-7 by scanning electrochemical microscopy, *Anal. Chem.* 80 (2008), p. 1437.

52. C. Nowierski, J. J. Noel, D. W. Shoesmith, and Z. Ding, Correlating surface microstructures with reactivity on commercially pure zirconium using scanning electrochemical microscopy and scanning electron microscopy, *Electrochem. Commun.* 11 (2009), p. 1234.
53. P. Sun, Z. Liu, H. Yu, and M. V. Mirkin, Effect of Mechanical Stress on the Kinetics of Heterogeneous Electron Transfer, *Langmuir* 24 (2008), p. 9941.

Chapter 5

The Studies of PbSCC of Alloy 800 at 300°C

by Using Direct Current Potential Drop

Technique

5.1 Results and Discussions

5.1.1 Calibration of Potential Drop System

5.1.1.1 Calibration curve of alloy 800 DCB specimen at room temperature

Figure 5.1 shows the calibration curve with potential as a function of real crack length. The potential value was recorded at different crack lengths for the same specimen at room temperature. The potential gradually increased from 0.185 mV to about 0.216 mV. The fitted curve indicated that the potential values increased almost linearly as the crack propagated.

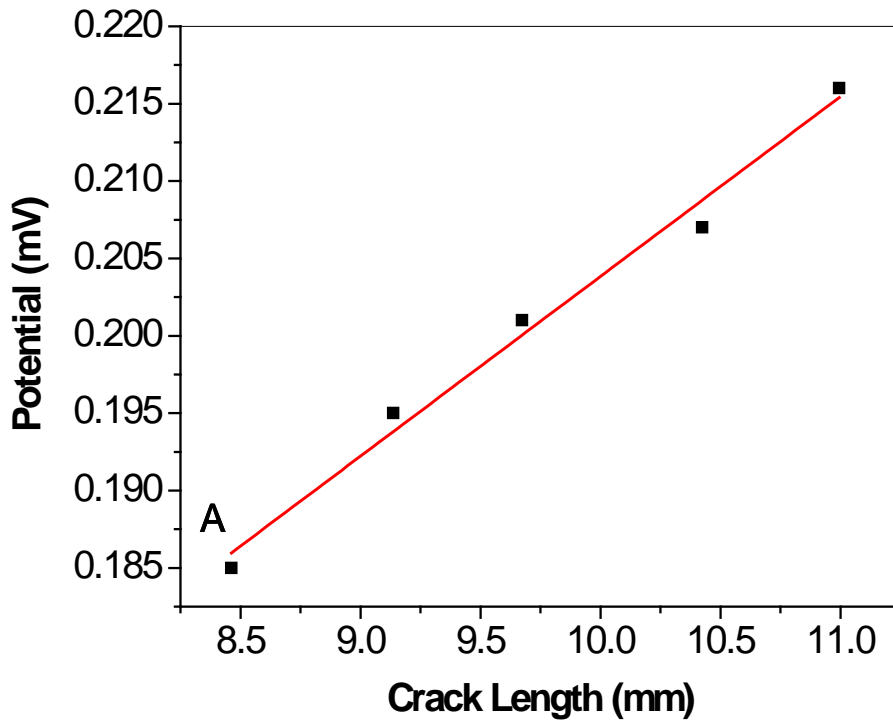


Figure 5.1 The calibration curve of actual potential values vs. real crack length for alloy 800 at room temperature

According to the fitted results, the intercept value is 8.77×10^{-5} V, and the slope is about 1.16×10^{-5} V/mm. The relatively small standard error values and R^2 of 0.9847 indicated a good fit. The fitted slope of the calibration curve can be used to predict the real-time crack length in the later measurements.

To eliminate the effect of pre-crack and system error (e.g. electrical wire resistance), normalized potentials and crack lengths are usually used [11]. Merah and et al. used the normalized calibration curve for the crack length measurement at room temperature [12]. The normalized calibration curve was proposed in Equation 5.1.

$$\frac{V}{V_0} = 1 + C \left(\frac{\Delta a}{W} \right)^m \quad (5.1)$$

where C , m are constants and can be obtained from the fitting results. V/V_0 stands for the normalized potential and a/W is the normalized crack length. In this work, point A in Figure 5.1 can be considered as the initial reference point, so $V_0 = V_A$ and $\Delta a = a - a_A$. The normalized calibration curve was plotted in Figure 5.2, which predicts the crack length with the $\Delta a/W$ value ranging from 0 to 0.3. The solid symbols in Figure 5.2 are experimental results, which are consistent with the fitted results. According to the fitted results, the value of “C” is 1.21 with a standard deviation of 0.349, and the value of “m” is 0.875 with a standard deviation of 0.112. The adjusted R^2 value of 0.9666 indicated a high degree of fit. Consequently, the calibration curve can be described as follows,

$$\frac{V}{V_0} = 1 + 1.21 \times \left(\frac{\Delta a}{W} \right)^{0.875} \quad (5.2)$$

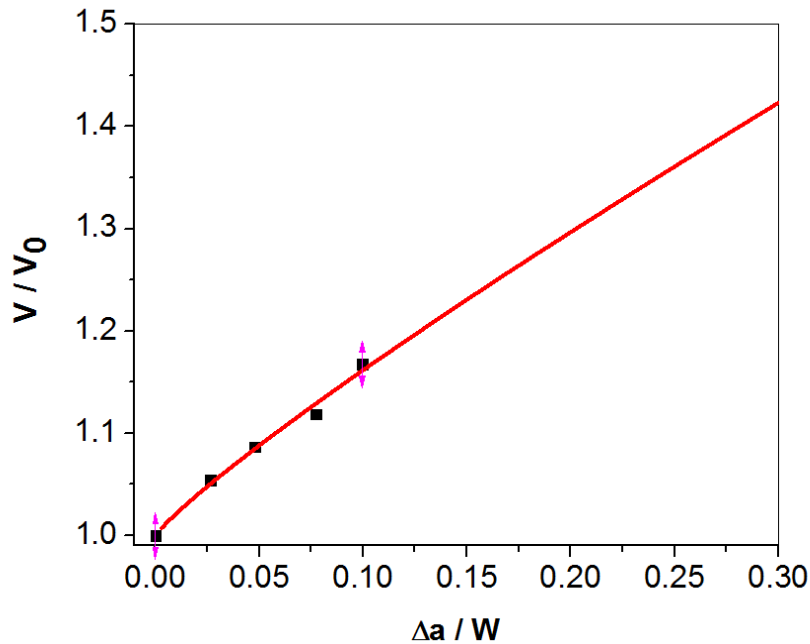


Figure 5.2 The normalized calibration curve of normalized potential values vs. normalized crack length for alloy 800 at room temperature

5.1.1.2 Temperature dependence of the resistivity of alloy 800 DCB specimen

The calibration curve in Figure 5.2 provides a precise prediction of crack propagation for alloy 800 DCB specimen at room temperature. However, the temperature dependence of the calibration curve is necessary for the real-time monitoring of crack propagation at 300°C. Near room temperature, the electric resistance of a typical metal increases linearly with rising temperature. However, the slope changes somewhat with temperature. The modern form of Matthiessen's Rules provides a general equation to sum up the total resistance as a function of temperature, shown in equation 5.3 [13, 14].

$$R = R_0 + aT^2 + bT^5 + cT \quad (5.3)$$

where R_0 is the temperature independent electrical resistivity due to impurities or environmental impact. The constant a , b , and c are coefficients which depend upon the material's properties.

Ikeda et al. investigated the electrical resistivity in ferromagnetic Ni-based alloys, and they found that the slope of ρ - T curve is almost independent of the solute concentration when $T > T_c$ (Curie temperature) [15]. However, the temperature dependence between 77 and 700K of the electrical resistivity for Ni-Pt alloy showed that the electrical resistivity gradually increases with rising platinum concentration [16]. Jones et al. studied the electrical resistivity of Fe-Cr- and Ni-Cr- based amorphous alloys, such as $Fe_{80-x}Cr_xB_{12}Si_8$ and $Ni_{80-x}Cr_xB_{12}Si_8$. They found that the temperature dependence exhibited a linear relationship at high temperatures [17].

To have a better understanding of the temperature dependence of alloy 800 DCB specimen, the potential value was recorded as a function of temperature, with a constant direct current going through the specimen. The potential changed from 0.51 mV to more than 0.56 mV while the temperature rose from 19°C to 300°C. The resistivity of the material can be expressed as

$$R = \frac{\ell \cdot \rho}{A} \quad (5.4)$$

where ℓ is the length of the material, A is the cross-sectional area, and ρ is the electrical resistivity. The value of ρ varies with the change of temperature, so the potential change indicates the resistivity change of alloy 800 under constant direct current.

The normalized resistivity is obtained via dividing the resistance at different temperatures by the resistance at an initial environmental temperature. Figure 5.3 shows the normalized resistance as a function of temperature. The solid symbols in the figure represent the experimental results, and the solid line is obtained by fitting the results by a polynomial model. The expression of the normalized resistance as a function of Kelvin

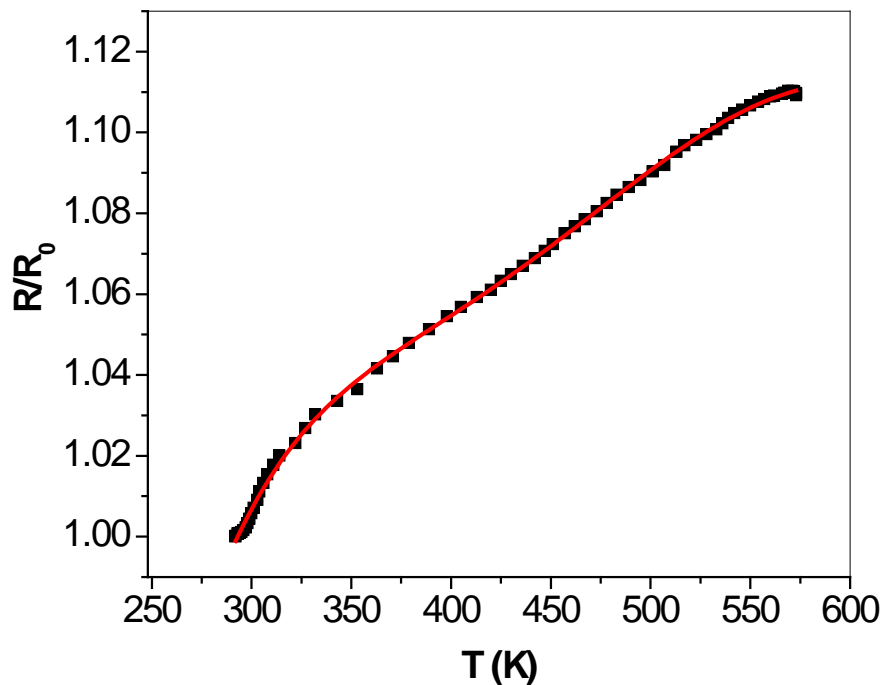


Figure 5.3 The temperature dependence of the normalized resistance of alloy 800 DCB specimen from 292 to 573 K.

temperature can be described as follows

$$R/R_0 = a + bT + cT^2 + dT^5 \quad (5.5)$$

where a, b, c, d are all constant and their values and standard error are listed in Table 5.1. The constant for item T^5 is so small that it can sometimes be neglected.

	a	b	c	d
Value	-3.03379	0.04237	-1.75722×10^{-4}	1.41359×10^{-13}
Standard Error	0.58717	0.00712	3.41076×10^{-5}	4.12919×10^{-14}

Table 5.1 The values and standard errors of the constants in temperature dependence curve (shown in Equation 5.5).

5.1.1.3 Calibration curve of alloy 800 DCB specimen at 300°C

The temperature dependence provides a relatively precise prediction of the resistivity of alloy 800 at different temperature. The operating temperature of

the CANDU nuclear reactor is 300°C, and it is also the experimental temperature of the potential drop system, so it is important to obtain the calibration curve at 300°C mathematically since it is extremely difficult to carry out the calibration experiments at high temperature. According to equation 5.4, we know that

$$\frac{R_{293K}}{R_{573K}} = \frac{\rho_{293K}}{\rho_{573K}} \quad (5.6)$$

The calibration curve at 293 K is shown in Figure 5.2, so the calibration curve at 573 K can be obtained by taking into account the temperature dependence of the resistivity of alloy 800.

According to equation 5.5, we can obtain

$$\frac{R_{300^{\circ}C}}{R_{20^{\circ}C}} = \frac{R_{573K}}{R_{293K}} = \frac{a + bT_1 + cT_1^2 + dT_1^5}{a + bT_0 + cT_0^2 + dT_0^5} \quad (5.7)$$

Inputting the values of a, b, c, d, $T_1 = 573$ K, and $T_0 = 293$ K, the ratio of two different temperature can be obtained as follows,

$$\frac{R_{300^{\circ}C}}{R_{20^{\circ}C}} = 1.11 \quad (5.8)$$

Consequently, the calibration curve at 300°C can be calculated as follows:

$$\frac{V}{V_0} = 1 + 1.11 * C \left(\frac{\Delta a}{W} \right)^m = 1 + 1.34 \times \left(\frac{\Delta a}{W} \right)^{0.875} \quad (5.9)$$

This calibration curve can be used to predict the crack growth of alloy 800 DCB specimen at 300°C.

Another simplified approach to estimate crack growth is by the ratio of voltage change and crack length increase. According to the slope in Figure 5.1 and the temperature dependence in equation 5.8, the slope can be expressed as follows,

$$S = \frac{\Delta V}{\Delta a} = 1.11 * 1.16 \times 10^{-5} \text{ V/mm} = 1.29 \times 10^{-5} \text{ V/mm} \quad (5.10)$$

This slope would be used to predicate the real crack length in Pb-contaminated and Pb-free conditions in the next section.

5.1.2 The effect of Pb on the SCC of alloy 800 DCB specimen by real time crack propagation monitoring

5.1.2.1 Comparison of Voltage Changes in Pb-contaminated and Pb-free Conditions

Figure 5.4 shows potential drop measurements of the alloy 800 DCB specimen with constant displacement load in Pb-contaminated conditions at 300°C. The raw potential data was plotted as a function of time. With the temperature increase from 19°C to 300°C in the autoclave, the potential increased

sharply from 0.508 mV to 0.563 mV due to the positive temperature dependence of the resistivity of alloy 800. After that, the potential increased gradually to 0.571 mV after about 12,000 minutes, during which the temperature was maintained constant. The increase in potential was attributed to the crack advance in the crack tip of the alloy 800 DCB specimen. The geometry change of the specimen caused by the crack propagation increased the resistance of the specimen by increasing its equivalent length and decreasing its cross-sectional area, which resulted in

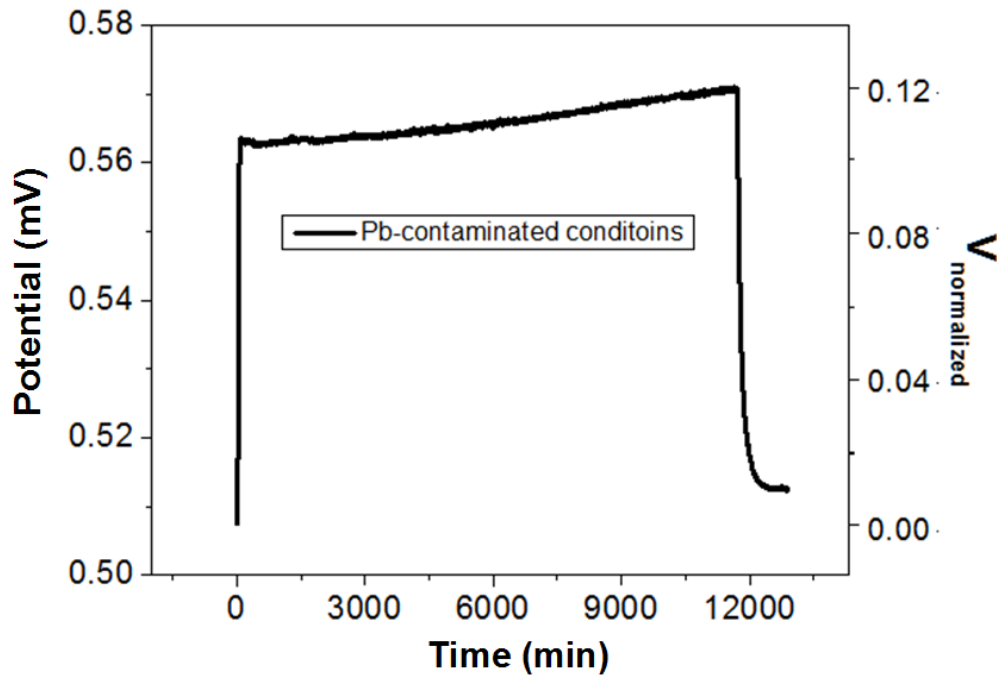


Figure 5.4 Normalized potential of alloy 800 DCB specimen as a function of time in Pb-contaminated neutral crevice chemistries conditions.

the change of the voltage values in the potential drop system. The initial potential of 0.508 mV prior to heating was considered as a reference potential for the

potential normalization. The corresponding normalized potential scale was presented in the vertical axis on the right. The heating of the autoclave was shut down at 11,700 minutes, and the potential started to drop at the same time. Finally, the potential remained at 0.513 mV when the temperature becomes ambient. The potential change of 8 μV at 300°C indicated an increase in crack length, and the quantitative calculation of the crack length increase would be discussed in the later sections.

The potential drop measurement of alloy 800 DCB specimen in Pb-free neutral crevice chemistries conditions was also recorded. The temperature dependence patterns of the Pb-free condition were similar with that of Pb-contaminated conditions, with a sharp potential increase when the temperature was increasing. Figure 5.5 shows a comparison of alloy 800 DCB specimen in Pb-contaminated and Pb-free conditions, during a crack propagation process at 300°C. When temperature first reached 300°C, the initial potentials in each condition were considered as a reference voltage V_0 in Pb-contaminated and Pb-free conditions, respectively. The curve with a positive slope indicated notable crack propagation in Pb- contaminated conditions. The flat bottom curve implied that the crack propagation in Pb-free conditions was not obvious compared to that in Pb-contaminated conditions. The linear solid lines were fitted curves, and the equations of the fitting results with standard errors are shown in Table 5.2, which provides a quantitative perspective to estimate the difference of the crack propagation behaviour in Pb-contaminated and Pb-free conditions. In the Pb-contaminated condition, the slope of normalized potential vs. time is 7.88×10^{-7}

min^{-1} , which is about 25 times the value of $3.21 \times 10^{-8} \text{ min}^{-1}$ in Pb-free conditions. This implied that the crack propagation rate of alloy 800 DCB specimen in Pb-contaminated condition is about 25 times that in Pb-free conditions at 300°C . The standard errors of the slope for Pb-free and Pb-contaminated conditions are less than 5%, which indicated a good fit.

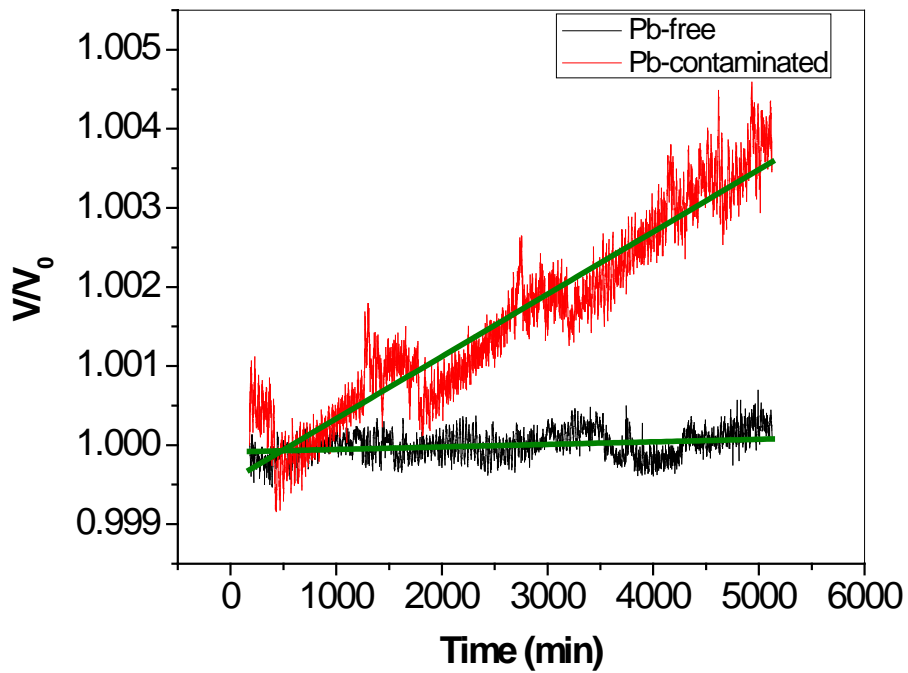


Figure 5.5 Comparison of Alloy 800 DCB specimens with applied stress in Pb-contaminated (top) and Pb-free (bottom) neutral crevice chemistries conditions

Equation	$y = a + b \cdot x$		
		Value	Standard Error
Pb-free	Intercept	0.99991	4.81×10^{-6}
Pb-free	Slope	3.21×10^{-8}	1.59×10^{-9}
Pb-contaminated	Intercept	0.99955	1.08×10^{-5}
Pb-contaminated	Slope	7.88×10^{-7}	3.57×10^{-9}

Table 5.2 Linear fitting results with stand errors of crack propagation curves for alloy 800 DCB specimen with applied stress in Pb contaminated and Pb-free conditions at 300°C.

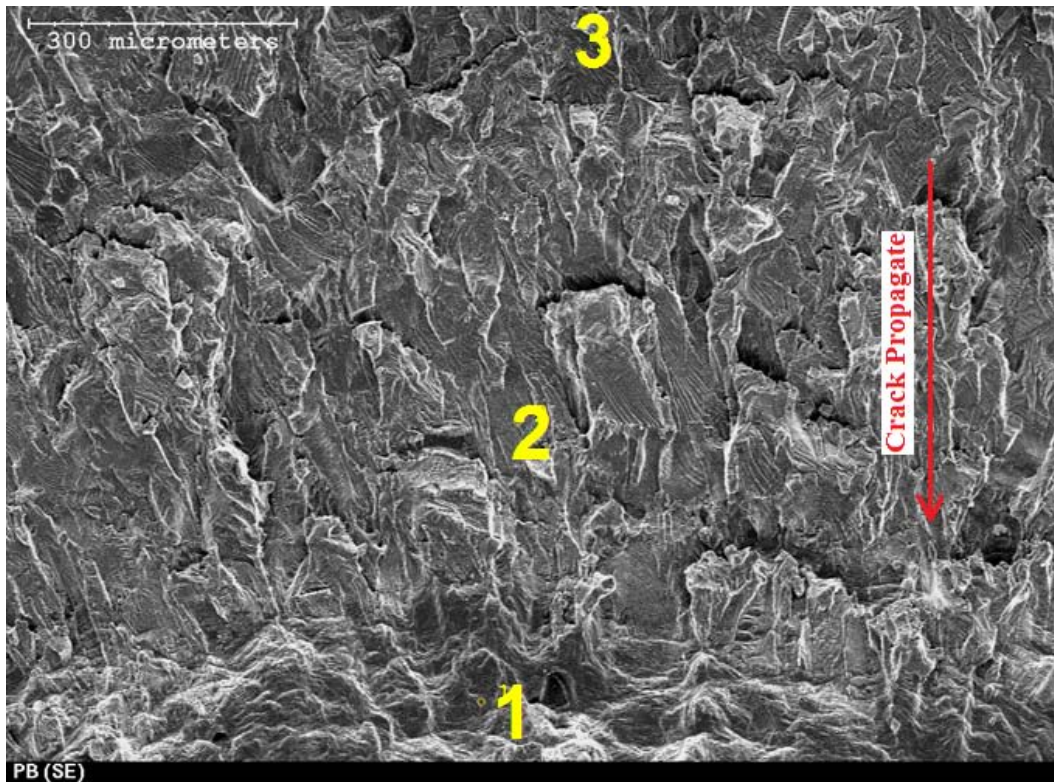
In this work, Pb contaminants significantly increased the CPR of the alloy 800 DCB specimen in neutral crevice conditions at 300°C. Actually, PbSCC of steam generator materials have been observed and reported for several decades. Copson and Dean first examined the behaviour of alloy 600 in Pb-containing environments and found that Pb would accelerate the occurrence of SCC in this alloy [18]. Numerous researchers have been working on the mechanism of PbSCC of the main SG tubing materials including alloys 600, 690 and 800. However, the precise mechanism is still not yet fully understood. Staehle proposed that a stress is applied to the crack tip leading to the propagation of the crack, as a result of the gradual increase in the volume of corrosion products [19]. In solution chemistry, the Pb present can also be incorporated into the structure of the passive film by a hydration-adsorption process. To be exact, the Pb is first hydrated into lead hydroxide and then it will form mixed hydroxides by being adsorbed into the passive film [20]. Another possibility is a point defect model; the metallic cation

vacancies migrate from the film/electrolyte interface to the film/metal interface, and the adsorbed lead ions on the film surface may enter the passive film successively by combining with the metallic cation vacancies [21-23]. In addition, a correlation between the film rupture ductility and PbSCC susceptibility of alloy 800 has been studied by our group. The results showed that film rupture at the crack tip might be the controlling factor. During this process, the incorporation of lead impurities decreases the ductility of the passive film, and increases the susceptibility to PbSCC [24].

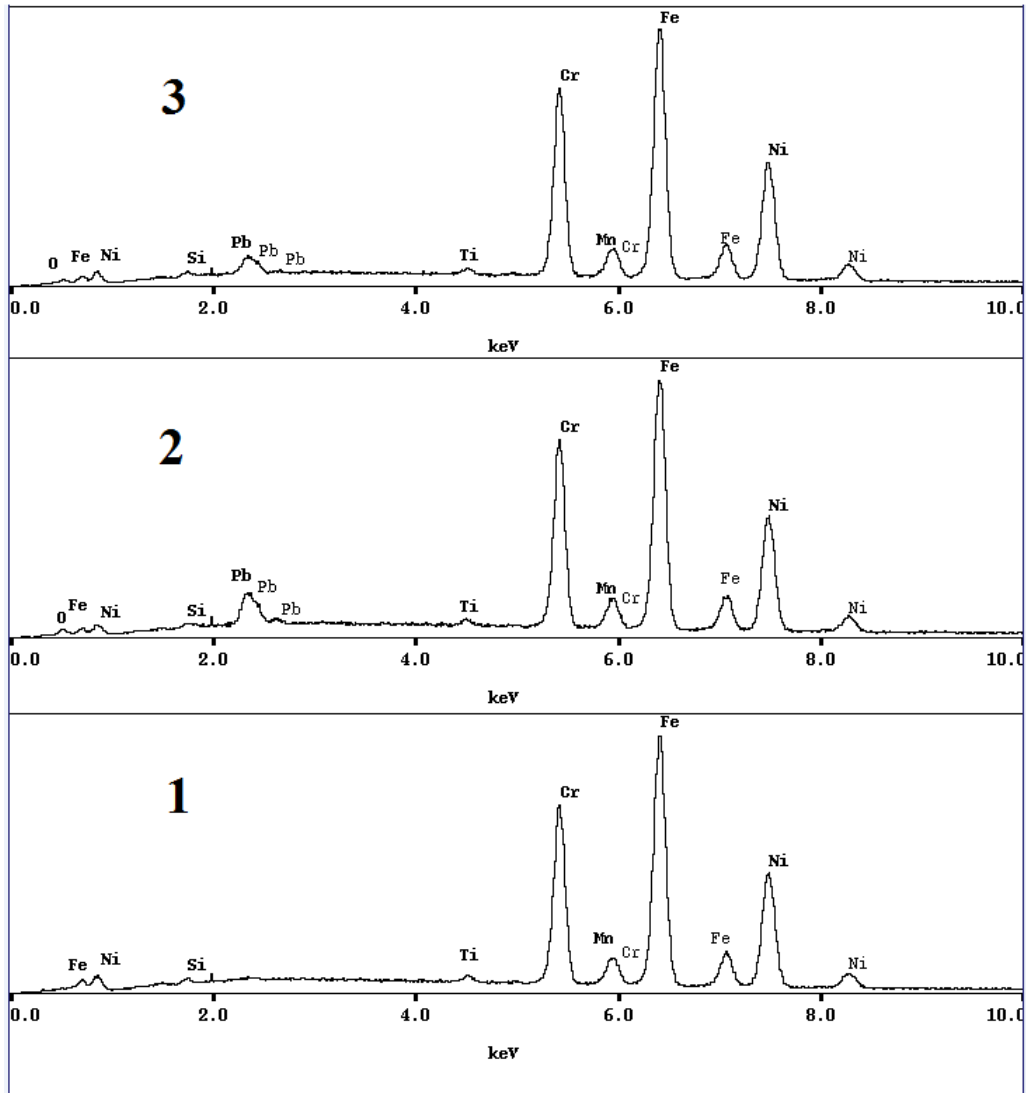
Figure 5.6 (a) shows a cross-sectional view of alloy 800 DCB arm after being opened. There are three different regions shown in the figure. Region (1) indicated the fast fracturing region, caused by the opening process, region (2) shows the crack growth arrest in Pb-contaminated condition, and region (3) stands for the fatigue pre-crack. The more general illustration of the complete three regions can be seen in Figure 5.8. Energy-dispersive X-ray spectroscopy (EDX) was also carried out for all three different regions. The corresponding EDX curves are shown in the Figure 5.6 (b). As you can see, there is no lead present in the fast fracturing region (1), since it is the arm opening procedure after a potential drop measurement in the Pb-contaminated condition. However, lead was observed in both the crack growth region and the pre-crack regions, and the concentration of lead present in the crack growth region is higher than that in the pre-crack region. The lead was not from the left over solution on the specimen, since the specimen was cleaned well in both ethanol and distilled water with an ultrasonic bath. This observation indicated that the lead did play an important role during the crack

propagation process at high temperature. The higher concentration in the crack growth region may be due to the fact that lead attacked the passive film and it stayed on the surface of the specimen as a form of product, which accelerated the crack propagation rate of the alloy 800 DCB specimen at 300°C. This is consistent with the mechanism proposed by Lu and et al. that Pb was incorporated into the passive film by a hydration-adsorption process [20].

Figure 5.7 shows the expanded image of the crack growth region of the same specimen in Pb-contaminated condition at 300°C. The intergranular attack (IGA) was observed in the crack growth region. The transgranular attack (TGA) was also suspected in this image. The intergranular cracks were also observed in the failure analysis of alloy 800 at high temperature [26].



(a)



(b)

Figure 5.6 Comparison of different spots in (1) fast fracturing region (2) crack growth region, and (3) fatigue pre-crack region. (a) SEM image comparison of different spots, (b) Comparison of lead composition at different spots by EDX.

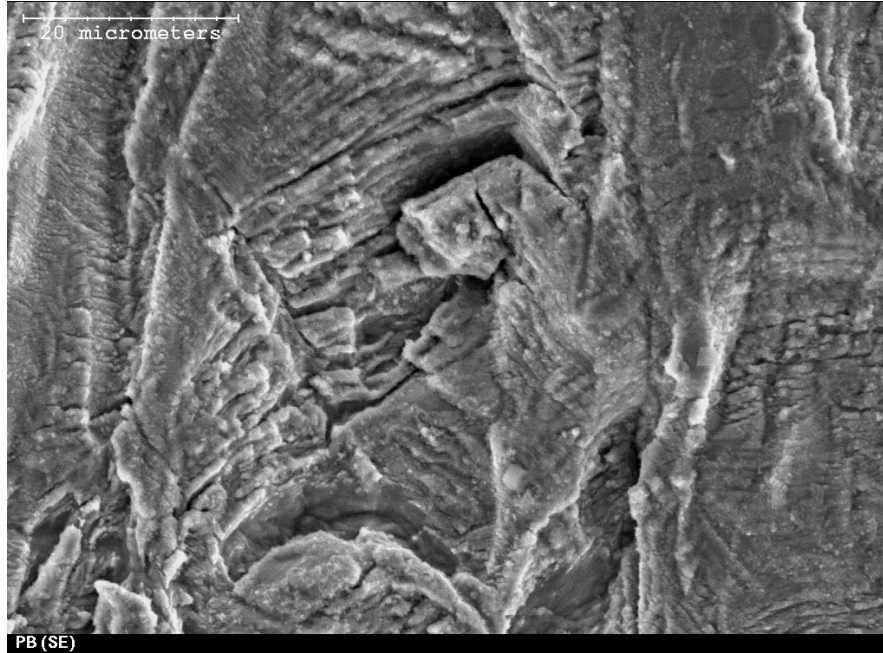


Figure 5.7 The expanded SEM image of the crack arrest on the alloy 800 DCB specimen in the Pb-contaminated neutral crevice chemistries conditions.

5.1.2.2 The Calculation of the Predicated Crack Length Increase by Calibration Curves

With the calibration curves of alloy 800 DCB specimen at 300°C, we are able to predicate the crack propagation rates in Pb-contaminated and Pb-free neutral crevice chemistries conditions. We are going to discuss the predicted crack growths following a non-linear calibration curve and linear calibration curve, respectively.

(a) *Non-linear calibration method*

In Pb-contaminated conditions, the normalized potential vs. time curve can be described in the equation 5.11,

$$\frac{V}{V_0} = 1.00 + 7.88 \times 10^{-7} \cdot t \quad (5.11)$$

where t is time in minute. Combining equations 5.9 and 5.11 together, we can obtain the $\Delta a/W$ vs. time curve as follows, which is a non-dimensional crack propagation rate value to estimate the relative crack growth versus the specimen width.

$$\left(\frac{\Delta a}{W} \right)_{\text{Pb-contaminated}} = 7.57 \times 10^{-8} \cdot t^{1.14} \quad (5.12)$$

Following the same calculation procedure, non-dimensional crack propagation rate of alloy 800 DCB specimen in Pb-free conditions can be obtained as well, which is shown in equation 13.

$$\left(\frac{\Delta a}{W} \right)_{\text{Pb-free}} = 1.95 \times 10^{-9} \cdot t^{1.14} \quad (5.13)$$

In Pb-contaminated condition, the effective crack growth time range at 300°C was from the 62nd to 11,700th minute, the t is equal to 11,638 minutes. According to the dimension of the specimen size, $W = 25.40$ mm, so the crack growth

$$[\Delta a]_{\text{Pb-contaminated}} = 0.083 \text{ mm} \quad (5.14)$$

In Pb-free condition, the predicted crack growth can also be calculated following the same procedure, so we can obtain

$$[\Delta a]_{\text{Pb-free}} = 0.0022 \text{ mm} \quad (5.15)$$

(b) Linear calibration method

The crack growth can also be determined by a linear calibration method, which simply transfers the difference in voltage to crack length change by using a linear calibration curve, shown in equation 5.10.

In Pb-contaminated condition, equations 5.10 and 5.11 can be combined to predict the crack growth in neutral crevice chemistries condition. According to Figure 5.3, V_0 is equal to 0.563 mV, so equation 5.11 can be written as

$$\Delta V = 4.44 \times 10^{-7} t \quad (5.16)$$

where ΔV has a unit of mV, and t has unit of minute. If equation 5.10 is inputted to equation 5.16, we can obtain the crack propagation velocity as follows:

$$\begin{aligned}
\text{CPR}_{\text{Pb-contaminated}} &= \Delta a/t = 4.44 \times 10^{-7} / S \\
&= 3.44 \times 10^{-5} \text{ mm/min} = 2.06 \mu\text{m/h}
\end{aligned}
\tag{5.17}$$

where $\text{CPR}_{\text{Pb-contaminated}}$ is the average crack propagation rate in Pb-contaminated condition, and S is the slope in equation 5.10.

During 11,638 minutes crack propagation in Pb-contaminated condition, the crack growth of alloy 800 DCB specimen can be calculated as below.

$$\begin{aligned}
[\Delta a]_{\text{Pb-contaminated}} &= \text{CPR}_{\text{Pb-contaminated}} \cdot t \\
&= 3.44 \times 10^{-5} \cdot 11638 \text{ mm} = 0.401 \text{ mm}
\end{aligned}
\tag{5.18}$$

In the Pb-free condition, the relationship between relative voltage values and time consumed in the autoclave at 300°C can be obtained from Table 5.2,

$$\frac{V}{V_0} = 1.00 + 3.21 \times 10^{-8} \cdot t
\tag{5.19}$$

where the initial voltage value V_0 is 0.601 mV, so the crack propagation rate in Pb-free condition can be calculated according to both equation 5.10 and 5.18.

$$\begin{aligned}
\text{CPR}_{\text{Pb-free}} &= \Delta a/t = (\Delta V/S) / t = 3.21 \times 10^{-8} \cdot V_0 / S \\
&= 1.50 \times 10^{-6} \text{ mm/min}
\end{aligned}
\tag{5.20}$$

Consequently, the crack propagation velocity of the alloy 800 DCB specimen in Pb-free condition can be obtained as follows:

$$\begin{aligned}
 [\Delta a]_{\text{Pb-free}} &= \text{CPR}_{\text{Pb-free}} \cdot t \\
 &= 1.50 \times 10^{-6} \cdot 11638 \text{mm} = 0.017 \text{mm}
 \end{aligned}
 \tag{5.21}$$

From the calculation above, the estimated crack growths in Pb-contaminated and Pb-free conditions at 300°C are about 0.401 mm and 0.017 mm, respectively. The real crack growths determined by SEM will be compared with those predicated values in the next section.

5.1.2.3 The Examination of the Real Crack Length Increases by SEM methods

The actual crack growth length was examined by the SEM using a three-point weighted average method. After potential drop measurements, each test specimen was cleaned in ethanol, distilled water in an ultrasonic bath, and blow-dried in air, after which the specimens were sectioned or opened in air for further SEM examination. According to the ASTM standards, the crack length determination for the double beam type specimen can be carried out by a five-point weighted average method for specimen thickness (B) greater than 5 mm and three-point weighted average for B smaller than 5 mm [25]. The value of a_o is obtained by averaging the first two surface measurements (a_1 and a_5) made at positions a little inward from the surface, and then these values are averaged with those at the three equally spaced (a_2 , a_3 , and a_4) inner measurement points:

$$a_0 = [(a_1 + a_5)/2 + a_2 + a_3 + a_4]/4 \quad \text{for } B > 5 \text{ mm} \quad (5.22)$$

For the same reason, the equation for the three-point weighted average method can be described as below,

$$a_0 = [(a_1 + a_3)/2 + a_2]/2 \quad \text{for } B \leq 5 \text{ mm} \quad (5.23)$$

For alloy 800 DCB specimen, the thickness B is small than 5 mm, so three-point weighted average method is used to determine the crack length increases for Pb-contaminated and Pb-free conditions, respectively.

(a) Crack Length Determination in Pb-contaminated condition

Figure 5.8 shows the cross-sectional view of the alloy 800 DCB specimen after being opened in air. A notable crack arrest can be observed in the middle of the SEM image. The top part in the image is caused by the fatigue pre-crack, and the bottom part is caused by fast fracturing during the arm opening procedure.

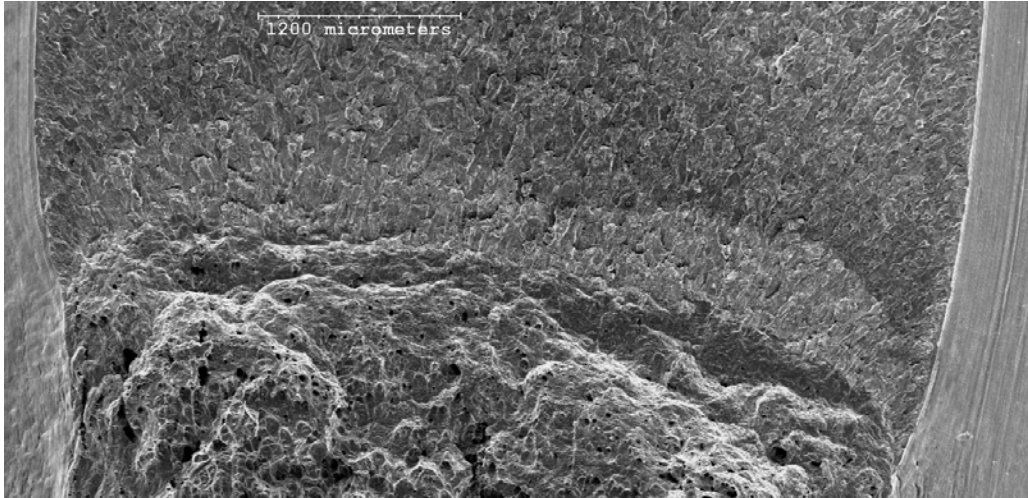
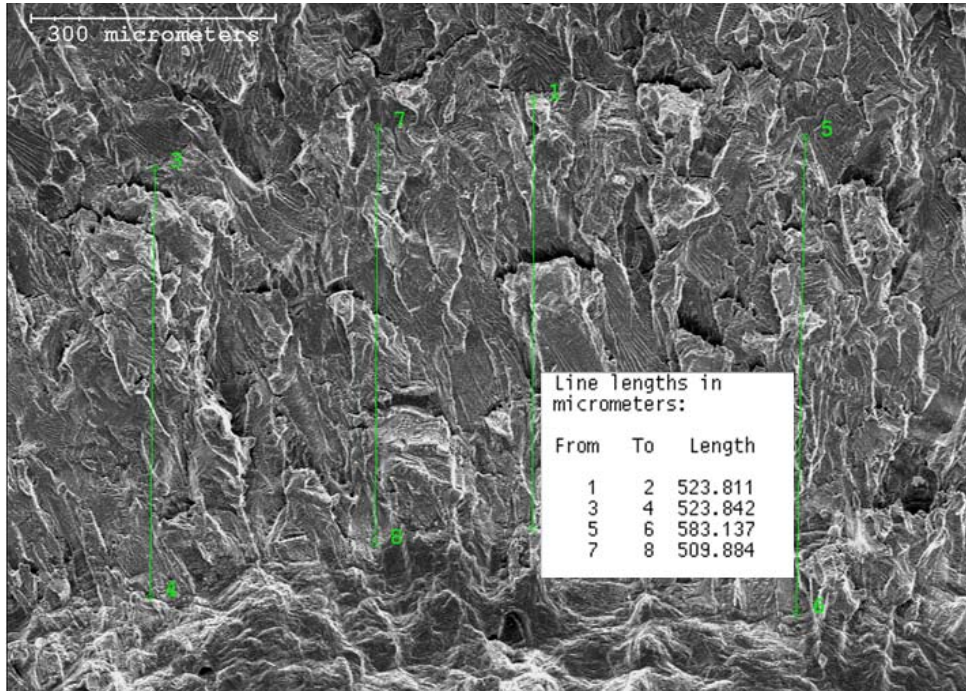
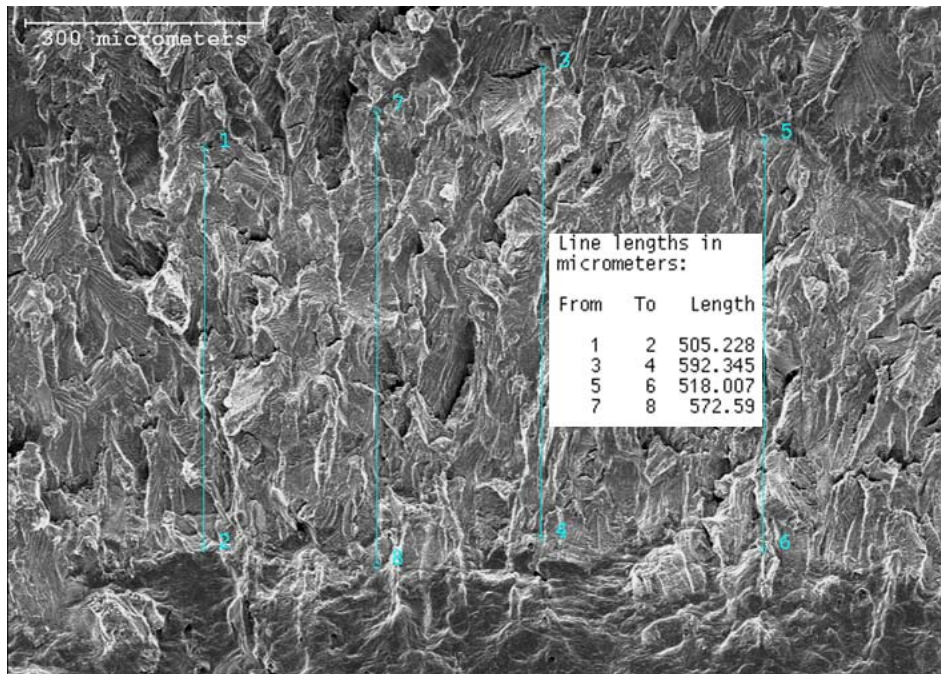


Figure 5.8 SEM image of the cross-sectional view of the alloy 800 DCB specimen after potential drop measurement in Pb-contaminated environment.

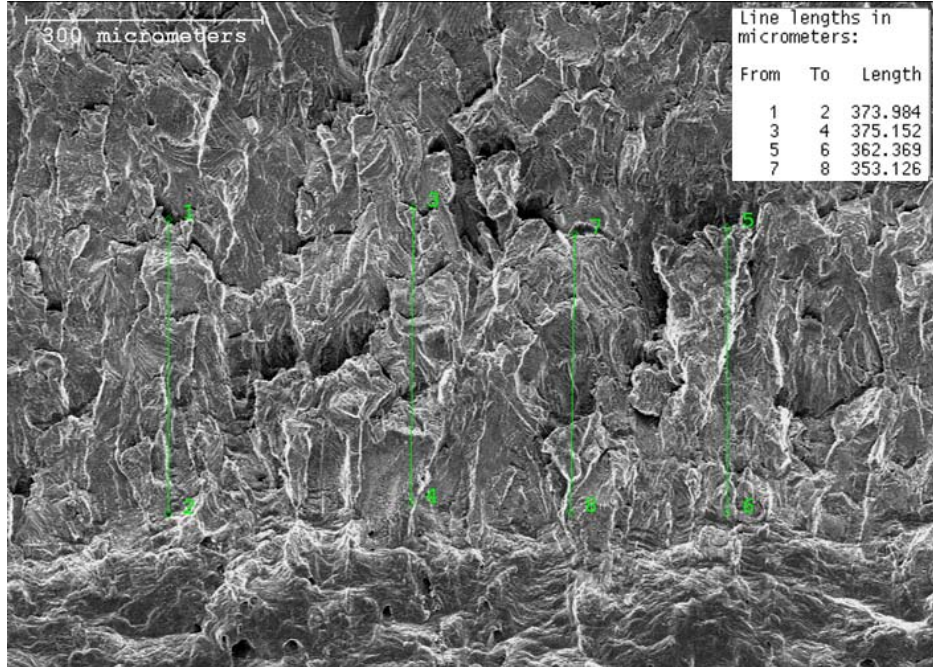
Figure 5.9 shows expanded SEM images of the crack arrests at different locations. Figure 5.9 (a) and (b) indicate locations near the specimen surface, while Figure 5.9 (c) exhibited the calculation of the crack length measurements at the center of the crack. The numbers on the images stand for the distance between two vertical consecutive points. To achieve a precise value of the average crack length changes Δa_1 , Δa_2 , and Δa_3 , four parallel distances were measured to calculate the average values.



(a)



(b)



(c)

Figure 5.9 SEM images of the crack arrest in Pb-contaminated condition with the crack length measurements at different spots of the crack (a) Left (b) Right and (c) Middle.

Table 5.3 shows the individual parallel measurements and the average values of Δa_1 , Δa_2 , and Δa_3 were also calculated in micrometer scale. After calculation, we know that $\Delta a_1 = 535 \mu\text{m}$, $\Delta a_2 = 547 \mu\text{m}$, and $\Delta a_3 = 366 \mu\text{m}$, respectively. According to equation 5.23, we can obtain

$$\Delta a_0 = [(\Delta a_1 + \Delta a_3)/2 + \Delta a_2] / 2 = 454 \mu\text{m} \quad (5.24)$$

In conclusion, the average crack growth of alloy 800 DCB specimen in Pb contaminated condition at 300°C is 0.454 mm. Compared to two different

predicted values 0.401 mm and 0.085 mm, the linear calibration curve is obviously more appropriate for the situation in this work, and the percentage error between the predicted and actual value is about 11.7 %. The real average crack growth velocity can be obtained, CPR(Pb-contaminated) is equal to 2.34 $\mu\text{m}/\text{h}$ (454 $\mu\text{m}/11638$ minutes).

Crack Length (μm)	Δa_1	Δa_2	Δa_3
1	524	505	374
2	524	592	375
3	583	518	362
4	510	573	353
Average	535	547	366

Table 5.3 The calculation table of the average crack length changes Δa_1 , Δa_2 , and Δa_3 .

(b) Crack Length Determination in Pb-free condition

The crack length in Pb-free condition was determined by the same three-point weighted average method. Figure 5.10 shows the cross-sectional view of the alloy 800 DCB specimen after potential drop measurement in Pb-free neutral crevice chemistries condition. There is a transition zone with a relatively deeper color in the middle of the image, which separates the top fatigue pre-crack region and the bottom fast fracturing region. Unlike the crack growth zone in Pb-

contaminated condition, the transition zone in Pb-free condition is not as obvious. Compared to that in Pb-contaminated condition, the transition between pre-crack region and fast fracturing region is more continuous, especially at the locations near the specimen surface, where no crack growth was observed.

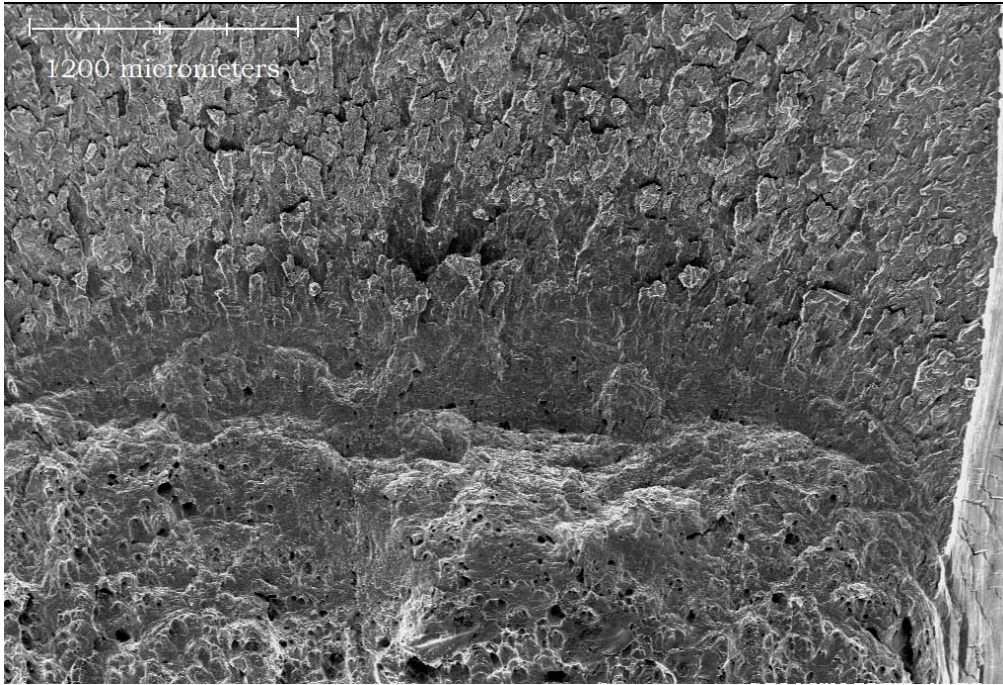


Figure 5.10 SEM image of the cross-sectional view of the alloy 800 DCB specimen after potential drop measurement in Pb-free environment

Figure 5.11 shows the expanded image of the middle part of the transition region, which can be considered as evidence of the crack growth Δa_3 .

$$\Delta a_3 = (127 + 132 + 146) / 3 = 135 \mu m \quad (5.25)$$

According to the definition of the three-point weighted average method, the Δa_1 and Δa_2 can be considered as 0, since the crack growths near the specimen surface regions are negligible. As a result, the crack growth in Pb-free condition can be calculated as follows,

$$\Delta a_0 = [(\Delta a_1 + \Delta a_3)/2 + \Delta a_2] / 2 = 68 \mu m \quad (5.26)$$

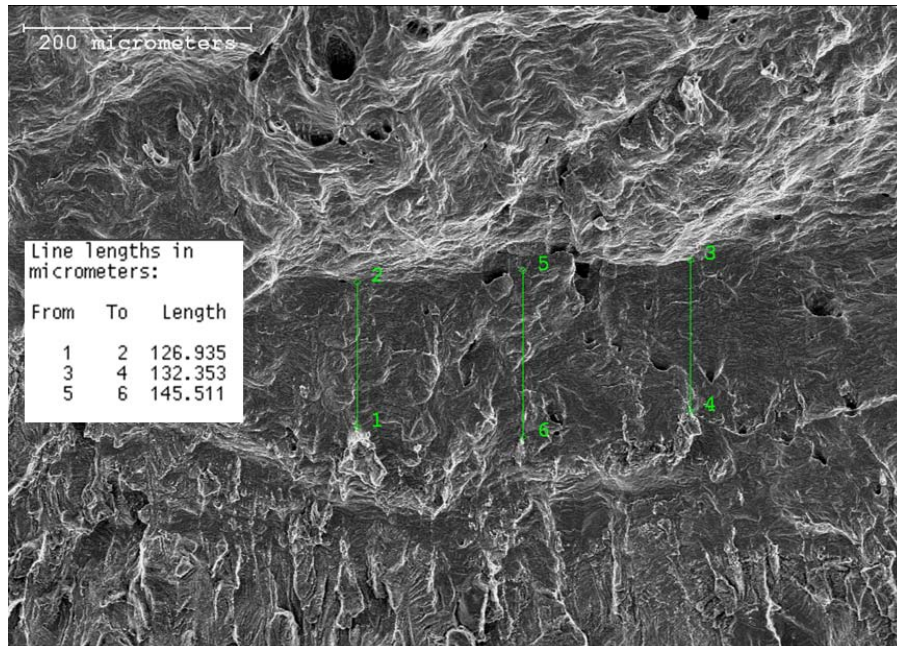


Figure 5.11 SEM images of the crack arrest in Pb-free with the crack length measurements in the middle of the crack

In Pb-free condition, the average crack growth of alloy 800 DCB specimen at 300°C is 0.068 mm. Two different predicted values of 0.017 mm and 0.0022 mm, tend to be smaller than the real crack growth. Therefore, the crack propagation rate of alloy 800 DCB specimen in Pb-free condition is 0.035 $\mu m/h$

(0.068 mm/11638 minutes), larger than the linear prediction of 0.0088 μ m/h (0.017 mm/11638 minutes). This may be attributed to the ambiguous crack growth region (transition zone) shown in Figure 5.11. No obvious horizontal crack growth arrest was observed in Figure 5.11. The transition zone in the middle might be caused by fast fracturing procedure.

(c) Comparison of Non-Linear and Linear Calibration Curves

Based on the actual crack growth, determined by the SEM approach, the linear calibration curve provides a more accurate estimate of the crack length increase in Pb-free neutral crevice chemistries condition at 300°C. This might be attributed by the fitting curve error of the variables C and m. The exponential amplification of the error from “m” is another factor of the inaccurate crack propagation estimate. The variation can also be caused by picking different reference points V_0 and α_0 . In general, the linear calibration curve with temperature dependence adjustment indicated an effective crack growth prediction in both Pb-contaminated and Pb-free conditions.

5.1.3 Periodic Crack Propagation Behaviour

There are different mechanisms proposed to explain the SCC process. Anodic dissolution, film-induced cleavage, and hydrogen brittlement (HE) are the three most popular SCC mechanisms. Slip dissolution is another type of dissolution mechanism, but it is used convincingly in many systems. Ford provided a detailed analysis on this model [33]. In many systems, crack

propagation is usually correlated with the oxidation process, so slip-oxidation provides a more accurate concept on the SCC mechanism, because crack advance is usually due to the combination of M/M+ and M/MO oxidation reactions.

In Ford's film rupture theory, the crack propagation rate is described as below,

$$\bar{V}_t = \frac{M}{z\rho F} \frac{Q_f}{\varepsilon_f} \dot{\varepsilon}_{ct} \quad (5.27)$$

where M and ρ are the atomic weight and density of the crack-tip metal. F is Faraday's constant, the fracture strain of the film is ε_f , and crack-tip strain rate is $\dot{\varepsilon}_{ct}$.

In the crack propagation process, the oxidation of the crack tip (film rupture) is competing with the protective film formation process, which caused a repetitive crack advance process. This frequency of film rupture is determined by the fracture strain of the film (ε_f) and crack-tip strain rate ($\dot{\varepsilon}_{ct}$) in equation 5.28.

$$f = \varepsilon_f / \dot{\varepsilon}_{ct} \quad (5.28)$$

Figure 5.12 shows a potential fluctuation in the crack propagation process, which indicated the periodic crack advance behaviour. The potential signal of the same specimen in static condition at 300°C is taken as a reference. The average frequency is calculated to be about 31 minutes. Considering the CPR at Pb-contaminated condition is 2.34 $\mu\text{m/h}$, the theoretical repetitive crack arrest at each cycle is about 1.21 μm . Figure 5.13 shows the actual crack arrest during the crack propagation zone. The periodic crack arrest band is about 1.3 μm wide, which is quite consistent with the theoretical calculation. The experimental results indicate

that the crack propagation behavior followed Ford's repetitive film rupture behavior very well.

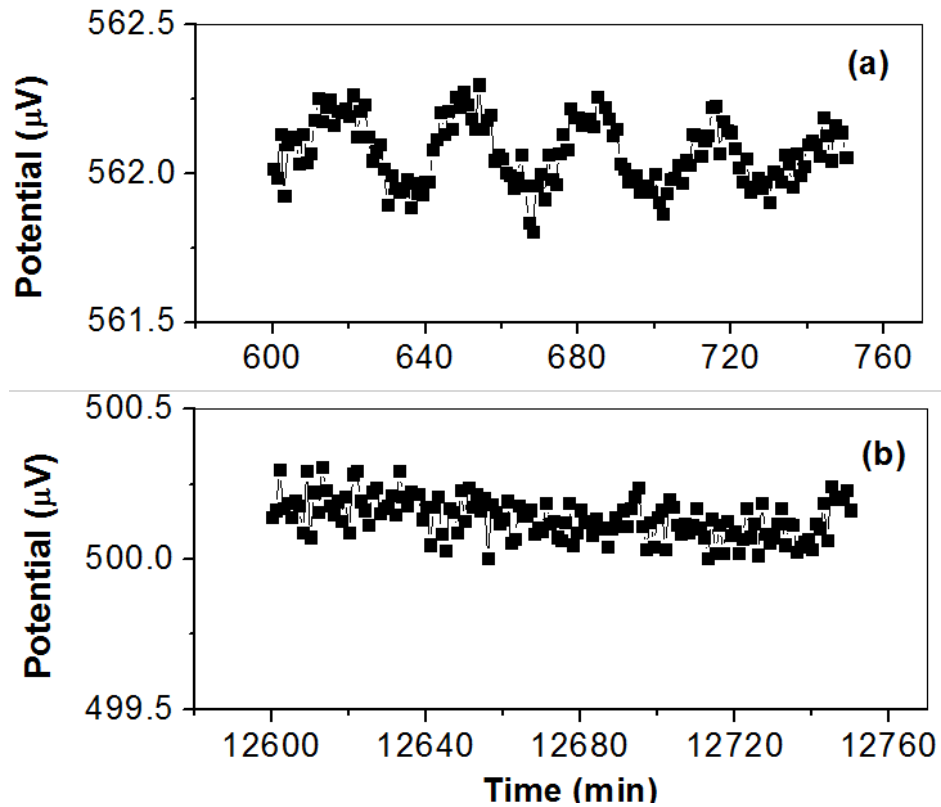


Figure 5.12 Comparison of (a) potential fluctuation in crack propagation process and (b) reference potential signal of the same specimen

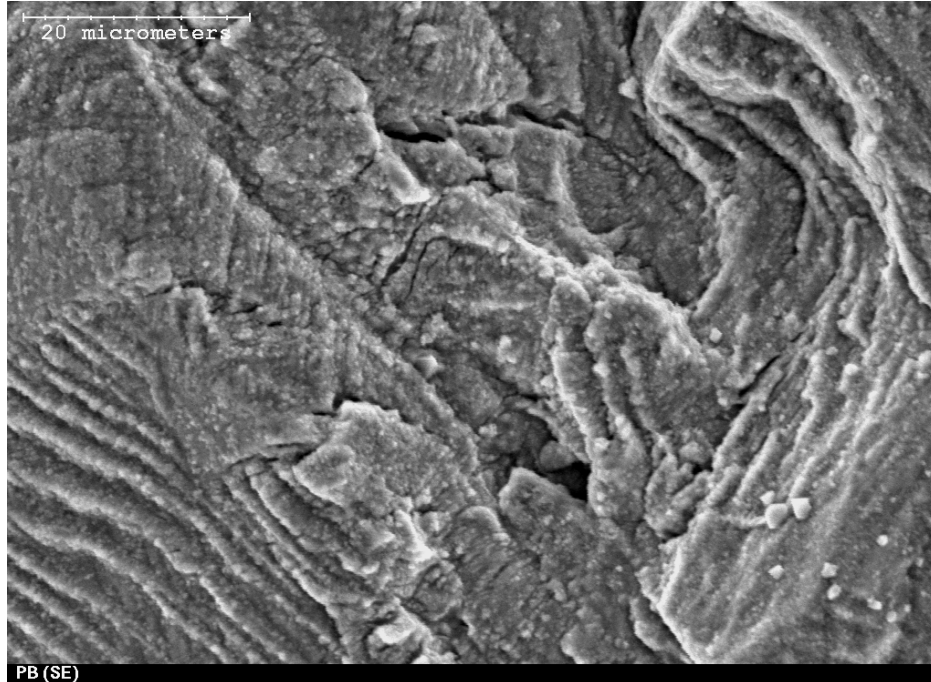


Figure 5.13 The SEM image of the crack arrest in the Pb-contaminated neutral crevice chemistry conditions, showing the periodic crack advance behaviors

5.1.4 Calculation of the stress intensity factor K for alloy 800 DCB specimen in both Pb-contaminated and Pb-free conditions at 300°C

Stress intensity factor, K , is an important parameter used in fracture mechanics to accurately predict the stress state near the crack tip. The DCB specimen is very convenient for the fracture mechanics calculation. Figure 5.14 provides a schematic representation of the specimen dimension and the load P , applied by an inserted wedge [27]. The height of each cantilever beam is H , and the thickness of the specimen is represented by B . The crack length, a , is defined

as the distance between the loaded line and the crack tip. The ratio of a / H is very critical in determining the fracture toughness of the materials. Many researchers have been dedicating a lot of effort on understanding fracture toughness with different a / H ratios. According to elementary beam theory [28], the stress intensity factor is given for large values of a / H as follows:

$$K = P \left(\frac{12}{H} \right)^{1/2} \left(\frac{a}{H} \right) \quad (5.27)$$

where P is the magnitude of the loads per unit thickness.

For the cases with very small values of a / H , Irwin's solution for a semi-infinite crack in an infinite sheet can be used as an approach to obtain the stress intensity factor [29],

$$K = P \left(\frac{2}{\pi a} \right)^{1/2} \quad (5.28)$$

Later in 1966, Gross and Srawley [30] extended the elementary beam solution to smaller values of a / H , and the expression is shown below based on boundary collocation,

$$K = P \left(\frac{12}{H} \right)^{1/2} \left[\left(\frac{a}{H} \right) + 0.687 \right] \quad (5.29)$$

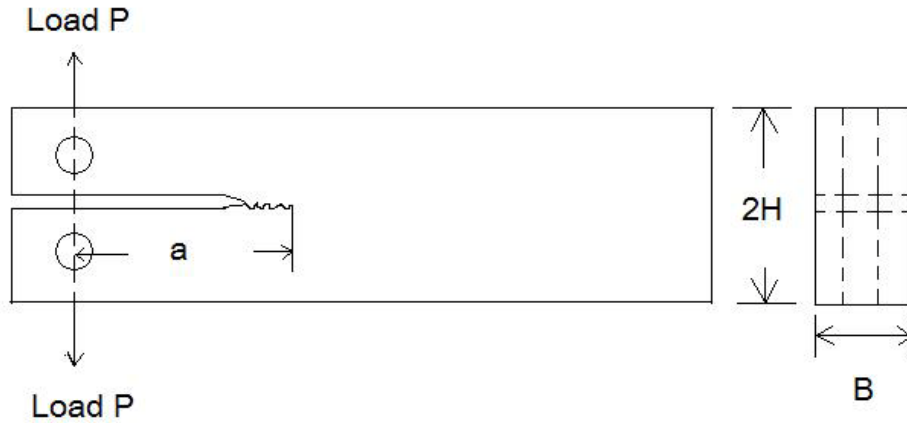


Figure 5.14 The schematic representation of the DCB specimen with a load P .

In 1985, Foote and Buchwald proposed a simple approximation formula for stress intensity factor, K , and they claimed that the values differ from the theoretical K values by less than 1.1 percent [31]. The formula is give below,

$$\frac{KH^{1/2}}{P} = \sqrt{12} \left(\frac{a}{H} + 0.673 \right) + \sqrt{\frac{2H}{\pi a}} - \left(0.815 \left(\frac{a}{H} \right)^{0.619} + 0.429 \right)^{-1} \quad (5.10)$$

This equation applied for all values of a / H , with $c / H > 2$ where c is the uncracked ligament.

Recently, calculation of the mode I stress intensity factor, K_I , is given by Sedriks [27] as follows:

$$K_I = \frac{E \cdot V_Y \cdot H (3H(a + 0.6H)^2 + H^3)^{1/2}}{4((a + 0.6H)^3 + H^2 a)} \quad (5.11)$$

$$\text{Range of Applicability } 2 \leq \frac{a}{H} \leq 5$$

where V_Y : The crack opening displacement (COD) at loaded line.

E: Young's modulus

This equation can be used to calculate K_I in situations where the load P is difficult to measure, so it is appropriate to use equation 5.11 in this work. For alloy 800 DCB specimen, the value $H = 12.68$ mm, $a_0 = 41.42$ mm before a wedge is inserted. According to the alloy product data bulletin [32], Young's modulus, E, of alloy 800 at 400°F and 600°F is 26.81×10^6 psi, and 25.71×10^6 psi, respectively, so the E at 300°C (572°F) is 25.86×10^6 psi. In this work, $a / H = 3.3$, so it satisfies the range of applicability of equation 5.11.

For the pre-crack alloy 800 DCB specimen without wedge, $V_Y = 0.26$ mm, so K_I can be calculated according to equation 5.11 below,

$$K_I(\text{without wedge}) = \frac{E \cdot V_Y \cdot H(3H(a + 0.6H)^2 + H^3)^{1/2}}{4((a + 0.6H)^3 + H^2a)} = 11.4 \text{Mpa} \cdot \text{m}^{1/2}$$

(5.12)

When the wedge was inserted in the DCB specimen, the V_Y increased to 1.60 mm, and all other parameters stay constant, so the stress intensity factor for the DCB specimen with wedge can be calculated,

$$K_I(\text{with wedge}) = \frac{E \cdot V_Y \cdot H(3H(a + 0.6H)^2 + H^3)^{1/2}}{4((a + 0.6H)^3 + H^2a)} = 69.7 \text{Mpa} \cdot \text{m}^{1/2}$$

(5.13)

The inserted wedge increased the stress intensity factor of alloy 800 DCB specimen dramatically. During the potential drop measurements, we assume the opening displacement distance does not change with crack increase, since the crack increase is too small compared to the total crack length. After the Pb-contaminated potential drop measurement, the crack length a increased from 41.42 mm to 41.82 mm, so the K_I can be adjusted as follows:

$$K_I(\text{Pb - contaminated}) = \frac{E \cdot V_Y \cdot H(3H(a + 0.6H)^2 + H^3)^{1/2}}{4((a + 0.6H)^3 + H^2a)} = 68.7 \text{Mpa} \cdot \text{m}^{1/2}$$

(5.14)

In Pb-free condition, the crack length a increased from 41.42 mm to 41.49 mm, so the K_I can also be adjusted for Pb-free condition as follows,

$$K_I(\text{Pb - contaminated}) = \frac{E \cdot V_Y \cdot H(3H(a + 0.6H)^2 + H^3)^{1/2}}{4((a + 0.6H)^3 + H^2a)} = 69.5 \text{Mpa} \cdot \text{m}^{1/2}$$

(5.15)

As we can see, the K_I changed from 69.7 MPa·m^{1/2} to 68.7 MPa·m^{1/2} in Pb-contaminated potential drop measurement and changed to 69.5 MPa·m^{1/2} in Pb-free measurement; the relative percentage differences are only 1.4% and

0.29% for the two measurements, respectively. Therefore, we can consider that the stress intensity level does not change in the potential drop measurements for alloy 800 DCB specimen in neutral crevice chemistries conditions.

5.2 Conclusions

In this work, the potential drop system was used to investigate the effect of lead on the SCC behaviour of alloy 800 DCB specimen in neutral crevice chemistries conditions. The linear calibration curve was found to predicate the crack growth of alloy 800 DCB specimen more precisely, compared to the non-linear calibration curve. The slope of the potential vs. crack length calibration curve was obtained, which is 1.29×10^{-5} V / mm at 300°C, considering the temperature dependence of the resistivity of alloy 800.

From the experimental results, the average CPR of the alloy 800 DCB specimen in Pb-contaminated condition is 2.34 $\mu\text{m/h}$, which is slightly larger than the prediction of 2.06 $\mu\text{m/h}$ based on the calibration. However, the average CPR in Pb-free condition is 0.035 $\mu\text{m/h}$, much smaller than that of Pb-contaminated condition. It was also observed that the concentration of Pb content in the crack growth zone is larger than the pre-crack region in Pb-contaminated potential drop measurements, which indicated that incorporation of Pb in the passive film deteriorates the stress corrosion cracking of the alloy 800 DCB specimen.

The repetitive crack propagation behaviour observed in the Pb-contaminated condition is consistent with the film rupture theory. The actual

repetitive crack arrest observed in the SEM image is quite consistent with the calculated results based on the experimental CPR.

The stress intensity factor (mode I), K_I , was also calculated before and after the potential drop measurement in both Pb-contaminated and Pb-free conditions. It was found that the K_I changed from $69.7 \text{ MPa}\cdot\text{m}^{1/2}$ to $68.7 \text{ MPa}\cdot\text{m}^{1/2}$ in Pb-contaminated potential drop measurement, and changed to $69.5 \text{ MPa}\cdot\text{m}^{1/2}$ in Pb-free measurement, so the stress intensity can be considered constant during the potential drop measurements.

Reference

1. H.R. Copson and S.W. Dean, *Corrosion* **21** (1965), p. 1.
2. T. Sakai, S. Okabayashi, K. Aoki, K. Matsumoto and Y. Kishi, *Corrosion*, 90 – paper no. 520, NACE, Houston (1990).
3. S.S. Hwang, U.C. Kim and Y.S. Park, *J. Nucl. Mater.* **246** (1997), p. 77.
4. J. Lumsden, A. McIlree, R. Eaker, R. Thomson, S. Slosnerick, Effects of Pb on SCC of Alloy 600 and Alloy 690 in prototypical steam generator chemistries, in: T.R. Allen, P.J. King, L. Nelson (Eds.), Proceedings of the 12th International Conference on Environmental Degradation of Materials in Nuclear Power System – Water Reactors, Salt Lake City, Utah, USA, August 14–18, (2005).
5. B.T. Lu, B. Peng, J.L. Luo, Y.C. Lu, Passivity of nuclear steam generator tube alloy in lead-contaminated crevice chemistries with different pH, in: Proceedings of 13th International Conference on Environmental Degradation

- of Metals in Nuclear Power Systems, Paper No. 172, Whistler, BC, Canada, August 19-23, Canadian Nuclear Society, 2007.
6. B. Peng, B.T. Lu, J.L. Luo and Y.C. Lu, *Journal of Nuclear Materials* 318 (2008), p. 333.
 7. A. Palani, B.T. Lu, L.P. Tian, J.L. Luo and Y.C. Lu, *Journal of Nuclear Materials* 396 (2010), p. 189.
 8. R. W. Staehle: *Assessment of and Proposal for a Mechanistic Interpretation of the SCC of High Nickel Alloys in Lead-Containing Environments*, 11th Environ. Degrad. ANS, 2003, p.381.
 9. Y.C. Lu, Effect Of Lead Contamination On Steam Generator Tube Degradation, Proceedings of 12th International Conference on Environmental Degradation of Materials in Nuclear Power Systems - Water Reactors Edited by TMS (The Minerals, Metals & Materials Society), 2005.
 10. B.T. Lu, J.L. Luo, Y.C. Lu, *Electrochimica Acta*, 53(12), 2008, 4122-4136.
 11. Merah, N., “DC Potential Drop Calibration in Creep-Fatigue Loading Conditions,” *Journal of Testing and Evaluation*, JTEVA, Vol. 28, No. 4, July 2000, pp. 301–306.
 12. Merah, N., Bui-Quoc, T., and Bernard, M., “Calibration of DC Potential Technique Using an Optical Image Processing System in LCF Testing,” *ASTM Journal of Testing and Evaluation*, Vol. 23, 1995, pp. 160–167.
 13. A. Matthiessen, *Progg. Anallen*, 122, 47 (1864) .
 14. Seymour J, *Physical Electronics*, chapter 2, Pitman, (1972).
 15. K. Ikeda, K. Suzuki and K. Tanosaki, *Journal of Magnetism and Magnetic*

- Materials* 40 (1983), p. 232.
16. Hans Litschel, *Phys. Chem. Solids*, Vol. 46, No. 12, (1985), p. 1421.
 17. D. F. Jones, G. Stroink, Z. M. Stadnik and R. A. Dunlap, *Materials Science and Engineering*, 99 (1988) p. 207.
 18. Copson, H. R., Dean, S. W., *Corrosion* 21 (1965), p. 1.
 19. Staehle, R. W., “Clues and issues in the SCC of High Nickel Alloys Associated with Dissolved Lead”, Proceedings of the 12th International Conference of Environmental Degradation of Materials in Nuclear Power System – Water Reactors – Eds., T. R. Allen, P. J. King, L. Nelson, TMS (The Minerals, Metals & Materials Society) (2005).
 20. Lu, B. T., Luo, J. L., Lu, Y. C., *J. Electrochem. Soc.* 154 (2007) p. C379.
 21. C. Y. Chao, L. F. Lin, and D. D. Macdonald, *J. Electrochem. Soc.*, 128, (1981), p. 1187.
 22. L. F. Lin, C. Y. Chao, and D. D. Macdonald, *J. Electrochem. Soc.*, 128, (1981), p. 1194.
 23. D. D. Macdonald, *J. Electrochem. Soc.*, 138, (1992), p. 3434.
 24. Lu, B. T., Luo, J. L., Lu, Y. C., *Electrochimica Acta*, 53, (2008), p. 4122.
 25. ASTM E 2472-06. Standard test method for determination of resistance to stable crack extension under low-constraint conditions. In: *Annual book of ASTM standards*, vol. 03.01. West Conshohocken, PA, USA: American Society for Testing and Materials; (2007).
 26. J. Ahmad, J. Purbolaksono, and L. C. Beng, *Engineering Failure Analysis*, Vol. 17, 1 (2010), p. 328.

27. A. J. Sedriks, *Corrosion of Stainless Steels: Stress Corrosion Cracking*, John Wiley & Sons, New York, (1979), p.139.
28. J.J. Gilman, *Fracture*, Ed. B.L. Averbach et al., John Wiley and Sons, Inc., New York (1959), p. 193.
29. G.R. Irwin, *Transactions ASME, Journal of Applied Mechanics*, 24, (1957), p. 361.
30. B. Gross and J.E. Srawley, "*Stress Intensity Factors by Boundary Collocation for Single-Edge Notch Specimens Subjected to Splitting Forces*", NASA TN D-3295 (1966).
31. R.M.L. Foote and V.T. Buchwald, *International Journal of Fracture*, 29, (1985), p. 125.
32. Product Data Bulletin C 800/800H, G. O. Carlson, Inc.
33. F.P. Ford, *Quantitative prediction of environmentally assisted cracking*, *Corrosion* 52 (1996) (5), p. 375.

Chapter 6

General Conclusions and Future Work

6.1 General Conclusions

In this work, the effects of $S_2O_3^{2-}$ and stress on the corrosion behavior of alloy 800 was studied by using scratch tests with electrochemical measurements and SECM in simulated nuclear steam generator secondary side crevice chemistries suggested by AECL. Scratch tests and SECM experiments revealed that $S_2O_3^{2-}$ enhanced the metal/oxide dissolution and retarded the repassivation process after the passive film was mechanically damaged by a scratch. On the other hand, the applied stress on alloy 800 degraded the corrosion resistance of the alloy by decreasing pitting potentials, and increasing passive current and surface reactivity/conductivity. The applied stress activated the grain boundaries on the C-ring specimens, and caused crack initiation possibly at grain boundaries, at triple points and at inclusions in an aggressive solution, such as NC2. A synergistic effect between $S_2O_3^{2-}$ and stress on the corrosion degradation of alloy 800 was also clearly observed in our experiments. The synergistic effect between $S_2O_3^{2-}$ and stress were mainly contributed by the active regions on the specimen surface.

In the study of PbSCC in the simulated crevice solutions at 300°C, the

average CPR of the alloy 800 DCB specimen in Pb-contaminated condition is 2.34 $\mu\text{m/h}$, which is slightly larger than the prediction of 2.06 $\mu\text{m/h}$ based on the calibration. However, the average CPR in Pb-free condition is 0.035 $\mu\text{m/h}$, much smaller than that of Pb-contaminated condition. It was also found that the concentration of Pb content in the crack growth zone is larger than the pre-crack region in Pb-contaminated potential drop measurements, which indicated that the incorporation of Pb in the passive film deteriorates the stress corrosion cracking of the alloy 800 DCB specimen.

The repetitive crack propagation behaviour observed in the Pb-contaminated condition is consistent with the film rupture theory. The actual repetitive crack arrest observed in the SEM image is quite consistent with the calculated results based on the experimental CPR. The stress intensity factor (mode I), K_I , was also calculated before and after the potential drop measurement in both Pb-contaminated and Pb-free conditions. It was found that the K_I changed from 69.7 $\text{MPa}\cdot\text{m}^{1/2}$ to 68.7 $\text{MPa}\cdot\text{m}^{1/2}$ in Pb-contaminated measurements, and changed to 69.5 $\text{MPa}\cdot\text{m}^{1/2}$ in Pb-free measurements, so the stress intensity can be considered constant during the potential drop measurements.

6.2 Future Work

The S^y -SCC and PbSCC of alloy 800 have been studied at room temperature, and 300°C, respectively. The following topics could be some directions in future research:

1. It will be beneficial to investigate the effect of reduced sulphur species on the SCC behavior of alloy 800 at high temperature, which simulate nuclear reactor environments.
2. A quantitative study of the effect of applied stress on the S^y-SCC could also help us further understand the synergistic effect of thiosulfate and applied stress.
3. The potential drop system could also be used to study the crack growth of alloy 800 C-ring specimen in the simulated crevice solutions with reduced sulphur species.
4. Studies of passive film thickness on the alloy 800 in simulated crevice solutions at 300°C could also contribute to our understanding of the crack propagation mechanisms at high temperature based on film rupture theory.